NORTHWESTERN UNIVERSITY

Toward Molecular Detection of Drifting Fundamental Constants

A DISSERTATION

SUBMITTED TO THE GRADUATE SCHOOL

IN PARTIAL FULFILLMENT OF THE REQUIREMENTS

for the degree

DOCTOR OF PHILOSOPHY

Field of Chemistry

By

Mark Gabriel Kokish

EVANSTON, ILLINOIS

June 2018

ABSTRACT

Toward Molecular Detection of Drifting Fundamental Constants

Mark Gabriel Kokish

Techniques in atomic physics have delivered some of the most precise measurements ever made, with frequency measurements reaching fractional precisions of 1×10^{-18}. High precision measurements can be used to test fundamental physics, such as pursuing a variation in fundamental constants. A finite drift in measurable constants such as the proton-to-electron mass ratio (μ) would reveal physics beyond the Standard Model. Rovibrational transitions in molecules offer a way to surpass constraints on the variation of μ placed by atomic measurements.

This thesis describes the development of new techniques to measure molecules at unprecedented precision and place new constraints on the variation of μ. We work exclusively with molecular ions, which allows us to trap and interrogate molecules for long periods of time. By simultaneously trapping laser-cooled atomic ions, the molecules are cooled down to temperatures where Doppler shifts are no longer a limiting factor. We describe two different methods to address the initial challenge of producing molecular ions inside the ion trap. In the first method, we construct a molecular beam directed at trapped

ions in order to produce novel molecular ions. The second method involves photoionizing molecules entrenched in a molecular beam, for which we developed a new nozzle design.

We also make further development toward achieving single molecule spectroscopy, where we aim to achieve the highest precision. We implement a method of producing our highly reactive molecule of interest, AlH^+. We also determine the optimum protocol for a new type of nondestructive, single-molecule quantum state detection, by transferring the internal state information of AlH^+ onto a co-trapped Ba^+ ion. This state detection will ultimately be used to perform high precision spectroscopy. Lastly, we perform an in-depth analysis of the molecular characteristics necessary to provide the best constraint of μ-variation. We propose measuring TeH^+, which has unique properties that allow for fast accumulation of statistics. TeH^+ is also relatively insensitive to systematic frequency shifts caused by external fields, despite being polar. These new techniques and new molecules will integrate into a growing field of high precision molecular spectroscopy.

Acknowledgements

I received so much support over the course of this Ph.D. from many people to whom I am immensely grateful. I first want to thank my adviser Brian Odom. Brian is kind, patient and an inspiring writer. He always asked the questions that gave me a stronger physical intuition. Brian is also willing to take risks, such as betting on this chemist wanting to give AMO physics a try. I will always be grateful to Brian for fostering an environment where I could discover my passion. I am simultaneously indebted to my co-adviser Tamar Seideman, who supported my experimental efforts and inspired me to dive into molecular theory, giving me the level of understanding I hoped to achieve in my Ph.D. I also thank Emily Weiss for helping make my joint advisership possible and my committee members Toru Shiozaki and Richard Van Duyne for their insight over the years.

I had the help of several graduate student mentors along the way. Vaishnavi Rajagopal bravely handed me her experiment in my first year. Her inexhaustible positive energy and willingness to help guaranteed my success that year. Chien-Yu Lien also had an active presence in my first year, providing level-headed and practical advice. I will also never forget the moment he showed me a trapped ion cloud large enough to see with the naked eye. I was also lucky to have met Yen-Wei Lin, who was always willing to have a conversation and dispense useful information when I really needed it. My special thanks also go to Chris Seck, who taught me so much. He showed me how to build lasers and

gave many tips for building electronic circuits. Most importantly, he did a fantastic job building the infrastructure for the single molecule spectroscopy (SMS) experiment, which required persistence and hard work. His efforts made my life much easier.

I also owe many thanks to the senior group members. Matt Dietrich helped me through the molecular beam and SMS experiments. Exchanging ideas was effortless with Matt. His expertise was far-reaching, and he was always willing to learn more. Shih-Kuang (Zeke) Tung was an absolute pleasure to spend time with. I will always remember his infectious laugh and willingness to entertain wild ideas. I envy the students that will work with Matt and Zeke over the course of their careers. Vincent Carrat was also a lifesaver for our lab and the SMS experiment. He brought much-needed optics experience to our lab, and he was always willing to put the needs of others before his own. Vincent expected nothing but the best for our experiment, and our experiment was made much better for it. It was also a breath of fresh air to have someone more passionate about Linux than me. Working with Vincent on tasks as dull as setting up an Apache server made for some of the best moments I had throughout my Ph.D. I also want to thank Jacob Johansen for his experimental advice, and Ivan Antonov for his molecular and experimental insight.

Patrick Stollenwerk started in the Odom group shortly before I did and has been with me since my first day at Northwestern. Pat has helped me a countless number of times on my experiments, and I could talk to him about anything. He has an excellent intuition. Even when I was most confident about a particular idea, if Pat smelled something wrong with it, we would often discover the problem shortly afterwards. I will miss being able to bounce ideas off each other.

I am also excited for the next generation of Odom group students. Panpan Huang took over the AlH^+ experiment after I left. I am in awe of the resilience she has shown, and I anticipate great results from her experiment. I was always envious of Joseph Cordero-Mercado because he started his experiment from scratch. I know he will have a bright future, and I am grateful for his interesting conversations and for how many optomechanical parts he has let me borrow throughout the years. James Dragan and Greg Rabelo Moreira Da Silva are the brave students taking over the SMS experiment. They continue to impress me day after day with their eagerness to learn and ability to learn quickly. They will without a doubt be successful in their endeavors. My overall interactions with the younger students have made me a better experimentalist and mentor.

When not running experiments in the Odom group, I was a theorist in the Seideman group. The Seideman group has collectively been very helpful. In particular, I am thankful for my colleague Tom Purcell, who is both fiercely intelligent and reliable. I also wish to thank Josh Szekely and Thomas Grohmann for their help with molecular theory. My thanks also go to Chelsea Mueller for taking on a project related to my work, giving me the opportunity to understand my research better.

My hopes of acquiring a Ph.D. were nourished well before arriving at Northwestern. I want to thank Hartmut Häffner for giving me the opportunity to first work with trapped ions. His students Mike Ramm and Thaned (Hong) Pruttivarasin were the experimentalists I tried to mimic, and I kept their advice in mind throughout the course of my Ph.D. I am also indebted to Caroline Ajo-Franklin, who gave me my first independent research opportunity at Lawrence Berkeley National Laboratory. There Heather Jensen was a friend and mentor to me. She taught me key skills that I made sure to use and

pass on to my younger students. I also have to thank Jane Ricci, who gave me my first job in a chemistry laboratory back in high school, which put me on the path toward a chemistry degree.

Equally important was the support I received outside of work. Bram, Dolev, Nolan and Weiwei: I have no idea how such a diverse group of personalities ended up spending so much time together, but these individuals provided me with great memories. I also want to thank Brian Maher, my friend since elementary school, who periodically phoned me from the other side of the country. Brian, Ana and the Maher family gave me some of my best experiences, reminding me of life outside graduate school. My thanks also go to Shih-Min and Chi-Yuan Tsao, who always treated me like family and made me feel at home in Taiwan.

I lastly want to thank my family members. My aunt and uncle, Ira and Sam, and my sister Iris have been a constant positive force in my life. My parents Lyudmila and Arkady worked so hard to provide me with every possible advantage. Their unconditional love and support were with me every step of the way. Lastly, I want to thank my fiancé Angela Tsao. She is best my friend, good luck charm and source of joy. Angela worked harder and sacrificed more than me to make my Ph.D. a reality, and I will always be thankful.

Preface

This thesis forgoes the theoretical background for several of the well-established techniques used here. Collected here are a list of relevant works sorted by category that provide background for the contents of this thesis.

Techniques in Atomic Physics

- Laser Cooling and Trapping - H. Metcalf [1]
- Controlling the Quantum State of Trapped Ions - C. Roos [2]
- Raman Sideband Cooling and Coherent Manipulation of Trapped Ions - S. Webster [3]

Molecular Beams

- Atom, Molecule, and Cluster Beams I - H. Pauly [4]
- The Even-Lavie Valve as a Source for High Intensity Supersonic Beam - U. Even [5]

Molecules

- Molecular Spectra and Molecular Structure Vol. I: Diatomic Molecules - G. Herzberg [6]
- Rotational Spectroscopy of Diatomic Molecules - J. Brown and A. Carrington [7]
- New Physics with Cold Molecules: Precise Microwave Spectroscopy of CH and the Development of a Microwave Trap - S. Truppe [8]

Dedication

To Angela and my parents Arkady and Lyudmila.

Table of Contents

List of Tables

List of Figures

CHAPTER 1

Introduction

Some of the most exciting scientific discoveries are those that reveal a more fundamental structure from which our current theories emerge. Unexplained phenomena in physics such as the matter-antimatter asymmetry [13], the tiny nonzero cosmological constant [14, 15], and the existence of dark matter [16], point to an underlying theoretical foundation. Arguably, the largest indicator of a more complete theory is the existence of fundamental constants, values that we can only measure, but not calculate.

There are 25 quantities that are considered fundamental [17]. Although fundamental in nature, the dimensionful quantities: the speed of light (c), Newton's gravitational constant (G) and Planck's constant ($\hbar$), are not insightful because their values are different depending on which system of units is being used. It can be shown ([18]) that any perceived change in one of the aforementioned dimensionful constants can always be attributed to a change in a fundamental dimensionless constants.[1] The dimensionless constants have specific physical meaning. For example, the fine structure constant (α) represents the coupling strength of a charged particle with the electromagnetic field, and the strong coupling constant (α_s) governs the strength of the strong interaction. The values of these constants are especially important to us observers, because had they been only slightly different (within a few percent), our universe would not lead to conditions that support a habitable universe [20].

[1] See also Section 3.2 of [19].

1.1. Drifting Fundamental Constants

Because no theory can predict the values of the fundamental constants, there is no reason to expect that they are actually constant. In fact, varying fundamental constants may help explain the vast strength difference between the gravitational and electromagnetic interactions [21], and potentially explain the coincidence problem [21, 22, 23]. Some have hypothesized that drifting fundamental constants could be attributed to interactions with dark matter [24, 25] or extra dimensions [26]. Therefore, constraining the variation of fundamental constants through measurement is well motivated for solving some of the most puzzling unexplained phenomena in physics.

An experiment constraining the variation of fundamental constants is relatively straightforward in principle, though not in practice. For example, the energy of electronic transitions in atoms can be related to α [27]. To constrain the variation of α, one simply needs to measure such an electronic transition, wait a certain period of time, and measure the same transition again. Barring any random or systematic frequency shifts, the drift of the measured frequency will be directly related to a drift in α. Because we have yet to observe a change in fundamental constants, all constraints in their variation amount to how precisely we can measure a given transition, setting an upper bound to their variation.[1]

One way to effectively "wait" a long period of time between measurements would be to measure atomic spectra from billions of years in the past and compare them to spectra measured today, something astronomers can do routinely. Measurements constraining the variation of α [28, 29], or even claiming a significant variation [30], are currently growing in number. An up-to-date review of the current status of these measurements can be found

[1] A more complete derivation for the example of the proton-to-electron mass ratio is given in Section 5.2.

in [31]. The challenge with astronomical measurements, however, is the lack of control over the source spectra, leading to a more difficult elimination of systematic frequency offsets. Any limit set by astronomical measurements would therefore be greatly bolstered by a laboratory setting.

Advances in atomic physics have led to extraordinarily precise frequency measurements, with frequency stabilities reaching down to 2×10^{-18} [32, 33]. Note that the precision of a measurement will be limited by the stability of its reference. One therefore needs two stable oscillators, such as two different atomic clocks [34], or two different transitions on the same atom [35]. In the case of constraining the variation of fundamental constants, there is an additional requirement that the two oscillators have different dependencies on the fundamental constant in question, otherwise both frequencies would drift at the same rate. The impressive precision in frequency measurements of atomic transitions has led to limits on the variation of fundamental constants comparable to that of astronomical measurements. At the time of writing, the best laboratory constraint on the fractional variation of α, $\dot{\alpha}/\alpha$, is 2.1×10^{-17}/yr [35].

Atomic clocks can also provide constraints on the dimensionless proton-to-electron mass ratio ($\mu = m_p/m_e$). It turns out electronic transitions have a very small dependence on μ [36]. The sensitivity mainly arises from hyperfine transitions via the nuclear magnetic moment [37]. Note that μ is not actually a fundamental quantity because the the proton consists of smaller fundamental particles. In actuality, a variation in μ corresponds dominantly to a variation of $\Lambda_{\rm QCD}/m_e$, where $\Lambda_{\rm QCD}$ is the quantum chromodynamics scale [38].

The best published laboratory limit on the variation of μ using the model of a drifting nuclear magnetic moment is 1×10^{-16}/yr [39], an order of magnitude larger than that for α.[1] This discrepancy stems from the precision available to hyperfine clocks, which have oscillator frequencies on the order of 10 GHz and precisions on the order of μHz, whereas these values for optical atomic clocks are 1 PHz and 1 mHz. In order to push these constraints even lower, a higher energy oscillator will be required.

1.2. Molecular Detectors

In comparison to hyperfine transitions, rovibrational transitions in molecules have a very straightforward dependence on μ, without the use of any additional models. In addition, their energies can be much larger than hyperfine transitions. For example, vibrational overtones in deeply bound electronic states can reach the optical domain. This will fundamentally allow constraints on μ-variation to reach the same order of magnitude as α-variation measurements, which is further motivated by predictions that μ will drift an order of magnitude faster than α [38].

Molecules unfortunately require significantly more effort than atoms to measure precisely. Spectroscopy at high precision requires repeatedly driving transitions between the same individual quantum states. Given that molecules additionally have vibrational and rotational degrees of freedom, it is more difficult to repeatedly prepare them in the same quantum state than it is for atoms. Certain molecules with exotic properties make this task easier [41, 42], although these molecules are seldom found in nature. Molecules can

[1]The tightest astronomical constraint on the variation of μ, measured by observations of methanol, is 2.4×10^{-17}/yr [40].

also have permanent dipole moments, which are more sensitive to external fields, leading to systematic frequency offsets. The difficulty in performing such measurements is reflected by the current best constraint of μ-variation set using a molecular transition: 5.6×10^{-14}/yr [43].

Doppler shifts will typically limit the precision of most molecular spectroscopy. One way to circumvent the challenge of translationally cooling molecules is to instead work with molecular ions in ion traps, and sympathetically cool the molecular ions using laser-cooled atomic ions [44, 45]. This procedure has been demonstrated to cool molecular ions [46, 47] and even proteins [48], to sub-Kelvin temperatures. The fewer trapped molecular ions, the further the temperature can be lowered. In the ultimate limit, molecular ions can be brought into the ion trap's quantum harmonic ground state [49, 50]. Measuring the internal state of a single molecule is however significantly more challenging than conventional fluorescence methods, although significant progress in quantum state detection has been made in recent years [51, 52].

1.3. Thesis Outline

This thesis chronicles the development toward high precision spectroscopy of a single molecule. Chapters 2 and 3 discuss different ways to produce the molecular ions that we are interested in measuring. Chapter 4 details additions made to the experiment designed to perform spectroscopy,[1] a method to perform quantum state detection and the expected spectrum of our molecule, AlH^+. Chapter 5 then describes in detail the properties that make a molecule most suited for a μ-variation measurement, where we identify TeH^+ as a candidate, and compare its features to other molecules.

[1]Previously described in Christopher Seck and Yen-Wei Lin's theses [53, 54].

CHAPTER 2

Interfacing Trapped Atomic Ions with Molecular Beams

2.1. Prologue

As mentioned in Chapter 1, the molecular ions we are often interested in are usually exotic. Knowledge of these molecules' internal structure, or even how to produce these molecules is lacking in the literature. The experiment described here provided a solution by creating a platform to create exotic molecular ions and study their chemical properties. The experiment combined two mature technologies: laser-cooled trapped atomic ions and molecular beams. Investigating ion-neutral chemistry in the sub-Kelvin regime can lead to new insights into low-temperature chemical reactions in space, a field known as astrochemistry. Additional motivations and details for this experiment can be found in Vaishnavi Rajagopal's thesis ([55]), who designed and constructed the apparatus. Here we reproduce one of the resulting publications from this apparatus [56], which leveraged the high density and spatial localization of molecular beams to achieve faster reaction rates in the production of exotic molecular ions. It also provided a method to characterize the molecular beam density without extra equipment.

2.2. High Density Pulsed Molecular Beam for Cold Ion Chemistry

In the past decade, researchers have steadily discovered an increasing number of exciting uses for trapped molecular ions. Topics ranging from cold chemistry [45, 57] to electron electric dipole moment searches [58] using trapped molecular ions have become

active areas of research, and interest in molecular ion preparation has led to a number of reaction rate measurements [59, 60, 61, 62]. Cold diatomic ions are typically formed by preparing laser-cooled alkaline earth metal atomic ions under ultrahigh vacuum (UHV) conditions and reacting them with neutral gas leaked into the chamber. Product formation rates are often limited by the amount of neutral gas that can be introduced, which is constrained by pumping speed and trap deloading. As an alternative neutral precursor source, a molecular beam provides a key relative advantage: a beam can be used to concentrate the flux of neutral reactants into the ion trap, increasing product formation rates over short time scales [63, 64]. As a result, the total amount of neutral gas required to achieve the desired number of molecular ions is reduced. Here we demonstrate this concept in the context of cold trapped ions by using a pulsed molecular beam source to form target molecular ion species from atomic ion precursors, and we use the trapped ions to directly measure the density profile.

To characterize our beam we exploit the previously-studied $Ba^+ + N_2O \rightarrow BaO^+ + N_2$ reaction [60]. Using a linear Paul trap ($2z_0 = 17.8$ mm, $r_0 = 4.6$ mm), we prepare a Doppler-cooled Coulomb crystal [65] of Ba^+ ions in the path of the molecular beam. The trap is housed in an ultrahigh vacuum chamber (Kimball Physics $6.0''$ spherical octagon) held at approximately 5×10^{-11} torr. We form Ba^+ in the trap by selectively photoionizing the ^{138}Ba isotope from a barium oven situated below the trap [66]. The trap is operated with a 3 MHz radio frequency (rf) drive; typical rf and end cap voltages are between 1.0-1.2 kV and 5-15 V, respectively. The ions are Doppler cooled with overlapping cooling (493 nm) and repumping (650 nm) lasers along the trap axis and are imaged with an EMCCD camera. Further details of the apparatus can be found in Refs. [55] and [67].

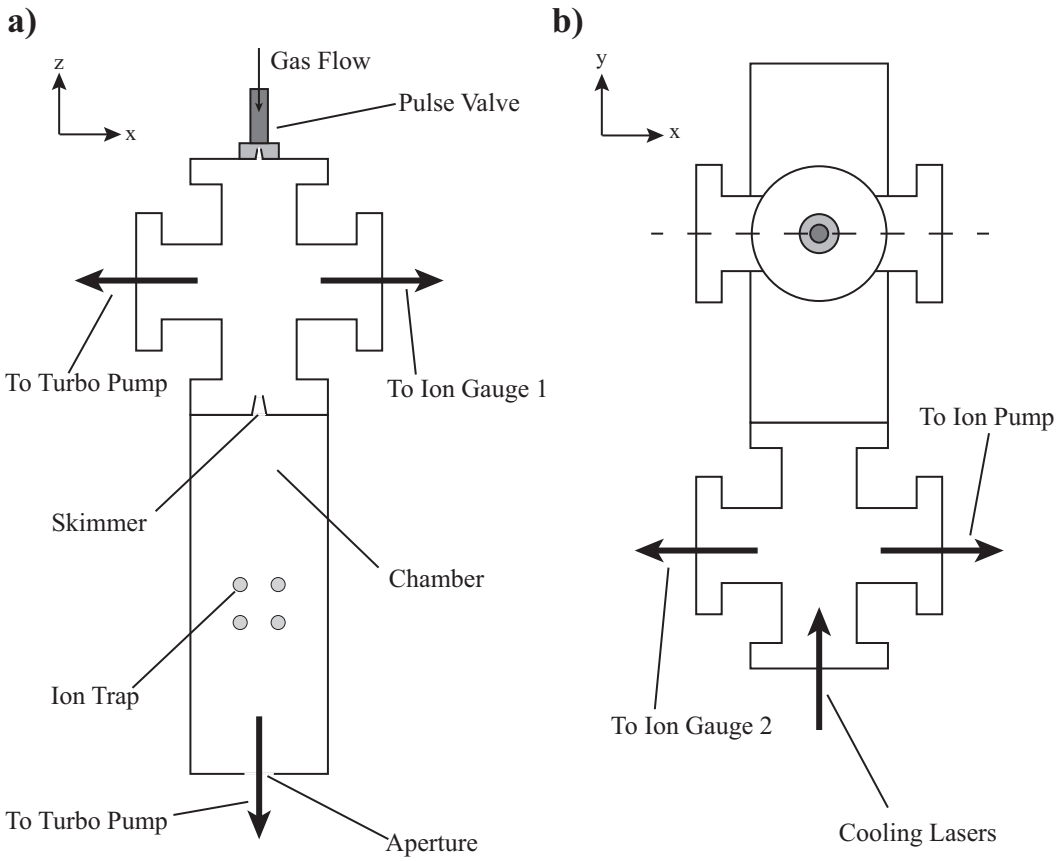

Figure 2.1. a) Reactant gas enters through the pulse valve, is collimated by the skimmer, passes through the ion trap and exits through an aperture opening to the turbo pump. b) Top view of the apparatus with the cross section (a) taken along the dashed line.

The N_2O reactant gas is introduced into a differentially pumped configuration (Fig. 2.1) through a previously-characterized solenoidal pulse valve (Parker series 9, 0.5 mm, conical nozzle) [68] with typical backing pressures between 6-10 psig. We drive the valve opening with a 200 V pulse for 210 μs. Upon opening the poppet, the gas supersonically expands into a differential pumping chamber and is collimated using a 1 mm skimmer located 137 mm downstream, which provides passage into the main reaction chamber (where the trap

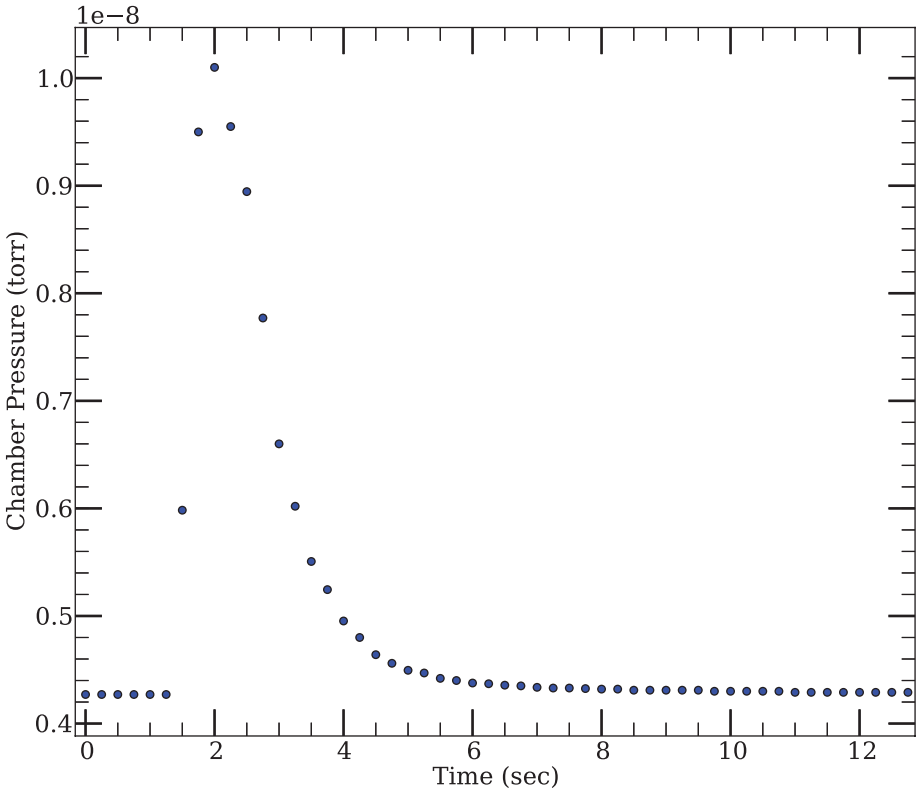

Figure 2.2. Temporal pressure profile after driving the pulse valve for 200 μs seen here beginning at 1.25 s.

is located). The distance between the pulse valve opening and the trap center is approximately 225 mm. The differential pumping chamber is connected to a turbo pump, while the reaction chamber is pumped with an ion pump and a turbo pump with a small aperture. The reaction chamber exit leading to the turbo pump is fixed opposite the skimmer entrance with an aperture of 2 mm, effectively creating a reverse differential pumping configuration. Fig. 2.2 shows the temporal profile of the reaction chamber pressure after a typical pulse of gas, measured from Ion Gauge 2 (Fig. 2.1).

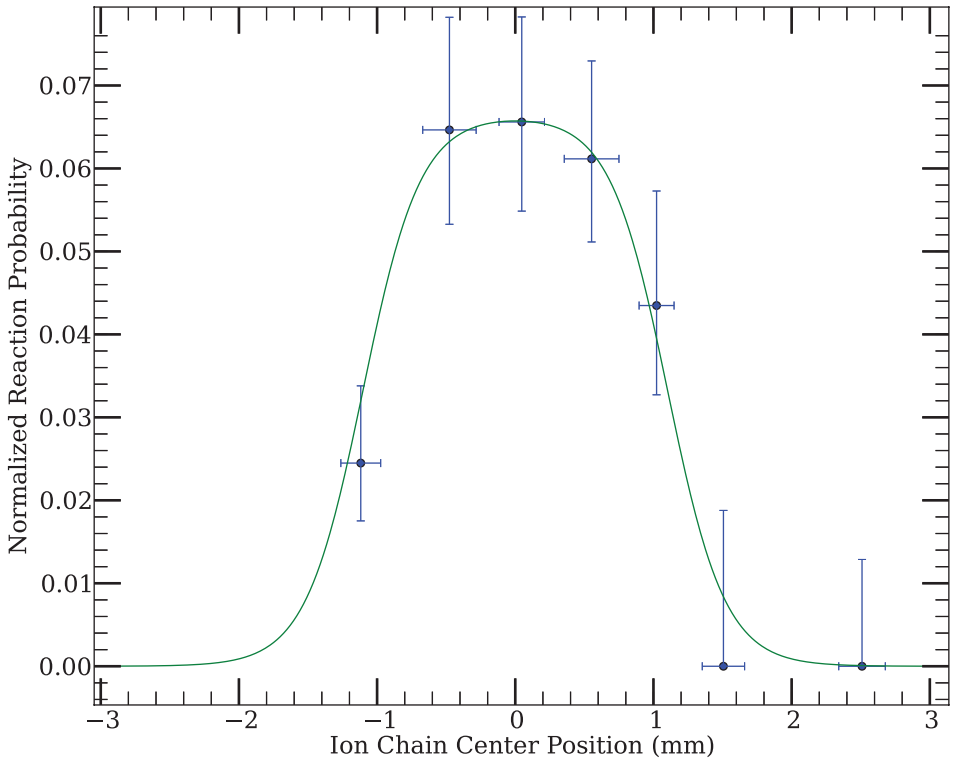

Figure 2.3. Reaction probability measurements with the ion crystal at different positions along the trap axis. The x uncertainty is given by the average ion crystal length for each bin. The y uncertainty refers to the 1σ confidence intervals for a Poisson process.

Ba^+ ions fluoresce (bright) during Doppler cooling while the sympathetically cooled BaO^+ ions do not (dark). In order to characterize the reaction rate, we measure the number of bright ions before and after a pulse of N_2O. The ratio of the number of new dark ions to the original number of bright ions represents the reaction probability per ion per pulse. Though highly exothermic, the reaction products remain trapped because the ion trap potential well is deeper than the reaction enthalpy. Using this ratio, we quantitatively characterize the molecular beam profile in the trap's axial direction by

changing the position of the target ions and measuring the reaction probability after a pulse of neutral gas. A typical string of 5-40 ions each separated from one another by approximately 15 μm is moved by varying the ion trap's axial offset voltage. Fig. 2.3 shows the measured beam profile. The high goodness of fit is a result of having four degrees of freedom in the fitting function. See Ref. [69]. The FWHM beam width (2.2 mm) and edge width (0.2 mm) were estimated by fitting to a bi-exponential as in Ref [69]. Assuming a conical expansion with the valve's conical angle of 45°, a beam width of 1.5 mm is expected at the trap center, in fairly good agreement with our measurement. Imperfections in the skimmer construction can change its behavior to more of an effusive source, which would broaden the beam [70]. The beam-like character of the gas jet is also qualitatively established by fluorescence transient dynamics. When the ions are in the path of the beam, the ion crystal melts, a result of heating induced by collisions with the neutral gas. During this time, the overall drop in fluorescence as well as ion de-localization is observed with the EMCCD (Fig. 2.4). This behavior is not observed for ion crystals positioned a few millimeters from the beam center, confirming that high neutral gas pressures are truly localized.

In a single pulse, the number of ions reacted ΔN is approximately given by:

$$\Delta N = k' N_0 \tau \tag{2.1}$$

$$k' = k\rho \tag{2.2}$$

where N_0 is the starting number of fluorescing atomic ions and τ is the pulse duration. The neutral gas density is much larger than that of the trapped ions and is unaffected

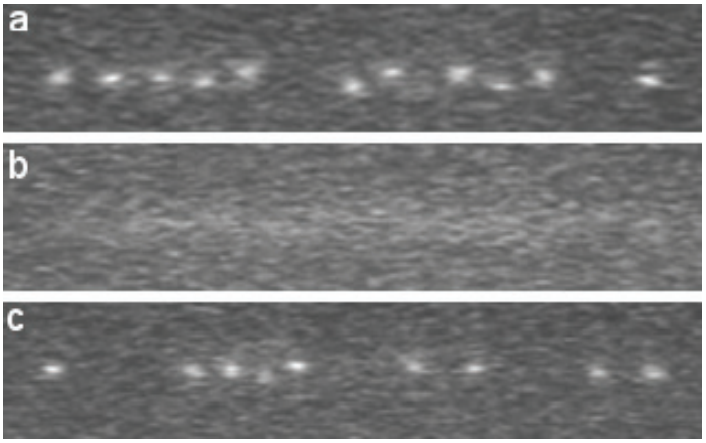

Figure 2.4. Typical measurement with ions in the path of the beam. a) Initial count of 11 ions. b) Melted ion string immediately after pulse of neutral gas. c) Final count of 9 bright ions.

by the reactions. Eq. 2.2 defines the pseudo-first order rate constant $k^{'}$, where ρ is the number density of the neutral gas and k is the bimolecular rate constant.[1] Energetically, Ba^+ must be in the excited state in order to react [60]. Its average excited state population is assumed to remain constant over the timescale of the pulse, because Ba^+ is constantly excited by the always-on Doppler cooling lasers. Using our measured peak reaction probability ($\Delta N/N_0$) of 0.066 per ion per pulse and the previously measured rate constant (0.016 s^{-1}) [60], we estimate a number density (ρ) of $10^{11}/cm^3$ over a time period of 0.5-1 ms.[2] For comparison to a typical leak valve scenario, our reaction rate corresponds to leaking in neutral gas at 10^{-9} torr ($\sim 10^7/cm^3$) for approximately 2 seconds. As an illustrative example, one can consider reaction rate measurements outside the beam as being equivalent to those from a leak valve; the ratio of the peak reaction

[1]Reaction rates leading to products other than BaO^+ are assumed to be negligible under these conditions, as observed in Ref. [60]. We identify the correct mass of BaO^+ using the imaging technique described in Ref. [67].

[2]The pulse duration is estimated based on previous characterization of the same model pulse valve in Ref. [68]

rate to that outside the beam represents the overall reduction in gas. For our apparatus we observe no reactions outside the beam. Using Poisson statistics, this allows us to set a 68% confidence-limit lower bound of five on this ratio.

In order to achieve higher reaction rates, higher pulse valve backing pressures could be managed with an improved reverse differential pumping configuration. A majority of the high-density molecular beam that passes through the trap flows directly into the exit on the opposite side, with the aperture mitigating backscattered gas re-entering the reaction chamber. By using an aperture diameter a few times larger than in the current design or by achieving better beam collimation, we could reduce the transient background pressure from each pulse (Fig. 2.2.) Under these improved conditions, we could then operate our pulse-valve backing pressure up to 1250 psi and increase the reaction probability per pulse. We note that operating at higher backing pressures leads to increased beam-broadening [70], which would need to be compensated by aperture size or beam collimation technique.

In summary, we have assembled a pulsed molecular beam in conjunction with laser-cooled trapped ions. In contrast to a previous pulsed beam experiment [61], we manipulate the positions of the ions to directly characterize the beam's spatial density profile. We show that higher reaction rates can be achieved while avoiding high background chamber pressures. These results serve as a proof of principle demonstration for broadening the scope of molecular ion species for which cold chemistry can be investigated. Pulsed molecular beams are particularly advantageous when low duty cycles can be tolerated, [71] such as synchronizing gas pulses with trapped molecular ions having short excited state

lifetimes. Observing such reactions would often be unfeasible using a leak valve due to the unacceptably high chamber pressures required.

CHAPTER 3

Production of Molecular Ions

3.1. Prologue

The origin of this project was to improve the experimental duty cycle of the AlH^+ optical rotational cooling experiment [72], where the rate limiting step was the production of AlH^+. The procedure was to first load Al^+ ions into the trap and then allow time for Al^+ to react with background gas until all of it converted to AlH^+, which occurred over a few minutes.[1] Ideally, we would follow the same procedure described in Chapter 2, where we could increase reaction rates by pointing a high density beam of a hydrogen donors at the trapped Al^+ ions. Unfortunately, the well depth of the X state of AlH^+ is only 0.7 eV [42], which poses a unique challenge. Not only are there few gaseous species that have hydrogen bonds weaker than 0.7 eV, but also the weak bond energy makes AlH^+ highly likely to donate its hydrogen to another species. The latter issue is especially problematic because the quantum state detection scheme for AlH^+ involves measuring a ratio of Al^+/AlH^+ [73], which requires starting with a pure collection of AlH^+ ions. Our trap geometry also precluded easy ejection of Al^+ without also ejecting AlH^+.

Given the challenges of reacting Al^+ to form AlH^+, we instead decided to create a source of neutral AlH, which we can selectively photoionize into AlH^+ using resonance

[1] The hydrogen donor was never identified.

enhanced multi-photon ionization (REMPI). We produced a separate chamber to demonstrate the effectiveness of the AlH source. We originally implemented an AlH source in a manner identical to that of [74]. While it successfully produced a beam of AlH, the source's short lifetime was ultimately incompatible with our ultrahigh vacuum chamber. We then switched to a laser vaporization source. The details of which are described in [75], reproduced below. More information about the construction of the source can be found in Appendix A.

3.2. Introduction

The ability to trap and prepare molecular ions in a well-defined state can pave the way for achieving new quantum computing schemes [76], cold and state-controlled chemistry [45] and precision tests of fundamental symmetries [77, 78, 79]. For trapped molecular ions, resonance enhanced multi-photon dissociation (REMPD) is commonly used to perform state readout due to its high efficiency [80, 81, 82]. However, the destructive nature of the measurement requires frequent trap reloading, creating a unique set of criteria for the molecular ion source. The source should present a minimized gas load during pulses, to maximize the duty cycle of experiments requiring ultra-high vacuum (UHV) conditions. Using a source that presents a low heat load also minimizes outgassing degradation of the vacuum. Due to these stringent requirements, out of the many molecular ions of potential interest, a disproportionate number of labs have chosen to work with molecular ions that can be created simply from Doppler-cooled atomic-ion precursors [83, 50].

Loading of ions directly from a laser-ablated target can meet many of the above criteria [84], with extra steps sometimes required to purify the trapped ion sample. [85]. However,

this technique requires a suitable ablation target, and the large energies of ejected ablation products can present practical challenges when loading multiple species. A pure ionic sample can also be loaded by selectively photoionizing a neutral precursor formed using laser vaporization [82]. In this scenario the laser vaporization can be done inside a nozzle that produces a molecular beam directed toward an ion trap [86], effectively isolating the ionic byproducts from the ion trap. This method allows for production of a wider range of molecules, because the high density of the carrier gas inside the nozzle can be used as a reactant when forming ablation products in UHV.

We improve upon this type of laser vaporization source by implementing a cylindrical nozzle entirely composed of transparent fused silica, providing a number of advantages. First, implementations of laser vaporization nozzles have typically had an aperture that allows the ablation laser to reach the target, leading to depressurization of the nozzle and decreased molecular flux [86]. Using a transparent material for the nozzle removes the need for an aperture, preserving ablation products within the beam. Sealed nozzles have been used with similar intentions [87, 88]; however, the compact design of the fully transparent nozzle avoids large block assemblies consisting of a window and multiple channels. Second, the small inner volume of the nozzle reduces the overall gas load needed to achieve a molecular beam. Lastly, if the ablation target requires heating, the low thermal conductivity of fused silica reduces the undesirable heat flow leaving the target region, reducing vacuum degradation. Fused silica also outgasses more easily than commonly used nozzle materials such as stainless steel or alumina [89]. Here we implement this nozzle design and demonstrate a stable source of aluminum monohydride (AlH) as a means to rapidly load the aluminum monohydride cation (AlH^+) into an ion trap.

Exploiting its highly diagonal Franck-Condon factors, AlH^+ was used to demonstrate fast rovibronic ground state cooling in an ion trap [72]. AlH^+ was previously formed by exposing 10's of trapped Al^+ ions to increased background pressures. Conversion to AlH^+ occurred over the course of a few minutes, making trap loading the experimental rate limiting step by a couple orders of magnitude [73]. To trap a pure sample of AlH^+ ions, one can instead selectively photoionize its neutral precursor AlH inside the trap. We use our nozzle to implement a molecular beam in order to deliver high densities of AlH to the ion trap. Laser ablation of aluminum in the presence of hydrogen gas leads to the formation of AlH and heavier aluminum hydrides [90]. In order to provide a stable, long-lasting flux of AlH we prepare a liquid aluminum target [88]. Using this nozzle design we demonstrate stable production of AlH with no degradation observed over hour time scales. We use a (2+1) resonance enhanced multi-photon ionization (REMPI) process in order to perform spectroscopy on AlH and form AlH^+ [91]. This source can be used to efficiently provide an ion trap over 100 AlH^+ ions in a few seconds.

3.3. Experimental

3.3.1. Apparatus Overview

The apparatus (Fig. 3.1) consists of two chambers: an expansion chamber and a six-way cross detection chamber separated by a four-way reducing cross that houses an ion deflector. The deflector, used to remove ionic ablation products, is realized by applying a high voltage ($\sim$500 V/cm over 3.5 cm) to a plate that extends as far as possible without completely obstructing the beam path. A mesh is placed on the opposite side in order to enhance the field near the molecular beam without obstructing the turbomolecular pump.

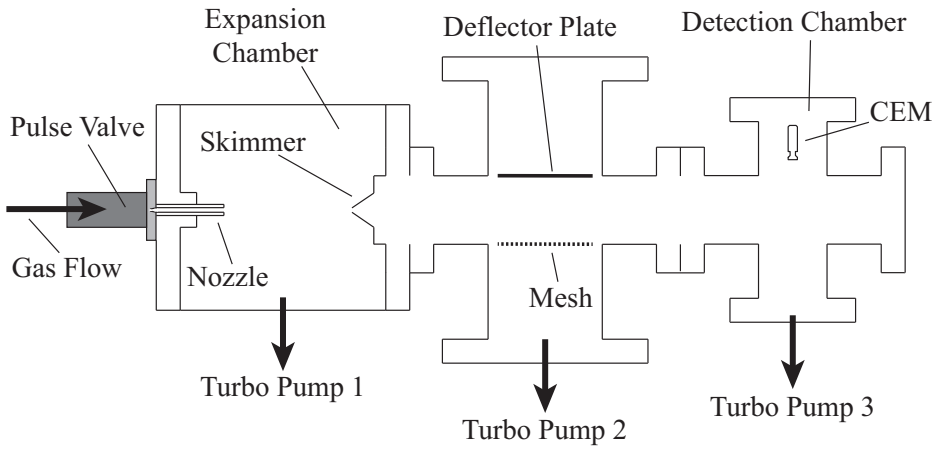

Figure 3.1. AlH detection apparatus (not to scale). AlH emanating from the nozzle expands with the carrier gas. Ablation ions are extracted from the resulting molecular beam using a deflector plate. AlH is subsequently photoionized to form AlH^+, which is detected with a CEM.

The two chambers are separated by a skimmer (1 mm aperture, 20° inner, 25° outer half angle), which is mounted to a custom adapter plate mounted to a reducing flange. The chambers and the reducing cross are each pumped with a separate 50 l/sec turbomolecular pump.[1] The expansion chamber additionally consists of an ion gauge, a viewport on top and a nozzle. The nozzle is fitted to a custom flange consisting of copper feedthroughs and a ConFlat connection to a Parker Series 99 pulse valve. The pulse valve is driven at 10 Hz using 200 V for 95 μs letting in H_2 with a backing pressure of 2 bar. The average pressures in the expansion and detection chambers with the pulse valve activated are 5×10^{-4} and 1×10^{-6} torr, respectively. Both chambers reach 1×10^{-8} torr with the pulse valve deactivated. The detection chamber has two viewports perpendicular to the molecular beam axis, which the photoionization beam passes through. The photoionization product is detected with a Photonis Magnum 5900 channel electron multiplier (CEM) perpendicular to the view

[1]A separate turbomolecular pump for the reducing cross was not essential to AlH beam formation.

ports and molecular beam. The CEM resides 30 cm downstream from the nozzle exit and its opening is situated 1 cm from the molecular beam axis.

3.3.2. Nozzle

The nozzle (Fig. 3.2) is designed to overlap ablated liquid aluminum with a pulse of hydrogen. It consists of a 5.7 cm long fused silica tube (6.35 mm OD, 1.9 mm ID) that extends down to the pulse valve entrance and is held in place by a Swagelok Ultra-Torr fitting welded to the flange [74]. By using a transparent material, we avoid having to drill a hole for the ablation laser to pass through on its way to the sample target. Such a hole would depressurize the nozzle, leading to a decreased molecular flux. Using diamond-tipped drill bits in a water bath, we drill a 2 mm hole on the bottom side of the nozzle diameter that allows aluminum vaporized in the oven (described below) to enter the nozzle. The area around the opening is filed down such that the the nozzle can be seated inside the 4 mm opening of the oven, forming a press-fit seal. In addition, an 8 mm deep cone is drilled into the exit of the nozzle, such that the base of the cone is 3 mm from the oven exit hole. Allowing the beam to expand as soon as possible helps mitigate cluster formation [92]. The cone full angle is 30°, which additionally helps collimate the beam [93].

The boron nitride oven (Kurt Lesker EVC10BN) holds solid pellets of 99.999% aluminum. Boron nitride is inert to molten aluminum, ensuring that the aluminum does not move once melted. A saddle-shaped clamp with a hole in the center is draped over the nozzle, holding the oven tightly by grabbing onto the upper lip of the oven.[1] This

[1]See Appendix A for more information.

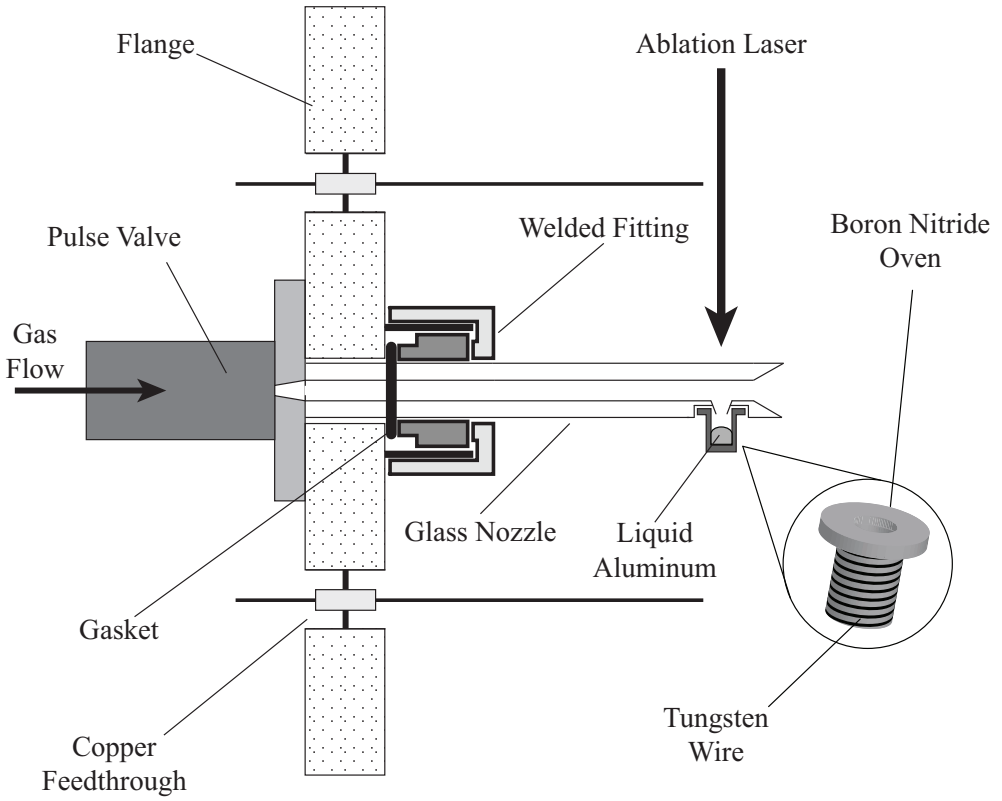

Figure 3.2. Cross section of the nozzle assembly (not to scale). The clamp holding the boron nitride oven to the glass tube is not shown.

prevents the oven from moving during heating and helps seal any gaps between the oven and the glass. The hole in the clamp allows transmission of the ablation laser. Tungsten wire (0.375 mm diameter) is wrapped around the oven in order to provide heat. A snug fit is achieved by first wrapping the tungsten wire around a $\frac{1}{4}$-20 screw ($\sim$7-8 turns). This molds the tungsten wire into a coil having slightly smaller diameter than the 6.35 mm oven. The tungsten wire is connected to the copper feedthroughs using beryllium/copper inline barrel connectors. Melting of aluminum was observed at 6.5 A, 4 V; the tungsten wire glows red around the oven and yellow where the wire is not touching the oven. The

ablation laser (532 nm, 10 Hz, 10 ns), is focused with an f = 150 mm lens. Initial measurements were performed with 11 mJ per pulse. Care must be taken not to ablate the walls of the glass tube as this causes the tube to crack, preventing the ablation laser from reaching the target.

3.3.3. Detecting Photoions

To find the photoionization signal we use an OPOTEK Magic Prism Optical Parametric Oscillator (OPO) pumped by the 3rd harmonic (355 nm) generated from a Spectra Physics Quanta Ray Pro-270 Nd:YAG laser. The OPO is specified to emit a broad linewidth (20 cm^{-1}), which is expected to enhance the signal due to its ability to cover multiple rotational transitions. For these procedures we measured approximately 10 mJ of REMPI light entering the chamber. The light is focused to the molecular beam axis with an f = 200 mm lens and we use a photon counter (SRS SR400) to count individual ion events from the CEM. Because the AlH product yield is lower than that of aluminum, we first measured aluminum photoions. Aluminum has two strong (2+1) REMPI lines at 445.2 nm and 446.3 nm [94], conveniently close to AlH's Q branch transition centered at 448.5 nm [91].

Note that the nozzle acts as a cylindrical lens and further focuses the ablation laser, leading to higher intensities. Effective ablation of the aluminum target can be confirmed by visually observing a "spark" where the ablation laser contacts the target [86]. We observe that the highest photoionization signal occurs with the REMPI beam focused directly under the CEM and centered on the molecular beam's axis. As is common for laser vaporization sources, we find the signal to be very sensitive to both the REMPI

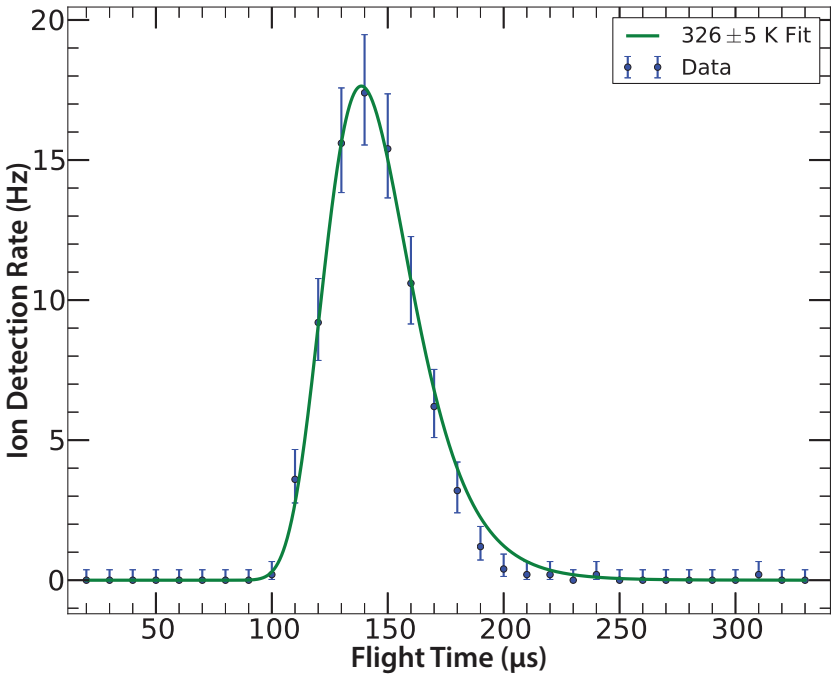

Figure 3.3. Time-of-flight profile for AlH with temperature fit from [9]. Error bars correspond to 1σ confidence intervals for a Poisson process.

and ablation pulse delays relative to the pulse valve trigger [95]. Ablating the molten aluminum target also leads to a background signal of ionic ablation products. However these ablation ions can be distinguished from REMPI ions due to their different arrival times at the CEM (10's of microseconds versus 150 μs) and are also mitigated by the ion deflector. A photodiode detects the arrival of the REMPI laser pulse in order to more easily facilitate synchronous detection of REMPI products. The REMPI ions are found to arrive at the CEM 700 ns after the REMPI pulse.

Due to the similarity in mass, Al and AlH have very similar velocity profiles. Switching to the Q branch of AlH (448.5 nm) led to a smaller photoionization signal. After rescanning the REMPI (Fig. 3.3) and ablation pulse delay times, the AlH signal was then further optimized by increasing to higher hydrogen backing pressures and adjusting the

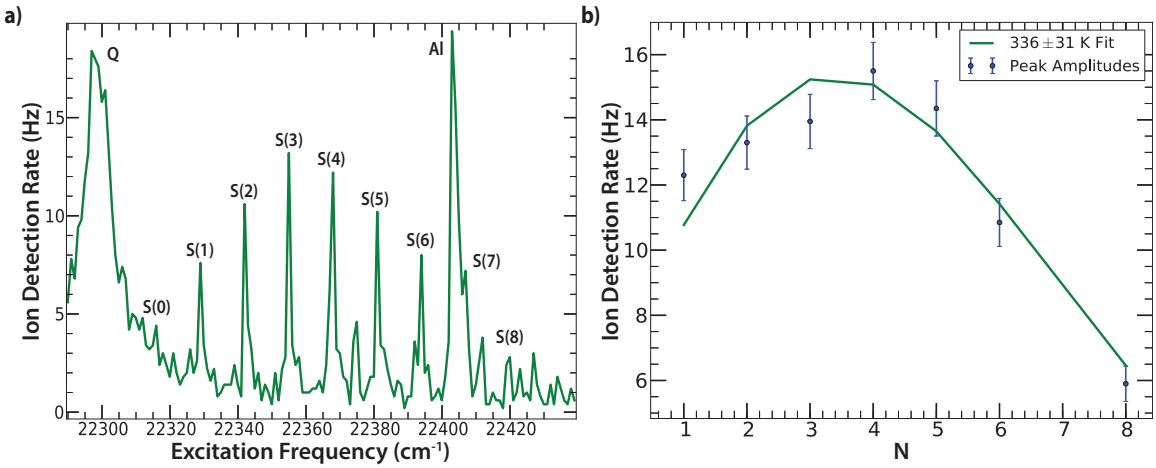

Figure 3.4. a) REMPI spectrum of the molecular beam. b) Rotational temperature fit to peak amplitudes of different S-branch transitions. S(0) and S(7) are omitted due to spectral interference. Error bars correspond to 1σ confidence intervals for a Poisson process.

ablation pulse intensity. We observe a signal saturation with increasing ablation pulse energy (2 mJ), and at higher intensities droplets of aluminum eject from the oven. We find that these droplets react with the glass, irreversibly altering its surface. We have also used deuterium as the carrier gas and confirm AlD's Q-branch peak at 448.1 nm, deduced using spectroscopic constants from [74].

3.4. Results

3.4.1. AlH Spectroscopy

After optimizing the signal, we then switch to a narrow linewidth pulsed laser (0.06 cm^{-1}, Sirah PrecisionScan, Coumarin 450) and perform spectroscopy. Fig. 3.4a shows a spectrum taken with 2 mJ of REMPI light focused with an f = 200 mm lens, integrating 5 seconds per point. The Q and S branches are easily identified. The spacing of the S-branch peaks yields a ground state rotational constant of 6.36 ± 0.03 cm^{-1}, in close

agreement with the literature [74]. The large narrow peak corresponds to the (2+1) 3p-7p REMPI transition in aluminum [94]. The spectrum is largely free of spectral interference, confirming that AlH is selectively photoionized. The strength of the S-branch transitions can also be used to assign a rotational temperature of 336 ± 31 K (Fig. 3.4b). This temperature corresponds well with the translational temperature of 326 ± 5 K obtained from the time-of-flight profile data. The translational temperature represents an upper bound because no correction was made to the fit for the time the gas resides in the nozzle. Although substantial cooling has taken place from the molten source, the temperature is fairly high compared with what can be achieved in typical supersonic expansions. We attribute this somewhat high temperature primarily to the low conductance of our compact apparatus (50 l/s pumping speed) compared to other conventional systems (4500 l/s) [86]. Colder rotational and translational temperatures in the same apparatus could presumably also be achieved by lowering the pulse repetition rate as was performed in [96]. Lower temperatures can also be reached by using a smaller nozzle inner diameter, minimizing the required gas load and allowing the expansion chamber to reach lower average pressures.

3.4.2. Long-Term Signal Stability

To demonstrate the long-term stability of the source, we tune the OPO to the center of the Q branch. As seen in Fig. 3.5, the ion production rate remains stable over hour timescales, also indicated by the symmetric nature of the histogram. In the first few hours of source operation, we observe a slight decrease in signal of ∼10% in 3 hours. During the measurement, we also observe a gray/black film coating the inner wall of the glass nozzle. The ablation laser simultaneously back-ablates this film off of the inner nozzle

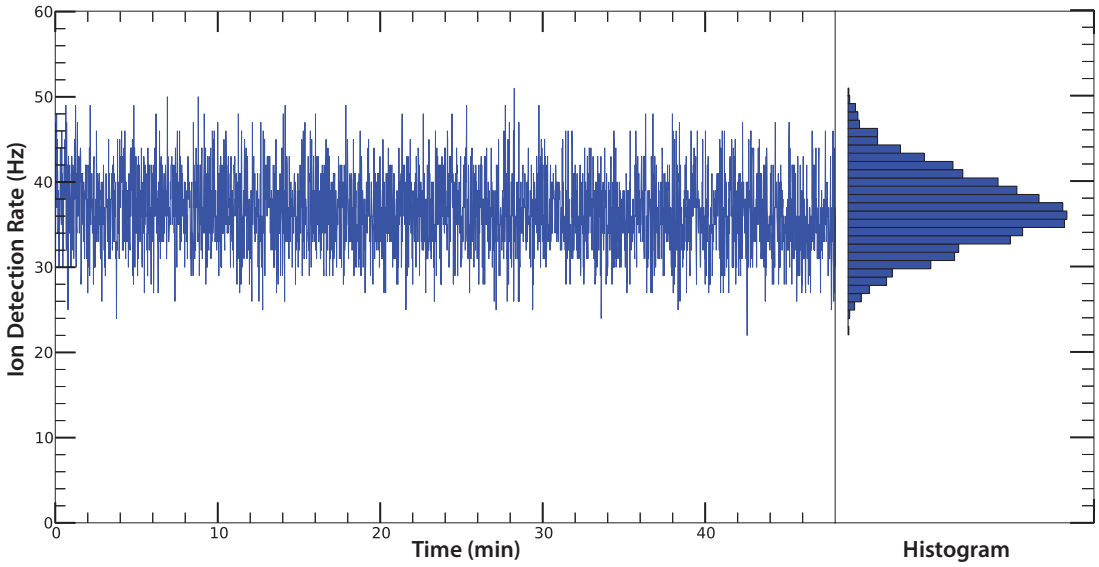

Figure 3.5. AlH^+ production rate at a constant frequency monitored over long timescales, as time series as well as associated histogram. Background ion production at this wavelength was found to be negligible.

wall, leaving a transparent circle for the ablation laser to reach the aluminum target [97]. After many pulses the rate of coating and back-ablation come to an equilibrium and long-term signal stability is reached. The inner nozzle wall can be cleaned off in this way by translating the ablation laser along the nozzle.[1]

We also conducted measurements with a nozzle containing a 1 mm hole for the ablation laser. Over time Al coats the upper viewport. Due to the lower ablation laser intensity at the viewport (compared to at the nozzle inner wall), the viewport must be cleaned periodically with higher ablation laser power in order to recover signal. Although this nozzle design provides a long-term AlH photoionization signal, the AlH flux is more than a factor of two smaller than that produced with the closed nozzle.

[1]Outside vacuum, a concentrated solution (2M) of potassium hydroxide (KOH) or sodium hydroxide (NaOH) is sometimes used to clean aluminum from the glass surface. The reaction releases bubbles of hydrogen gas.

3.5. Conclusion

We have demonstrated a long-term stable, pulsed beam of AlH from which AlH^+ can be produced via (2+1) REMPI. Using a transparent nozzle we forgo having to drill a hole for the ablation laser, allowing for increased overall beam intensity and lower internal and external temperatures. The compact size of the nozzle allows for easy integration with many UHV systems. The nozzle also accommodates using a molten Al target, providing a stable AlH flux due to the constant and smooth surface topography over many ablation pulses. We have demonstrated a 330 Kelvin AlH source and provide suggestions for reaching lower rotational and translational temperatures. Our AlH beam is directed toward an ion trap, so that AlH can be photoionized leading to a pure trapped sample of AlH^+. Because AlH itself is a Doppler cooling candidate [98], a stable beam of AlH could also potentially be used to realize laser slowing and trapping of AlH.

3.6. Epilogue

Although in [75] we used (2+1) REMPI to measure the spectrum of AlH, this is likely not the best method to produce AlH^+. Photoionizing AlH this way also produces Al^+ ions [91], the mechanism for which has not been confirmed. Two potential mechanisms could be: tunnelling into the $Al^+ + H^-$ potential well while populating the C state during REMPI [99], or the high photon flux required to photoionize AlH might be large enough to photodissociate AlH^+.

To avoid the production of Al^+, we will instead photoionze AlH using (1+1') REMPI, where the first photon pumps AlH to the A state (426 nm), and the second photon, generated via second harmonic generation of 426 nm (213 nm), will photoionize AlH.

Using this method, the C state will not be populated, and the lower energy required for the 1-photon processes should avoid any photodissociation out of the ground state of AlH^+.

CHAPTER 4

Toward High Precision Spectroscopy of a Single Molecular Ion

4.1. Introduction

This experiment aims to perform the most precise measurement of a molecular transition with the intention of setting a new constraint on the variation of the proton-to-electron mass ratio. We plan to perform quantum logic spectroscopy (QLS) on a single AlH^+ ion [100], using a co-trapped Ba^+ ion. A prerequisite to achieving QLS is being able to demonstrate state detection and motional ground state cooling of the Ba^+ logic ion. The apparatus and the procedures used to achieve the latter are described in excellent detail in Part 3 of [53], and will therefore not be repeated here. This chapter will describe new developments made, experimental and theoretical, toward demonstrating high precision spectroscopy of AlH^+.

4.2. Production of AlH^+

After demonstrating ground state cooling of Ba^+ [10], the next step was to implement a method of loading AlH^+ into the ion trap. As discussed in Section 3.1, AlH^+ production requires special care due to its high reactivity. Chapter 3 provides a method to reliably produce AlH^+ via photoionization of neutral AlH; however, implementation of a molecular beam solution for this experiment requires extra care to prevent the degradation of vacuum that stems from constantly introducing the carrier gas into vacuum.[1]

[1]One solution would involve several stages of differential pumping.

An alternative solution is to ablate a solid material that liberates neutral AlH, which can be photoionized inside the ion trap. This method was not pursued in Chapter 3 due to the requirement of needing a large sample of pure AlH^+, whereas here we can keep reloading until a single ion of AlH^+ is successfully loaded. Fortunately the species $LiAlH_4$, which is solid at room temperature, was shown to release high densities of AlH upon ablation [101]. We have also considered other AlH-containing species such as $NaAlH_4$ and $KAlH_4$, although ablation of these species is likely to produce large amounts of easy-to-ionize sodium and potassium ions. The mass of these ions is close enough to the mass AlH^+, making them likely to falsely appear as a successful loading attempt until confirmation using resolved sideband mass spectrometry [83]. One major drawback of $LiAlH_4$, however, is that it begins to decompose at 150 °C [102]. This makes achieving ultrahigh vacuum pressures of 10^{-11} torr more challenging and time consuming.

4.2.1. Ante-Chamber

We instead designed a solution that circumvents the problem by attaching an ante-chamber to the science chamber, separated by a gate valve. Fig. 4.1 is an image of the apparatus, which going from left to right consists of: a 24" rack and pinion translator (Kurt Lesker LRPSSG324MNM), a 4.5" to 2.75" reducing cross, a 20 L/s ion pump, an ion gauge, a 4.5" cube with blanks on the sides and a 4.5" viewport on the top, two rotatable minimum-length nipples,[1] and a gate valve (Kurt Lesker SG0150MCCF). On the end of the translator is a 1/4-28 tapped hole, to which we attached a custom made sample holder with two cups: one for producing the logic ion and the other for the spectroscopy

[1]These were necessary to attach the ante-chamber to the science chamber because the valve's bolts do not line up with those of the science chamber.

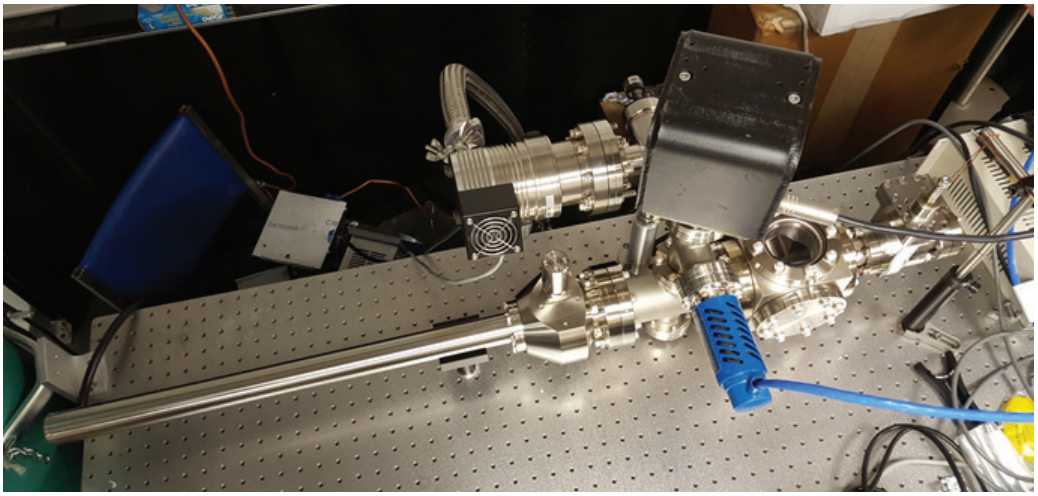

Figure 4.1. Ante-chamber separated from the science chamber.

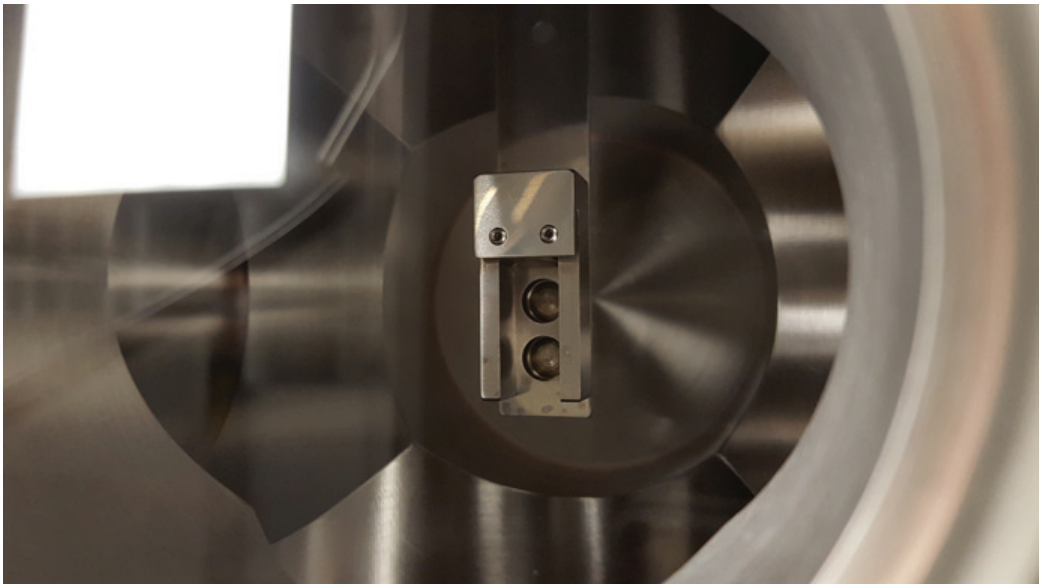

Figure 4.2. End of the sample holder.

ion (Fig. 4.2). On the end of the sample holder is custom machined set of walls to prevent ablation products from spraying onto parts of the trap. On the top are two set screws and a slit that were originally designed to hold a 1"x1" square of ITO-covered glass. This glass square would have a hole drilled above each of the samples, such that one could send

the ablation laser through the glass and the ablation products would only exit through the hole. Although the latter idea was meant to prevent the build up of ablation products on the ion trap, leading to patch potentials, similar experimental setups did not observe drastic decreases in heating rates after long term use.[1] We therefore did not implement the glass slide. The sample holder is fixed to the translator with a vented 1/4-28 silver-coated vacuum screw. Machine drawings for the sample holder and the attachment are available in Appendix D.

One complication with the gate valve is that with the actuator attached, the maximum bakeable temperature is 60 °C, even though the gate valve can be baked to 150 °C with the gate valve closed. The limitation is presumably due to the grease used to lubricate the actuator. This might be able to be circumvented by using thermally resistant grease. With the actuator removed and the the valve held open, the valve can be baked to 200 °C. The ante-chamber was first pre-baked with a blank attached to the end before attaching it to the science chamber (Fig. 4.3).

After baking the ante-chamber, an 80/20 cage was made to transport the chamber. The ante-chamber was attached to where the feedthrough for the barium oven was originally connected. The attachment was done under flow of nitrogen, both from the science chamber and from the ante-chamber simultaneously to avoid needing to rebake the chamber. The attached chamber is pictured in Fig. 4.4. An image of the full apparatus can be seen in Fig 4.5,[2] and Fig. 4.6 shows the sample holder fully engaged under the trap. To remote control the motion of the translator, we attached a stepper motor (Applied Motion TSM11Q-1SM) with a 1:100 motoreducer. After attaching the ante-chamber, the

[1]Personal communication from Prof. Rainer Blatt's group.
[2]Note: some cable posts were edited out of the image.

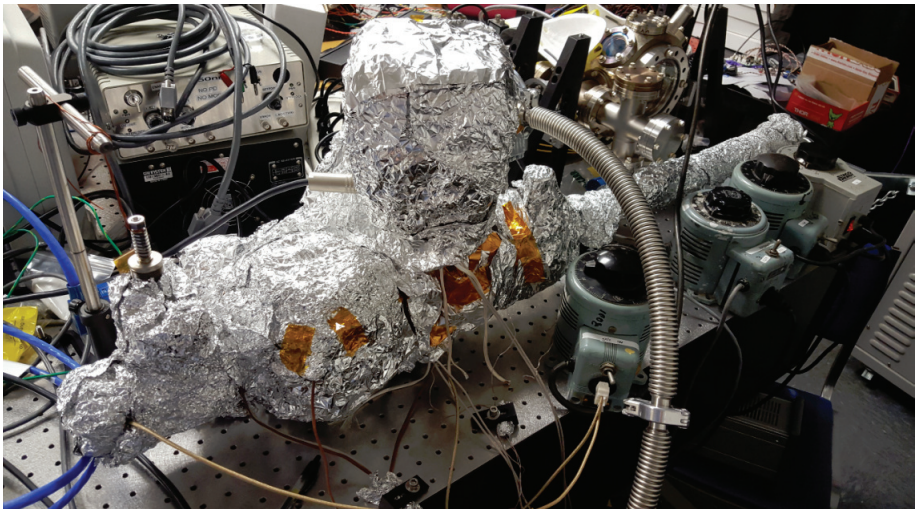

Figure 4.3. Baking the ante-chamber. The gate valve is manually held open with the actuator removed.

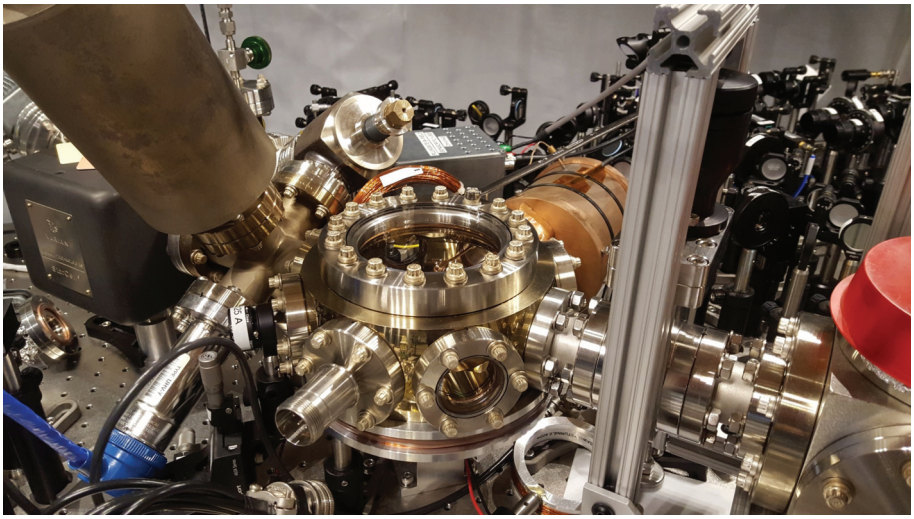

Figure 4.4. Ante-chamber attached to the science chamber. The ante-chamber rests on an 80/20 frame.

gate valve was closed and through the viewport, under flow of nitrogen, the samples were introduced onto the sample holder. The final pressure in the ante-chamber after pumping down without re-baking is $\sim 1 \times 10^{-9}$ torr. With the gate valve open, the pressure in the science chamber is $\sim 1 \times 10^{-10}$ torr. Once ions are successfully loaded into the

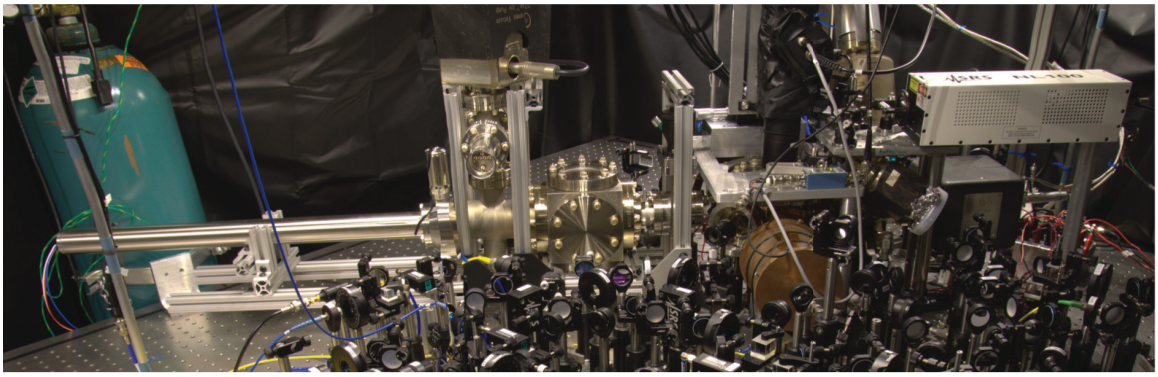

Figure 4.5. Full apparatus with imaging and ablation laser installed.

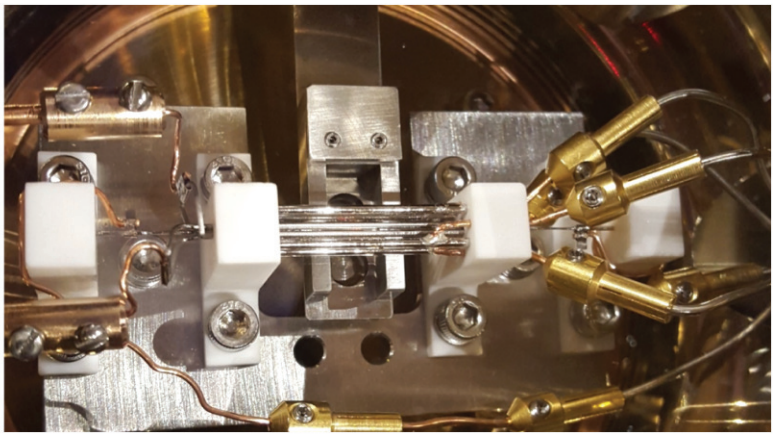

Figure 4.6. Sample holder under the ion trap.

ion chamber, we can retract the stage and close the gate valve, dropping the pressure in the science chamber down by a factor of two. This method of sample introduction can therefore be used to load more species into the chamber.

4.2.2. Imaging System

The upper flange of the science chamber was originally a re-entrant window designed to collect more fluorescence. However, in order to make room for an ablation laser from above, the flange was replaced with a 6" UVFS viewport flange (Fig. 4.6). We therefore

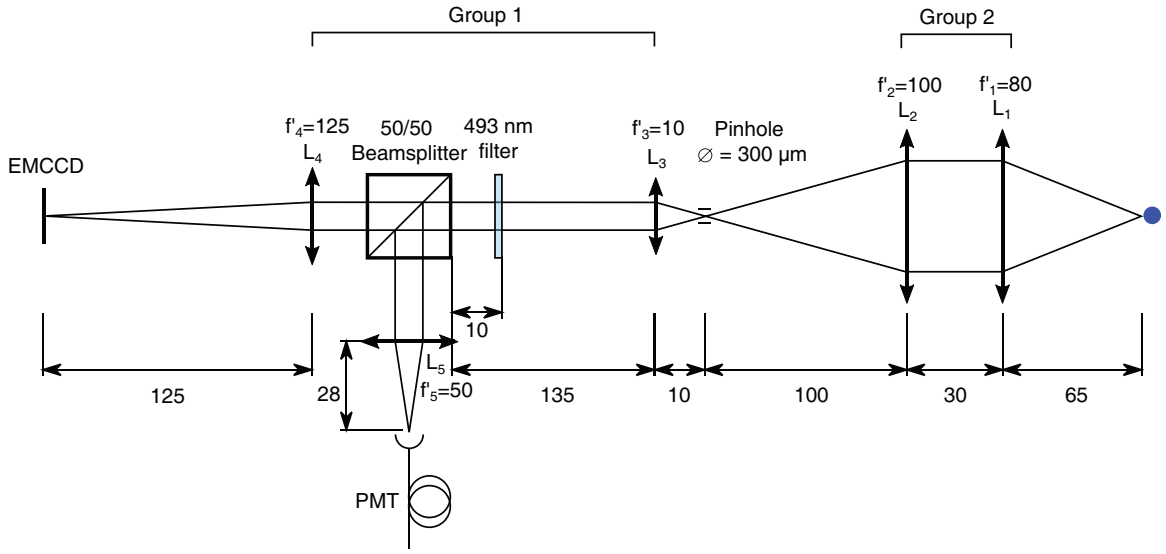

Figure 4.7. Imaging System.

had to construct a new imaging system, shown in Fig. 4.7. The system has a total magnification of 15.5, where each pixel is 0.645 μm in the object plane. The EMCCD is an Andor Luca S. We calibrate the overall collection efficiency using a single Ba^+ ion and a series of 493 nm and 650 nm pulses such that only one 493 nm photon is emitted per experiment. We measure an overall collection efficiency of 0.001.

Although the collection efficiency is adequate, the imaging system in Fig. 4.7 leads to serious spherical aberration, due to the Group 2 lenses being achromatic doublets (Thorlabs AC508). We designed a new system to replace the Group 2 lenses, shown in Fig. 4.8. This system replaces the two achromats with aspheres (Thorlabs AL50100-A), significantly reducing the spherical aberration. Because no f = 80 mm asphere was in stock, we placed an additional f = 300 mm achromatic doublet (Thorlabs AC508-300-A) in order to bring the focus to the necessary distance.[1]

[1]In this configuration the spherical aberration introduced by the achromat is minimal.

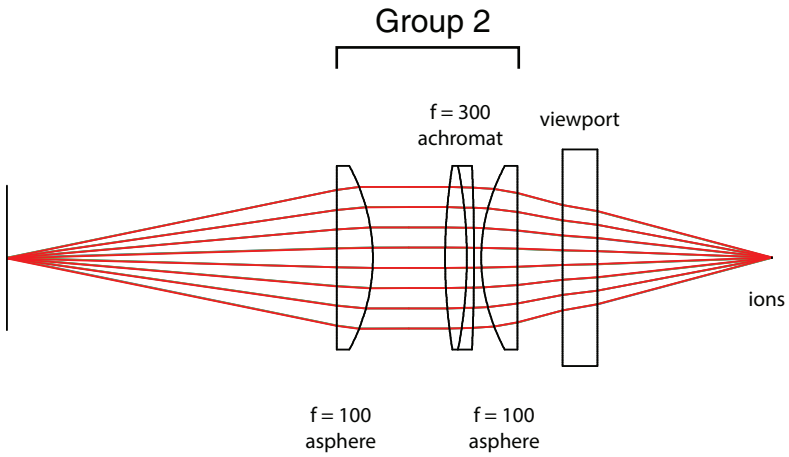

Figure 4.8. Upgraded Group 2 of imaging system.

4.2.3. Trap Loading

We use an SRS NL-100 nitrogen laser to ablate the solid samples, with typical pulse energies of 30-50 μJ focused with an f = 150 mm lens.[1] Because we need to produce different wavelengths to separately ionize Ba and AlH, we use a pulsed optical parametric oscillator OPO (Ekspla NT342C). For barium ionization we drive the 413.24 nm $^1S \rightarrow {}^3D$ transition. We optimize trap loading by tuning the relative delay between the ablation and photoionization pulses. When the delay is optimized, pulse energies of 10 μJ produce several ions in a single pulse. To load one Ba^+ we turn down the ablation power such that approximately 10 pulses produces one ion. We also leave the 80 MHz red-detuned 493 nm laser (near-resonant π in [53]) on during loading to speed up cooling.

For loading AlH^+ we use $(2+1)$ resonance enhanced multi-photon ionization (REMPI) tuned to the $X \rightarrow C$ transition in AlH at 448.5 nm, using approximately 2 mJ of pulse energy. Although this technique may produce Al^+ ions, attempts at ground state cooling and motional state detection can be made with either Al^+ or AlH^+. We may switch to

[1]The rectangular beam shape of the nitrogen laser does not focus well.

the (1 + 1') REMPI scheme described in Section 3.6 to more reliably produce only AlH^+. In order to avoid doubly-ionizing the barium ions with the photionization, we purposely move the focus of the photoionization beam approximately 100 μm away from the trap center, in the axial direction. For loading exactly one AlH^+ ion, the procedure can be made easier using the technique in [103].

4.3. Motional Ground State Cooling

4.3.1. Ion Mass Ratio

The mass ratio of Ba^+/AlH^+ is 4.9. Because the ions have vastly different individual secular frequencies, energy transfer between them is inefficient. The cooling limit for both ions actually does not depend on the ion mass ratio [104]; however, the larger the mass ratio, the longer it will take to reach to cooling limit. Methods to increase the rate of sympathetic cooling are discussed in [105]. Another consideration is that for mass ratios greater than 4, the radial motion is essentially decoupled from the axial motion [104], which is problematic because the radial the spectroscopy ion will not be cooled along this axis. Techniques for cooling ions with a large mass ratio (3.9) are presented in [106]. One method is to operate in a regime where the radial and axial secular frequencies are similar, in order to facilitate the transfer of energy.[1] The authors in [106] successfully demonstrate motional ground state cooling in this regime.

Another consideration mentioned in [106] is the number of lasers needed to keep two ions with large mass ratios crystallized. Slow cooling rates make the ion pair vulnerable to melting after a collision with background gas. The authors of [106] use multiple Doppler

[1]Note that this increases ion micromotion [104].

cooling lasers at various red detunings in order to achieve crystallization when using the $^{171}Yb^+$ ion, which they mention is due to the ion's lower scattering rate. They also mention that multiple lasers are not required when using the even isotope $^{174}Yb^+$. We observe similar behavior in that no additional lasers are necessary to crystallize $^{138}Ba^+$ and AlH^+, although the melting rate is decreased when turning on our 80 MHz red-detuned 493 nm laser.

4.3.2. Motional Mode Spectrum

Before attempting to ground state cool a Ba^+-AlH^+ ion pair, we first focused on a simpler scenario where the dark ion is a different isotope of Ba^+. The techniques for near-resonant Raman sideband cooling, driving logic gates and state detection described in [53] were used here to take a motional spectrum of Ba^+ and an ion with (at-first) unknown in mass, shown in Fig. 4.9. For conciseness, Fig. 4.9 contains three separate datasets plotted on the same axes. For each experiment, the π-time for the far-off-resonant Raman beams was optimized for each resonance. Fitting the spectrum leads to the determination of the dark ion as $^{137}Ba^+$.

Several conclusions about the experiment can be drawn from Fig. 4.9. The contrast on the carrier and sidebands is smaller than that demonstrated for a single ion [10], which is likely due to the higher final crystal temperature in the two-ion scenario. At the time of this measurement, we could only perform near-resonant Raman sideband cooling on one of the normal mode red sidebands. Not cooling both axial modes leads to a degraded signal, parametrized by the Debye-Waller factor [107]. Modulation of the RF for the

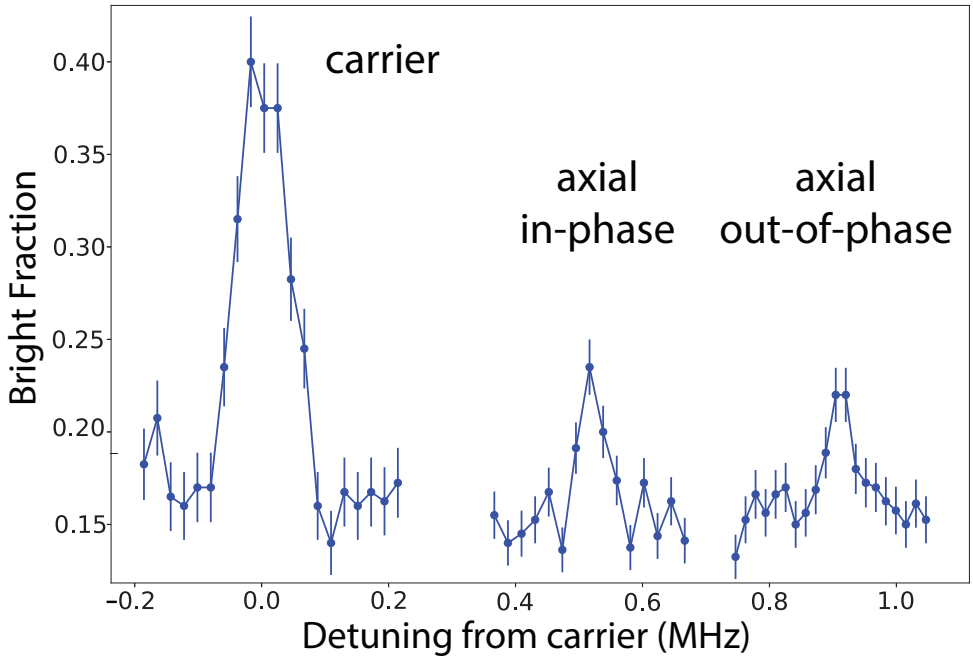

Figure 4.9. Resolved sideband spectrum. Note that each peak corresponds to a separate experiment, with the π-time optimized for each resonance.

AOMs controlling the near-resonant Raman beams has been implemented in order to drive both sidebands simultaneously.

Fig. 4.9 also shows that decoherence is currently limiting the experiment, as the π pulses on the blue sidebands do not transfer the population with near-100% efficiency. While incomplete motional ground state cooling will contribute to this short coherence time, we only achieve coherence times on the order of 150 μs even for a single ion, which suggests that likely other factors such as noise in our magnetic field coils are the main source of decoherence. For a $^{138}Ba^{+}$ Zeeman qubit, coherence times of 100 μs have been raised to 4 ms by actively stabilizing the magnetic field [108]. The effects of motional dephasing can also be eliminated while searching for sources of decoherence by altering the configuration of our Raman beams [109].

The laboratory room also suffered severe temperature swings, which led to one of the several involved beamlines to drift over the course of the measurement. To combat this, the near- and far-off-resonant Raman beams and the shelving/deshelving lasers were combined into two separate optical fibers, which significantly helped mitigate the issue. Other potential improvements to the experiment are mentioned in [53].

4.4. Photon Recoil Readout

The eventual goal is to perform quantum logic spectroscopy (QLS) on a single AlH^+ ion, which coherently maps the internal state information onto a co-trapped atomic ion, from which state detection can easily be performed. Proceeding with this method as a first attempt, however, would be very challenging because successfully driving coherent operations requires knowledge of the transition strength. Because transitions at our desired precision have never been measured in AlH^+, it would be more ideal to first implement an incoherent form of survey spectroscopy. This was impressively demonstrated on a CaH^+ ion by performing spectroscopy, state transfer and state detection all in a single step [52]. This technique is completely general to any molecule, although it requires driving molecular transitions on their blue sidebands, which are suppressed by the Lamb-Dicke parameter squared (typically $\sim$100-fold). Suppressed line strengths are an added difficulty when surveying already weak vibrational overtones with narrow linewidths. To circumvent this difficulty we aim to separate the spectroscopy and state transfer steps.

After state preparation into the ground vibrational state, a narrow-linewidth laser can be used to drive vibrational overtones at high precision. We then only require that our state transfer operation be conditional on whether the ground vibrational state is still

occupied, assuming the excited state lifetime is long. If the initial state is $|X, v = 0\rangle$, one method would be to repeatedly drive absorption-emission events to an excited electronic state: $|A, v = 0\rangle$. After several scattering events the two ions will warm up, and the induced motion can be detected on the co-trapped atomic ion. The origins of this technique can be traced to a technique called sympathetic heating spectroscopy [110]. An improvement to this technique involves driving absorption events in phase with the motional frequency of the ion pair, amplifying the motion and minimizing the number of required scattering events [111, 112, 113]. Because this process is separate from the actual spectroscopy step, we call it photon recoil readout (PRR).

For most molecules, however, this technique will not be efficient due to vibrational branching into $|X, v = 1\rangle$, which will typically be out of resonance with the driving laser. Therefore this technique is only suitable for molecules with abnormally small vibrational branching ratios such as AlH^+ [42]. For AlH^+ the branching ratio of $|A^2\Pi_{1/2}, v = 0\rangle \rightarrow |X^2\Sigma, v = 0\rangle$ to $|A^2\Pi_{1/2}, v = 0\rangle \rightarrow |X^2\Sigma, v = 1\rangle$ is approximately 32:1, which effectively sets our "photon budget", i.e. we need to detect induced motion on the co-trapped atomic ion with fewer than 32 scattering events on average. How to detect motion within this photon budget is described in the following section.

4.4.1. Predicted Signal

We are interested in implementing a procedure to measure whether or not there is an electron in the vibrational ground state of AlH^+: $|X^2\Sigma, v = 0\rangle$. The PRR protocol for AlH^+ is shown in Fig. 4.10. Both Ba^+ and AlH^+ are first prepared in the motional ground ground state. Motion is induced by repeatedly driving the $|X^2\Sigma, v = 0\rangle \rightarrow |A^2\Pi_{1/2}, v = 0\rangle$

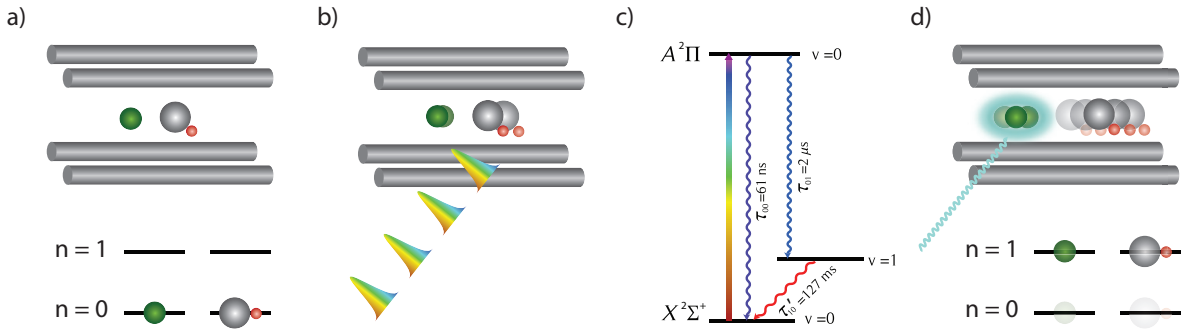

Figure 4.10. Photon Recoil Readout. a) Both ions are prepared in the motional ground state (n = 0). b) Electronic excitation on the molecule is driven inducing motion on both ions. c) Absorption and emission can continue until off-diagonal decay into an excited vibrational state halts the process. d) The introduced motional energy can be measured on the atom using standard motionally-dependent electron shelving techniques, followed by fluorescence detection [10].

transition. State detection is then performed on Ba^+ by first driving a red sideband transition on the Zeeman interval, and then the spin state is measured via electron shelving and fluorescence [53]. For a first demonstration we can avoid rotational state preparation entirely by driving the electronic transition with a broadband laser (Section 4.4.2). To determine how many photon recoil events on the molecule are necessary to introduce one quanta of motion on the ion pair, we need to understand how adding energy to one ion transfers energy to the ion crystal. This information is encoded in the Lamb-Dicke parameter, which for a single ion is:

$$\eta^2 = \frac{\omega_R}{\omega_z}, \tag{4.1}$$

where ω_z is the secular frequency in the z direction, and ω_R is the recoil energy imparted to the ion upon absorbing or emitting a photon:

$$\omega_R = \frac{\hbar k_z^2}{2m}, \tag{4.2}$$

where the wavevector $k_z = 2\pi\lambda^{-1}\cos(\theta)$ and m is the mass of the ion. If the ion starts in the motional ground state, the probability of being taken out of the ground state is approximately:

$$P \sim 1 - e^{-N^2\eta^2}, \tag{4.3}$$

where N is the number of recoil events, assuming that each recoil event coherently adds momentum $i\eta$ [113, 114, 115]. Eq. 4.3 shows that readout performed in this manner is very efficient due to the exponential scaling.

For a two ion system in one dimension, we instead have two normal modes, one where the ions oscillate in-phase and one out-of-phase. Although our measurement will detect induced motion on one of these modes, the recoil events will only occur on one ion. We therefore need to calculate the "effective" Lamb-Dicke parameters for each normal mode, given an absorption event on a single ion. A full derivation is given in Appendix B. Here we summarize the key results necessary to calculate the effective Lamb-Dicke parameters.

We assume two ions in a one-dimensional harmonic trap along the Z axis, one with mass m_1 and the other with mass μm_1, where the ion mass ratio $\mu = m_2/m_1$.[1] The trap potential is such that a single ion of mass m_1 has a secular frequency of ω_z along the Z axis.[2] The normal mode frequencies are:

$$\omega_{\pm}^2 = \frac{\omega_z^2}{m_1}\left(1 + \frac{1}{\mu} \pm \sqrt{1 - \frac{1}{\mu} + \frac{1}{\mu^2}}\right), \tag{4.4}$$

[1]The mass ratio μ here should not be confused with the proton-to-electron mass ratio m_p/m_e.
[2]ω_z can be calculated from experimental trap parameters using Eq. 4 of [116], for example.

where the lower energy ω_- is the in-phase mode and the higher energy ω_+ is the out-of-phase mode. The effective Lamb-Dicke parameters are calculated using:

$$\begin{aligned} \eta_1^{ip} &= k_z^{(1)} A_- \sqrt{\frac{\hbar}{2\omega_- m_1}} \qquad \eta_1^{op} = k_z^{(1)} A_+ \sqrt{\frac{\hbar}{2\omega_+ m_1}} \\ \eta_2^{ip} &= k_z^{(2)} B_- \sqrt{\frac{\hbar}{2\omega_- \mu m_1}} \qquad \eta_2^{op} = k_z^{(2)} B_+ \sqrt{\frac{\hbar}{2\omega_+ \mu m_1}} \end{aligned} \tag{4.5}$$

where $k_z^{(1)}$ and $k_z^{(2)}$ are the wavevectors along the Z direction for light resonant with a given transition in ion 1 and 2, respectively, and:

$$A_\pm = \left(\frac{1}{1 + \left(1 - \frac{1}{\mu} \mp \sqrt{1 - \frac{1}{\mu} + \frac{1}{\mu^2}}\right)^2 \mu} \right)^{1/2}, \tag{4.6}$$

$$B_\pm = \left(1 - \frac{1}{\mu} \mp \sqrt{1 - \frac{1}{\mu} + \frac{1}{\mu^2}}\right) \sqrt{\mu} A_\pm, \tag{4.7}$$

which are the components of a transformation matrix used to transform into the normal mode picture.

For our experiment Ba^+ is the logic ion, from which it is easiest to measure ω_z. Ba^+ has a mass $m_1 = 138$ amu. We perform logic operations driving Raman transitions on the $S_{1/2} \rightarrow P_{1/2}$ transition between $S_{+1/2}$ and $S_{-1/2}$, which in our configuration leads to $k_z^{(1)} = \sqrt{2}(2\pi)/(493 \text{ nm})$.[1] For exciting motion on AlH^+ ($m_2 = 28$ amu), we drive the $|X^2\Sigma, v = 0\rangle \rightarrow |A^2\Pi_{1/2}, v = 0\rangle$ transition at 361 nm at a 45 degree angle to the trap axis: $k_z^{(2)} = (\pi\sqrt{2})/(361 \text{ nm})$. For a single Ba^+ ion in our trap, an endcap voltage of approximately 9.5 V leads to a secular frequency in the axial direction of $\omega_z = 2\pi \times 248$ kHz. At this voltage with one Ba^+ and one AlH^+ in the trap, using Eq. 4.4 yields an

[1]Note that for Raman transitions, we need the Δk_z wavevector [53].

	IP	OP
η_{Ba^+}	0.194	0.0310
η_{AlH^+}	0.0774	0.179

Table 4.1. Absolute values of the effective Lamb-Dicke parameters for each normal mode driving Ba^+ and AlH^+ separately.

in-phase and out-of-phase mode frequency of $\omega_- = 2\pi \times 295$ kHz and $\omega_+ = 2\pi \times 801$ kHz, respectively. Plugging these values into Eq. 4.5 yields the effective Lamb-Dicke parameters for each mode; their absolute values are presented in Table 4.1.

Because the number of scattering events on AlH^+ is scarce, we choose to drive the out-of-phase mode, which has a large effective Lamb-Dicke parameter of 0.179. A more accurate prediction of the number of required scattering events takes into account the photon statistics [114]:

$$S(\overline{N}) = \sum_{N=0}^{\infty} P(N)\mathcal{P}(N, \overline{N}) \tag{4.8}$$

where $P(N)$ is the excitation probability for N scattering events (Eq. 4.3) and

$$\mathcal{P}(N, \overline{N}) = \frac{\overline{N}^N e^{-\overline{N}}}{N!}, \tag{4.9}$$

where $\overline{N}$ is the average number of scattering events necessary to reach a signal $S(\overline{N})$. Eq. 4.8 suggests only $\overline{N} = 10$ scattering events on average is needed to reach a signal of 0.89.

The penalty for needing so few photons to excite motion on the out-of-phase mode is more difficulty measuring the excitation on the Ba^+ ion, which has an effective Lamb-Dicke parameter of only 0.03. Because the sideband Rabi frequency is suppressed by the Lamb-Dicke parameter, readout on the Ba^+ ion requires approximately 39 times more laser

power than that required to measure the in-phase mode. Despite this power requirement, accommodating state detection on the Ba^+ ion is the simpler choice.

The opposite scenario involves driving excitation of AlH^+ on the in-phase mode ($\eta^{op}_{AlH^+}$ = 0.0774), which would only require 21 scattering events to reach the same signal of 0.89. This number of scattering events is also within the photon budget of AlH^+ and makes detection on Ba^+ simpler; however, this option will introduce new difficulties. Specifically, the measurement needs to be made faster than the heating rate for each mode, so that we know for sure any introduced motional excitation is from the molecule rather than the environment. Not only is the heating rate faster on the in-phase mode [104], but because the in-phase mode frequency is smaller than the out-of-phase mode, it also takes longer to excite 21 scattering events on the in-phase mode. This then requires consideration of the AlH^+ excitation laser, detailed in the following section.

4.4.2. AlH^+ Excitation Laser

The broadband laser used drive the $|X^2\Sigma, v = 0\rangle \rightarrow |A^2\Pi_{1/2}, v = 0\rangle$ transition is a Spectra-Physics Tsunami (3941-M1BB), pumped with a Spectra-Physics 15 W Millenia eV. The laser outputs 100 fs pulses at 80 MHz with an output power of 4 W at 720 nm. The light is doubled using a BBO crystal and can be pulse-shaped to perform rotational cooling [53]. In order to synchronize the excitation laser with the motional modes of the ions, we need to step down the 80 MHz repetition rate using a pulse picking system. Fig. 4.11 shows the schematic.[1] We send the laser through a ConOptics Model 350-160-01 KD*P Series E-O Modulator, driven by a ConOptics Model 25D Driver. The pulses are gated using a

[1]The pulse picking system was designed by Vincent Carrat.

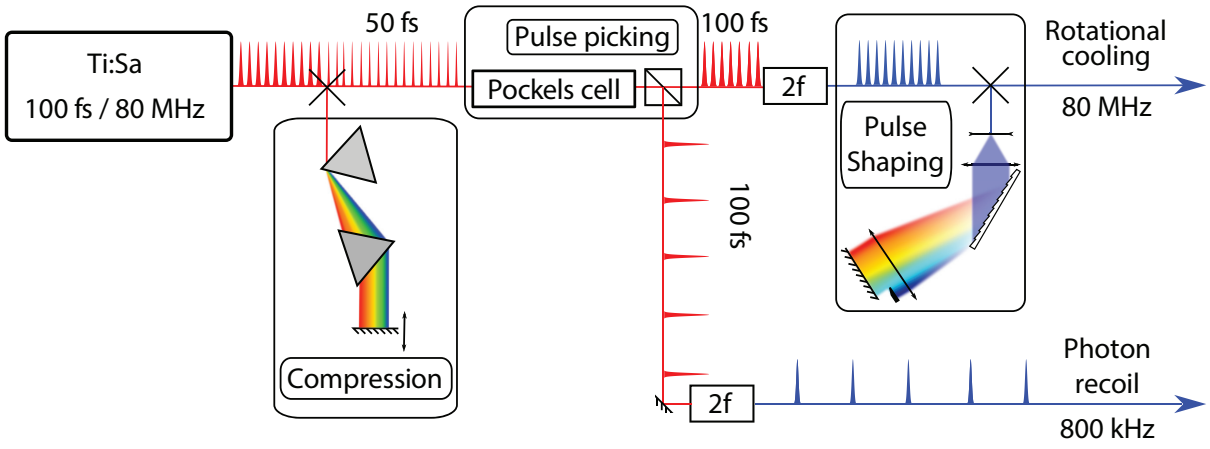

Figure 4.11. Rotational cooling and photon recoil readout beamlines.

ConOptics Model 305 Synchronous Countdown System, which gives us control over how many pulses to skip in order to bring the repetition rate down to ∼800 kHz. We measure a contrast in pulse power of 100:1. For this reason we pick pulses before the second harmonic generation stage, in order to increase the contrast to 10000:1. However the pulse picker introduces dispersion into the pulses, which we measure using a Grenouille (Swamp Optics 8-60-USB). This dispersion will degrade the doubling efficiency, we therefore also include a pulse compressor (Swamp Optics BOA-8-TU-315) before the modulator in order to pre-compensate for the dispersion. The unpicked beamline will be used for rotational cooling of AlH^+ [72].

Note that pulse picking simultaneously solves another problem: the linewidth of the $|X^2\Sigma, v = 0\rangle \rightarrow |A^2\Pi_{1/2}, v = 0\rangle$ transition is $2\pi \times 2.4$ MHz and the frequency comb spacing is 80 MHz, which can lead to the excitation laser missing the resonance. By pulse picking the repetition rate down to 800 kHz, a comb tooth is then guaranteed to be within the

linewidth of the transition.[1] Assuming a uniform intensity over the pulse bandwidth after doubling, only 1 part in 3.85×10^6 will go into the transition.

The saturation intensity (I_{sat}) of the $|\text{X}^2\Sigma, v=0\rangle \rightarrow |\text{A}^2\Pi_{1/2}, v=0\rangle$ is approximately 70 μW/mm^2. With a doubling efficiency of 50% and focusing the laser to a 100 μm diameter spot, we can achieve a saturation intensity of 0.94 I_{sat}. Assuming we lose one hundredth of the power after pulse picking (0.01 I_{sat}), the scattering rate would be $\sim 7.5 \times 10^4$ s^{-1}. To induce 10 scattering events, the required illumination time would then be: 130 μs

As a first demonstration of PRR, the lifetime of the $|\text{X}^2\Sigma, v=1\rangle$ state can be measured. The excitation laser can first pump the population out of the $|\text{X}^2\Sigma, v=0\rangle$ state. After ground state cooling, one can measure the PRR signal as a function of time. However, because the lifetime is predicted to be 127 ms, it may be necessary to perform ground state cooling continuously.[2]

4.4.3. Spectroscopy protocol

With non-destructive state detection of $|\text{X}^2\Sigma, v=0\rangle$ in hand, spectroscopy of the vibrational overtones of AlH^+ can be performed. Spectroscopy to the $|\text{X}^2\Sigma, v=3\rangle$ state in AlH^+ will provide the maximum sensitivity to a variation of μ.[3] The 67 ms lifetime of the $|\text{X}^2\Sigma, v=3\rangle$ manifold also presents the opportunity to perform molecular spectroscopy at an unprecedented Hz level. Higher precision spectroscopy can reveal higher order inner

[1] This problem will need to be addressed for the rotational cooling setup, either by warming the ion ([117]) during rotational cooling or destroying the comb structure of the laser, e.g. modulating the femtosecond laser's pump power.
[2] Note that some pulse shaping may be required as the laser may drive transitions out of $|\text{X}^2\Sigma, v=1\rangle$.
[3] See Section 5.2, Eq. 5.7.

couplings of AlH^+, yielding new physical intuition than can also serve as a benchmark for *ab initio* calculations. Such couplings also find use in enhancing sensitivity to drifts in fundamental constants, which occurs when two states belonging to different degrees of freedom coincide in energy [118].

The spectroscopy protocol using photon recoil readout (PRR) would be almost identical to that shown in Fig. 4.10: i) both the logic and spectroscopy ion are prepared in their motional ground state, ii) the spectroscopy laser is applied to the spectroscopy ion for an appropriate duration,[1] and iii) PRR is used to determine if a transition on the molecule successfully occurred; motion will only be induced if the molecular transition was unsuccessfully driven.

The $|X^2\Sigma, v = 0\rangle \rightarrow |X^2\Sigma, v = 3\rangle$ transition has an energy of 2450 nm, which can be accessed using a commercial OPO,[2] and transmits through UV fused silica viewports with 85% efficiency. The transition has a dipole moment of 0.01 Debye. For the eventual goal of demonstrating quantum logic spectroscopy, we need to drive red sideband pulses on AlH^+ on this transition. Using the derived results and conditions from Section 4.4.1, the corresponding effective Lamb-Dicke parameter for this transition would be 0.025. Achieving a modest Rabi frequency of $2\pi \times 100$ kHz, would require focusing 127 mW of the laser to a 100 μm diameter spot. Driving the carrier transition would require over three orders of magnitude less power. This estimate assumes the laser has a linewidth narrower than the $2\pi \times 2.4$ Hz natural linewidth, which will require stabilization to a high-finesse cavity.

[1]The pulse duration will depend on the linewidth and power of the spectroscopy laser in order to achieve a high transition probability.
[2]The Lockheed Martin Argos SF-15, for example.

4.5. Internal Structure of AlH^+

High precision spectroscopy at the Hz level will resolve transitions beyond that of traditional ro-vibrational spectroscopy. Preliminary spectroscopy requires a general intuition of the internal molecular structure, in order to make sense of any spectrum. The procedure for making a reliable prediction of the molecular spectrum is outlined in the following sections. This section makes generous use of footnotes, which provide reference to specific equations or passages in books that cover this subject much more extensively.

4.5.1. Refining the Effective Hamiltonian

The ultimate goal of spectroscopy is to relate what we measure to physical processes inside the molecule, by which we develop physical intuition. More specifically, we attempt to construct an accurate Hamiltonian of our system. Our measurement corresponds to transitions between eigenstates of the exact molecular Hamiltonian ($\mathcal{H}$). However, we cannot fit our spectrum to $\mathcal{H}$ because $\mathcal{H}$ possesses an infinite number of eigenstates. We instead construct an effective Hamiltonian ($\mathcal{H}_{\text{eff}}$) that closely corresponds to the subspace in which our experiment operates. Although $\mathcal{H}_{\text{eff}}$ does not represent the exact Hamiltonian, we can add higher order perturbative terms to $\mathcal{H}_{\text{eff}}$ within the framework of perturbation theory.[1] $\mathcal{H}_{\text{eff}}$ ultimately serves as a model that physically describes the interactions within the molecule. The relative strengths of these interactions are characterized by their respective molecular constants, which we determine by fitting $\mathcal{H}_{\text{eff}}$ to our spectra. Higher precision spectroscopy can refine these molecular constants, or even reveal new interactions within the molecule.

[1]The derivation of $\mathcal{H}_{\text{eff}}$ from $\mathcal{H}$ using perturbation theory is detailed in Section 7.2 of [7]).

The validity of the effective Hamiltonian depends upon the perturbation elements between states being small compared to energy spacing between states. In general the coupling between low energy electronic states is small relative to electronic transition energies. Similarly, diatomic hydrides tend to have small reduced masses, leading to large vibrational spacings. This motivates the use of an effective Hamiltonian that describes a single vibronic manifold $|\eta, \Lambda, v\rangle$, where v is the vibrational quantum number, Λ is the projection of the orbital angular momentum onto the internuclear axis, and η is the electronic state.[1] The effective Hamiltonian for AlH^+ should account for the coupling between its many internal degrees of freedom which include: electronic orbit, nuclear rotation, electron spin and nuclear spin stemming from both aluminum and hydrogen:

$$\mathcal{H}_{\eta v} = T_\eta + G_{\eta v} + \mathcal{H}_{\rm rot} + \mathcal{H}_{\rm cd} + \mathcal{H}_{\rm so} + \mathcal{H}_{\rm ss} + \mathcal{H}_{\rm sr} + \mathcal{H}_{\Lambda \rm d} + \mathcal{H}_{\rm Q} + \mathcal{H}_{\rm nsr} + \mathcal{H}_{\rm nsns} + \mathcal{H}_{\rm hfs} \quad (4.10)$$

where T_η is the origin of $|\eta, \Lambda\rangle$ and $G_{\eta v}$ is the vibrational energy obtained by vibrationally averaging over the internuclear coordinate R.[2] The remaining terms are the rotational, centrifugal distortion, spin-orbit, electron spin-spin, spin-rotation, Λ-doubling, quadrupole, nuclear spin-rotation, nuclear spin-nuclear spin and hyperfine interactions.

The Hamiltonian (Eq. 4.10) can be simplified with some knowledge of the electronic state. We perform spectroscopy in the ground state, so $T_\eta = 0$. Although the AlH^+ ground state was determined to be a Σ state ($\Lambda = 0$) long ago [119], this could have been predicted with some qualitative arguments. The thermodynamically stable separated atoms would be Al^+ and H, since the ionization energy of Al is smaller than that of H.

[1] Following the notation of [7], η sometimes represents all other quantum numbers not involved in the effective Hamiltonian

[2] See Section 7.5 in [7]

The lowest energy electron configuration of Al^+ and H is ^1S and ^2S, respectively. Invoking the Wigner-Witmer rules, the addition of these two symmetries will produce a $^2\Sigma^+$ state (See Tables 26 and 27 of [6]). Alternatively, one could use molecular orbital theory to predict the ground state molecular orbital configuration to be a σ^1, which corresponds to only one possible electron configuration: $^2\Sigma^+$ (See Section A.5 of [120]).[1] A Σ ground state configuration means that $\mathcal{H}_{\rm so} = 0$ to first order due to a lack of conserved orbital angular momentum to which the electron spin can couple. In addition $\mathcal{H}_{\Lambda \rm d} = 0$, since this interaction only occurs for $\Lambda > 0$ states. Lastly, a single unpaired electron (spin doublet) has no electron spin coupling partner, yielding $\mathcal{H}_{\rm ss} = 0$.

The remaining terms in the effective Hamiltonian for AlH^+ can be written more explicitly to represent the involved angular momenta. The rotational kinetic energy is:

$$\mathcal{H}_{\rm rot} = B_{\eta v} \boldsymbol{N}^2 \tag{4.11}$$

where $\boldsymbol{N}$ is the total angular momentum absent of spin ($\boldsymbol{N} = \boldsymbol{J} - \boldsymbol{S}$), and $B_{\eta v} = \langle \eta v | B(R) | \eta v \rangle$, our vibronic state's expectation value of the rotational constant:

$$B(R) = \frac{\hbar^2}{2 M_r R^2} \tag{4.12}$$

where M_r is the reduced mass of the nuclei. Note that Eq. 4.11 is often seen in the literature with the rotational angular momentum $\boldsymbol{R}$. However, the rotation operator mixes different electronic states in the exact Hamiltonian. In our effective Hamiltonian, $\boldsymbol{R} = \boldsymbol{N} - \boldsymbol{L}$, where $\boldsymbol{L}$ is the orbital angular momentum, which allows us to add in the effects of electronic state mixing perturbatively. Within the effective Hamiltonian, the

[1] For a more complicated scenario where multiple electron configurations are possible, see Chapter 5

first-order diagonal element of the rotational energy is $B_{\eta v}(\boldsymbol{N}^2 - \boldsymbol{L}_{\boldsymbol{z}}^2)$. This simplifies to Eq. 4.11 for a Σ state ($L_z = \Lambda = 0$).[1] Note for the following terms in the Hamiltonian, the ηv subscripts are dropped, although they too are meant to represent the interaction constants with a specific vibronic state.

Continuing with Eq. 4.10, the centrifugal distortion term is

$$\mathcal{H}_{\text{cd}} = -D(\boldsymbol{N}^2)^2 \tag{4.13}$$

where D is the centrifugal distortion constant, which accounts for the rotating nuclei being pulled apart as they rotate. The spin-rotation term is:

$$\mathcal{H}_{\text{sr}} = -\gamma T^1(\boldsymbol{N}) \cdot T^1(\boldsymbol{S}) \tag{4.14}$$

where γ is the spin-rotation constant, describing the strength of the electron spin's interaction with the nuclear rotation to first order. To second order, γ includes the interaction of excited electronic states, the effect of which is typically much larger than the first order contribution.[2] The angular momenta $\boldsymbol{N}$ and $\boldsymbol{S}$ are represented in spherical tensor form (T^k), indicating they are rank 1, vector operators. The spherical tensor framework is invaluable for deriving analytical expressions for matrix elements involving the coupling of several angular momenta. A great resource understanding the properties of spherical tensors is [121] and Chapter 5 of [7].

The quadrupole interaction stems from the individual nuclei's quadrupole moments interacting with the local electric field gradient at each respective nucleus. For AlH^+,

[1] More information can be found in Sections 7.4.2 and 7.5.3 of [7]
[2] See Section 7.4.4 of [7].

only Al has a nonzero quadrupole moment, and its interaction takes the form:

$$\mathcal{H}_{\mathrm{Q}} = eQq_0T^2(\boldsymbol{\nabla E}) \cdot T^2(\boldsymbol{Q}) \tag{4.15}$$

where e is the electron charge, Q is the quadrupole moment of the aluminum nucleus, and q_0 corresponds to the average field gradient for a given electronic state:

$$q_0 = -2\langle \eta, \Lambda | T_0^2(\boldsymbol{\nabla E}) | \eta, \Lambda \rangle \tag{4.16}$$

Note that the quadrupole interaction is governed by the action of rank 2 tensors. The consequence of this is a lack of quadrupole shifts for states with total angular momentum less than 1.

Both Al and H possess nuclear spin, which can individually interact with the magnetic moment caused by rotation of the nuclei:

$$\mathcal{H}_{\mathrm{nsr}} = c_I^{\mathrm{Al}}T^1(\boldsymbol{I_{Al}}) \cdot T^1(\boldsymbol{N}) + c_I^{\mathrm{H}}T^1(\boldsymbol{I_H}) \cdot T^1(\boldsymbol{N}) \tag{4.17}$$

where c_I corresponds to the strength of the nuclear spin-rotation interaction. Similarly, the nuclear spins can interact with each other via:

$$\mathcal{H}_{\mathrm{nsns}} = c_4T^1(\boldsymbol{I_{Al}}) \cdot T^1(\boldsymbol{I_H}) \tag{4.18}$$

where c_4 is the isotropic nuclear spin-nuclear spin interaction strength.

The last component of the effective Hamiltonian, the hyperfine structure, describes interactions coupling nuclear spin to the electron spin. The effective Hamiltonian describing

these interactions is given by:

$$\begin{aligned}\mathcal{H}_{\text{hfs}} = b_F^{\text{Al}} T^1(\boldsymbol{I_{Al}}) \cdot T^1(\boldsymbol{S}) + b_F^{\text{H}} T^1(\boldsymbol{I_H}) \cdot T^1(\boldsymbol{S}) \\ + 3[t_0^{\text{Al}} T^1_{q=0}(\boldsymbol{I_{Al}}) \cdot T^1(\boldsymbol{S}) + t_0^{\text{H}} T^1_{q=0}(\boldsymbol{I_H}) \cdot T^1(\boldsymbol{S})],\end{aligned} \tag{4.19}$$

which consists of two separate interactions for each nucleus. The Fermi contact interaction (b_F) describes the isotropic interaction between the nuclear and electronic spin at the nucleus. The other interaction involves a classical dipolar interaction between the electronic and nuclear spins. Note that in contrast to how the dipolar interaction is represented in Eq. 4.19, its most general form is a rank 2 tensor interaction (See Appendix 8.1 and 8.2 of [7]), consisting of many components. However the strongest component is usually the diagonal element in Λ, whose strength is determined by t_0.

Fortunately the internal structure of AlH^+ has been characterized by many investigators over the last several decades (Table 4.2). The quadrupole interaction constant has not been measured, although in neutral AlH it was measured to be -36.72 MHz [122]. While the field gradient will likely be different for AlH^+, the AlH measurement provides an insightful order of magnitude. Although some of the smaller interaction constants have yet to be measured, the present values greatly decrease the parameter space when fitting a more precise spectrum.

4.5.2. Choosing a Basis Set

To fit our experimental spectrum, we have to compute our own eigenspectrum for comparison. This requires inputting estimated molecular constants into our effective Hamiltonian

Interaction	Constant	Value	Reference
Rotation	B	1.97×10^5	[123]
Centrifugal Distortion	D	14	[123]
Spin-Rotation	γ	1700	[123]
Hyperfine Fermi Contact (Al)	b_F^{Al}	1586	[124]
Hyperfine Fermi Contact (H)	b_F^{H}	49	[124]
Hyperfine Dipolar (Al)	t_0^{Al}	442	[124]
Hyperfine Dipolar (H)	t_0^{H}	2	[124]

Table 4.2. Molecular constants for the ground vibronic state of AlH^+ in MHz.

and diagonalizing a matrix constructed with our choice of basis set. Because the eigenstates of the Hamiltonian can be expanded in any basis set, any choice of basis set will allow us to fit a spectrum and determine the molecular constants. However, choosing an arbitrary basis set might not lead to any physical intuition.

In general, it is both most convenient and insightful to choose a basis set with the largest number of good quantum numbers, which correspond to conserved quantities in the Hamiltonian. One method to visualize constants of motion is to draw vector coupling diagrams for all the angular momentum for each degree of freedom in the molecule. A series of idealized coupling cases, named Hund's cases [6], well-approximate most diatomic spectra. For example, in Hund's case (a) the orbital angular momentum ($\boldsymbol{L}$) is fixed to the internuclear axis. Note that the electron spin ($\boldsymbol{S}$) is also fixed to the same axis due to the electron orbit creating magnetic moment to which the spin can couple [125]. The cylindrically symmetric potential about the internuclear axis leads to the projection of both the electron orbital and spin angular momentum on the internuclear axis ($\boldsymbol{L_z}$ and $\boldsymbol{S_z}$) being conserved, corresponding to the conserved quantities Λ and Σ. In contrast, Hund's case (c) represents a scenario where spin-orbit coupling is so strong that $\boldsymbol{L}$ and

$\boldsymbol{S}$ couple together to form $\boldsymbol{J_a}$. In this case neither projection onto the internuclear axis is individually conserved in time, although the projection of $\boldsymbol{J_a}$ (Ω) is conserved. The diagonal matrix elements for the different Hund's cases will produce different patterns in the spectrum. By matching the measured spectrum to these idealized cases, we can build physical intuition as to the internal molecular processes. In many cases, molecular spectra can corresponds to some mixture of different Hund's cases which occur due to off-diagonal matrix elements coupling states of different Ω.[1] For low J states these off-diagonal couplings are small, and the spectra correspond well to certain Hund's cases.

AlH^+ has a Σ ground state, which almost always corresponds to Hund's case (b) for low $\boldsymbol{N}$ states.[2] The lack of conserved orbital angular momentum along the internuclear axis means no spin-orbit coupling fixes $\boldsymbol{S}$ to the internuclear axis, instead coupling directly to $\boldsymbol{N}$. The validity of any coupling scheme can be tested against the criteria for nondegenerate perturbation theory [126]:

$$\left| \frac{H_{ij}^{(1)}}{E_i^{(0)} - E_j^{(0)}} \right| < 1 \tag{4.20}$$

where $H_{ij}^{(1)}$ is the first order perturbation and $E_{i/j}^{(0)}$ are the zeroth order eigenenergies. Using Eq. 4.20, this means that the $T^1(\boldsymbol{N}) \cdot T^1(\boldsymbol{S})$ interaction should be smaller than the rotational spacing, i.e. $\gamma/B < 1$. We however have to create a coupling scheme that will additionally take into account the two nuclear spins, and we can use the same principle to construct the appropriate basis set. Based on the interaction constants in Table 4.2,

[1] See $\boldsymbol{L}$- and $\boldsymbol{S}$-uncoupling operators in Section 3.1.2.3 in [126]

[2] Note that Hund's case (b) can be shown to be equivalent to Hund's case (a) in the limit of spin-orbit coupling going to zero [127].

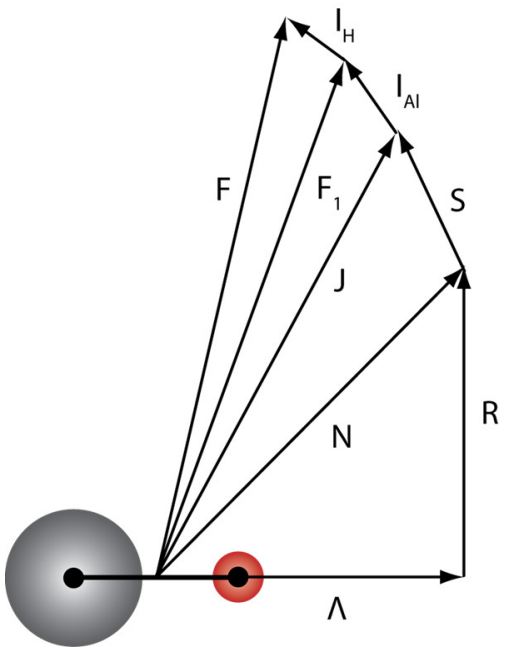

Figure 4.12. Vector coupling diagram for AlH^+.

we can construct a coupling scheme:

$$\begin{aligned} \boldsymbol{N} + \boldsymbol{S} &= \boldsymbol{J} \\ \boldsymbol{J} + \boldsymbol{I_{Al}} &= \boldsymbol{F_1} \\ \boldsymbol{F_1} + \boldsymbol{I_H} &= \boldsymbol{F} \end{aligned} \tag{4.21}$$

which corresponds to the vector coupling diagram in Fig. 4.12. Based on the similar magnitudes of γ and b_F^{Al}, it is clear that $\boldsymbol{F_1}$ will not be diagonal in this basis set, meaning the matrix constructed in this basis set will have to be diagonalized to obtain the true eigenspectrum, corresponding to a linear combination of basis states.

4.5.3. Evaluating matrix elements

Having chosen an appropriate basis set, the next step is to evaluate individual matrix elements for each nonzero interaction in Eq. 4.10. Analytical expressions for these matrix elements can be derived using spherical tensor algebra. Although the final expressions look daunting, they only need to be derived once for each coupling scheme. The authors of [7] have in fact derived the matrix elements for almost all common coupling cases for diatomic molecules, reducing our task to simply looking them up! However, for previously underived coupling schemes, we can make use of derived angular momentum relations summarized in Appendix 5.1 of [7]. For example, the spin rotation matrix element is:

$$\begin{aligned}
&\langle \eta, \Lambda; N, S, J, F_1, F, M_F | \gamma T^1(\boldsymbol{N}) \cdot T^1(\boldsymbol{S}) | \eta, \Lambda; N, S, J, F_1, F, M_F \rangle \\
&\quad = \gamma (-1)^{N+J+S} \begin{Bmatrix} S & N & J \\ N & S & 1 \end{Bmatrix} \langle N || T^1(\boldsymbol{N}) || N \rangle \langle S || T^1(\boldsymbol{S}) || S \rangle \\
&\quad = \gamma (-1)^{N+J+S} \begin{Bmatrix} S & N & J \\ N & S & 1 \end{Bmatrix} \{ N(N+1)(2N+1) S(S+1) 2S+1 \}^{1/2}
\end{aligned} \tag{4.22}$$

where the quantities the large brackets are a Wigner 6-j symbol and we have used the fact that our basis is diagonal in N ($N = N'$). Note also that the larger quantum numbers F_1 and F, corresponding to the $\boldsymbol{F_1}$ and $\boldsymbol{F}$ vectors, are ignored because both $\boldsymbol{F_1}$ and $\boldsymbol{F}$ are composed of $\boldsymbol{J} = \boldsymbol{N} + \boldsymbol{S}$. Although we could have looked up Eq. 4.22 in a book,[1] the result of Eq. 4.22 was derived using two relationships stemming from spherical tensor

[1] Eq. 9.89 in [7]

algebra:

$$\begin{aligned}&\langle j_1,j_2,j_{12},m|T^k(\boldsymbol{A_1})\cdot T^k(\boldsymbol{A_2})|j_1',j_2',j_{12}',m'\rangle\\&=(-1)^{j_1'+j_{12}+j_2}\delta_{j_{12},j_{12}'}\delta_{m,m'}\begin{Bmatrix}j_2' & j_1' & j_{12}\\ j_1 & j_2 & k\end{Bmatrix}\langle j_1||T^k(\boldsymbol{A_1})||j_1'\rangle\langle j_2||T^k(\boldsymbol{A_2})||j_2'\rangle\end{aligned}\tag{4.23}$$

and

$$\langle j||T^1(\boldsymbol{j})||j'\rangle=\delta_{j,j'}[j(j+1)(2j+1)]^{1/2},\tag{4.24}$$

both of which can be found in Appendix 5.1 of [7]. The matrix elements for the hyperfine and quadrupole interactions in Eq. 4.19 and Eq. 4.15 consume much more space, so we refer the reader to Section 10.4.4 of [7], where the matrix elements were derived for the same coupling scheme used here. Once the matrix elements have been computed, diagonalizing the matrix should yield a predicted level structure. For the $\boldsymbol{N}=1$ manifold in the ground vibronic state, the predicted energy level diagram is drawn in Fig. 4.13. These were computed using the constants in Table 4.2.

4.5.4. Interactions with External Fields

Very often we subject the molecules to external electric and magnetic fields. For example, our AlH^+ sits in an ion trap, which can typically subject the ion to hundreds of Volts per meter electric fields and few-Gauss magnetic fields. High precision spectroscopy will resolve the Stark and Zeeman splittings between M_F states, making it helpful to evaluate these elements. The matrix elements will also define the selection rules and determine the transition line strengths, which helps identify transitions more easily.

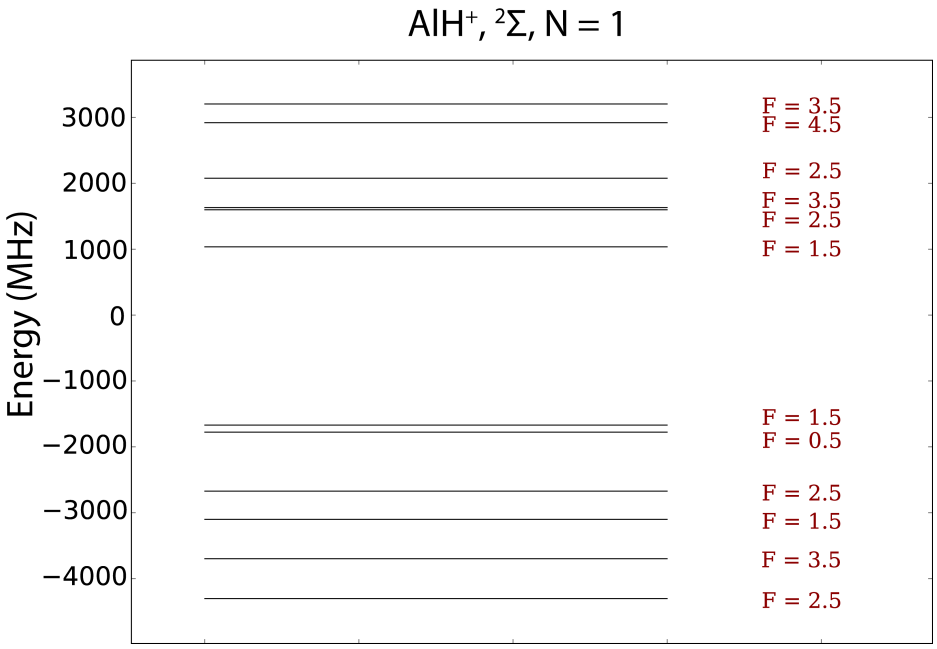

Figure 4.13. Energy levels for the $N = 1$ manifold in the vibronic ground state of AlH^+.

Matrix evaluation must be done with special care, however. Our external fields and our measurements are carried out in the laboratory-fixed frame, while most of the angular momenta we examine are defined with respect to the the internuclear axis, the body-fixed frame. For example, the Stark interaction is:

$$\mathcal{H}_{\mathrm{E}} = -T^1_{p=0}(\boldsymbol{\mu_e}) \cdot T^1_{p=0}(\boldsymbol{E_0}), \tag{4.25}$$

where $\boldsymbol{\mu_e}$ is the electric dipole moment and $\boldsymbol{E_0}$ is the electric field in the laboratory-fixed frame (p). The dipole moment, however is computed with respect to wavefunctions quantized in the body-fixed frame (q).[1] Spherical tensor algebra provides a robust way to evaluate matrix elements by rotating the laboratory-fixed components of $\boldsymbol{\mu_e}$ into the

[1] $p = q = 0$ means along the laboratory Z and internuclear axis, respectively.

body-fixed frame, using a relation stemming from the definition of a spherical tensor:

$$T_p^k(\boldsymbol{A}) = \sum_q \mathscr{D}_{pq}^{(k)}(\omega)^* T_q^k(\boldsymbol{A}) \tag{4.26}$$

where $\mathscr{D}_{pq}^{(k)}(\omega)^*$ is the complex conjugate of the pq element of the kth rank rotation matrix $\mathscr{D}_{pq}^{(k)}(\omega)$, which represents a rotation from the laboratory-fixed axis to the body-fixed axis through the three Euler angles $\omega = (\phi, \theta, \chi)$. We can exploit a useful relation to evaluate matrix elements with the rotation operator acting on a symmetric top wavefunction:[1]

$$\langle J, \Omega, M || \mathscr{D}_{.q}^{(k)}(\omega)^* || J', \Omega', M' \rangle = (-1)^{J-\Omega} [(2J+1)(2J'+1)]^{1/2} \begin{pmatrix} J & k & J' \\ \Omega & q & \Omega' \end{pmatrix}. \tag{4.27}$$

The first subscript of the rotation matrix element in Eq. 4.27 (.) means that the matrix element is reduced with respect to the orientation in the laboratory-fixed frame.

One more complication is that in order to use Eq. 4.27, we need to obtain the reduced matrix element, which we must extract out of our coupled basis set. For this we need two more useful relations:

$$\langle j, m | T_p^k(\boldsymbol{A}) | j', m' \rangle = (-1)^{j-m} \begin{pmatrix} j & k & j' \\ -m & p & m \end{pmatrix} \langle j || T^k(\boldsymbol{A}) || j' \rangle, \tag{4.28}$$

which is known as the Wigner-Eckart theorem, and

$$\begin{aligned} &\langle j_1, j_2, j_{12}, m | T^k(\boldsymbol{A_1}) | j_1', j_2', j_{12}', m' \rangle \\ &= \delta_{j_2, j_2'} (-1)^{j_{12}' + j_1 + k + j_2} [(2j_{12}+1)(2k+1)]^{1/2} \begin{Bmatrix} j_1' & j_{12}' & j_2 \\ j_{12} & j_1 & k \end{Bmatrix} \langle j_1 || T^k(\boldsymbol{A_1}) || j_1' \rangle \end{aligned} \tag{4.29}$$

[1] See Section 5.5.5 in [7].

where $T^k(\boldsymbol{A_1})$ only acts on $\boldsymbol{j_1}$ in the coupled system $\boldsymbol{j_1} + \boldsymbol{j_2} = \boldsymbol{j_{12}}$. Armed with Equations 4.26, 4.27, 4.24, 4.28 and 4.29, we can derive the Stark matrix elements in our coupled system. For the first step:

$$\begin{aligned}
&\langle \eta, \Lambda; N, \Lambda, S, J, I_{Al}, F_1, I_H, F, M_F| - T_0^1(\boldsymbol{\mu_e}) \cdot T_0^1(\boldsymbol{E_0})|\eta, \Lambda'; N', \Lambda', S, J', I_{Al}, F_1', I_H, F', M_F'\rangle \\
&\quad = E_0(-1)^{F-M_F} \begin{pmatrix} F & 1 & F' \\ -M_F & 0 & M_F \end{pmatrix} \\
&\qquad \times \langle \eta, \Lambda; N, \Lambda, S, J, I_{Al}, F_1, I_H, F|| - T_0^1(\boldsymbol{\mu_e})||\eta, \Lambda'; N', \Lambda', S, J', I_{Al}, F_1', I_H, F'\rangle
\end{aligned} \tag{4.30}$$

where we have replaced $T_0^1(\boldsymbol{E_0})$ with its scalar magnitude in the $p = 0$ direction: E_0. We also used the Wigner-Eckart theorem (Eq. 4.28) to remove the orientation dependence (M_F) in the reduced matrix element. Note that having our field in the $p = 0$ forces our matrix elements to be diagonal in M_F, as governed by the Wigner 3j symbol. We then further reduce the matrix element on the right hand side of Eq. 4.30 by repeatedly

applying Eq. 4.29 three times to unpack F, F_1 and J:

$$\begin{aligned} R.H.S. = -E_0(-1)^{F-M_F} &\begin{pmatrix} F & 1 & F' \\ -M_F & 0 & M_F \end{pmatrix} (-1)^{F'+F_1+1+I_H}\{(2F'+1)(2F+1)\}^{1/2} \\ &\times \begin{Bmatrix} F & F_1 & I_H \\ F_1' & F' & 1 \end{Bmatrix} (-1)^{F_1'+J+1+I_{Al}}\{(2F_1'+1)(2F_1+1)\}^{1/2} \\ &\times \begin{Bmatrix} F_1 & J & I_{Al} \\ J' & F_1' & 1 \end{Bmatrix} (-1)^{J'+N+1+S}\{(2J'+1)(2J+1)\}^{1/2} \begin{Bmatrix} J & N & S \\ N' & J' & 1 \end{Bmatrix} \\ &\times \langle \eta, \Lambda; N, \Lambda || T_0^1(\boldsymbol{\mu_e}) || \eta, \Lambda'; N', \Lambda' \rangle. \end{aligned} \tag{4.31}$$

The final step is to evaluate the reduced dipole moment matrix element in the body-fixed frame. Invoking Equations 4.26 and 4.27, the matrix element comes out to:

$$\begin{aligned} \langle \eta, \Lambda; N, \Lambda || T_0^1(\boldsymbol{\mu_e}) || \eta, \Lambda'; N', \Lambda' \rangle &= \sum_q \langle \eta, \Lambda; N, \Lambda || \mathscr{D}_{.q}^{(k)}(\omega)^* T_q^1(\boldsymbol{\mu_e}) || \eta, \Lambda'; N', \Lambda' \rangle \\ &= \mu_q (-1)^{J-\Lambda}\{(2N+1)(2N'+1)\}^{1/2} \begin{pmatrix} N & 1 & N' \\ \Lambda & q & \Lambda' \end{pmatrix}, \end{aligned} \tag{4.32}$$

where the μ_q is the scalar magnitude of the dipole moment in the q direction. The Wigner 3j symbol determines the selection rules. For example, if we are interested in transitions within the same electronic state, we would choose the $q = 0$ component, forcing $\Lambda = \Lambda'$ and replace μ_q with the permanent dipole moment μ_0. Combining Equations 4.30, 4.31 and 4.32 gives the full Stark matrix element for our coupled basis.

The transition probability for an electric dipole transition is proportional to the square of the Stark matrix element.[1] The square of Wigner 3j symbol in Eq. 4.32 is known historically as the Hönl-London factor, which effectively scales the dipole moment, governing the strength of a given transition.[2]

[1]See Section 6.1.2.1 of [126].
[2]For a more detailed discussion about line strengths, see [128].

CHAPTER 5

Polar Molecular Ion Optical Probe for Varying μ

One of the most attractive features of AlH^+ is its ability to be cooled quickly using optical methods [117, 72], which stems from its unusually small vibrational branching ratios on a broad-linewidth electronic transition [42]. Although this property can lead to a several orders of magnitude decrease in experimental dead time compared to other molecules, the experimental duty cycle is only one of many criteria that make a molecule suitable for a μ-variation measurement. In the process of identifying these criteria, we discovered the tellurium monohydride cation (TeH^+), which not only exhibits small vibrational branching ratios, but also meets many of the criteria necessary to set tighter constraints on the variation of μ. In the following sections we present the unique properties of TeH^+ and motivate its use as a probe of μ-variation. This work is being assembled into a manuscript for publication. Note that some of the calculations may have changed since publishing this thesis. The most recent and accurate work can be found in [129].

5.1. Electronic Structure of TeH^+

A spectrum of TeH^+ has never been measured, however its internal structure has been calculated and analyzed in [11]. The potential energy curves for the low lying states of TeH^+ in Fig. 5.1 exhibit a striking feature: the four lowest-energy potential wells have almost identical curvature and equilibrium distances. This structure can be predicted from a simple molecular orbital diagram, shown in Fig. 5.2. The π orbitals are almost

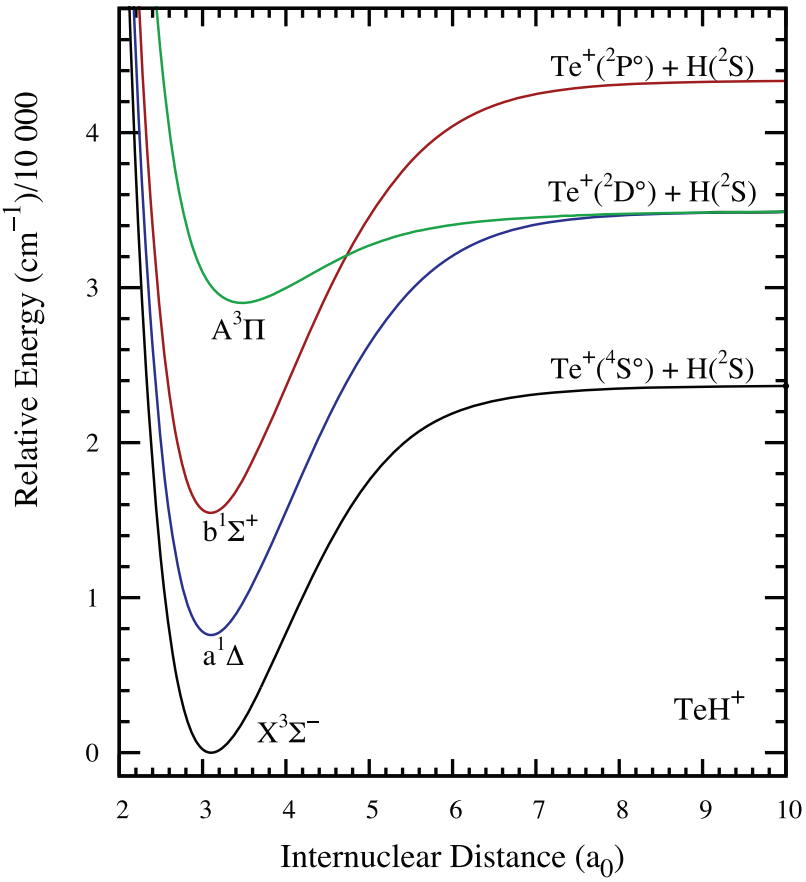

Figure 5.1. Potential energy curves for the lowest lying states of TeH^+, adapted from [11].

purely nonbonding, because the nearest orbitals of similar symmetry in hydrogen are approximately 12 eV higher in energy than the hydrogen 1s orbital. The first two excited state configurations in TeH^+ are simple rearrangements of electrons in the non-bonding orbitals, where relative energies of each state are governed by Hund's rules.

One can also predict that these configurations correspond to rearranging electrons in p orbitals highly localized on the Te atom. This can be seen by comparing the transition energies between configurations at the dissociation limit to the transition energies at

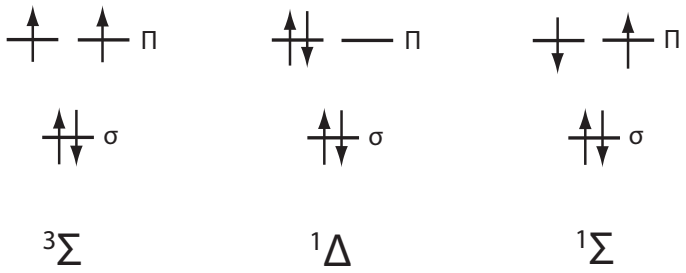

Figure 5.2. Molecular orbital diagrams for lowest lying states of TeH^+.

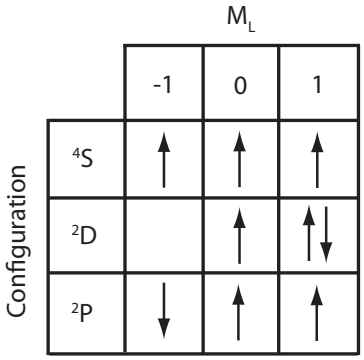

Figure 5.3. Lowest energy configurations of Te^+.

the equilibrium bond distance. At the dissociation limit, the energy splittings are governed by the electron configurations of Te^+: ^4S, ^2D and ^2P, depicted in Fig. 5.3. These configurations correspond to rearrangement of electrons between different p orbitals. At the equilibrium bond distance, the transition energies between electron configurations are very similar to those at the dissociation limit.

Because neither of the first two excited configurations involve removing an electron from a bonding orbital, the potential energy surfaces have almost identical well depth and equilibrium bond distances. Transitions between these electronic states are expected to have extremely diagonal nuclear wavefunction overlap, i.e. diagonal Franck-Condon factors (FCFs).[1] Despite the exceptionally small vibrational branching ratios expected

[1]A Franck-Condon factor of 1.000 was calculated for the b-X transition in [11].

for such transitions, this feature comes at the expense of these transitions being forbidden by spin selection rules. Forbidden transitions have narrow linewidths, hindering the speed of optical pumping.

Fortunately, the large mass of Te^+ leads to a massive spin-orbit coupling between the electronic states. Fig. 5.4 shows the potential energy curves when spin-orbit coupling is included in the Hamiltonian. When the spin-orbit interaction becomes larger than the rotational interaction, the Λ+S state splits into S+1 spin-orbit states, warranting a change of basis labeled by the good quantum number Ω.[1] The spin-orbit interaction couples states with the same Ω.[2] Here the $\Omega = 0$ component of the $X^3\Sigma^-$ state interacts with the $b^1\Sigma^+$ to produce a large X state splitting of more than 1000 cm^{-1}. Using LEVEL 16 [131], we calculate that the lifetimes of the $b0^+$ and a2 states are 15 μs and 2.4 ms, respectively.[3] The predicted vibrational and rotational constants of the $X_1 0^+$ state, are 2146.6 and 6.23 cm^{-1}, respectively. These large constants ensure that given a Boltzmann distribution at room temperature, nearly all of the population is in the vibrational ground state and fewer than 13 rotational states are occupied [72]. Given the highly diagonal FCFs, one can reasonably approximate only tens of scattering events necessary to cool the population from room temperature to the rovibrational ground state, which can be achieved relatively quickly using either the $b0^+$ or a2 states. An additional advantage of the X-a transition is that its energy lies within the O-band telecom communication region, for which the laser and amplification technology is well-developed.

[1] See page 344 of [130]
[2] See Section 7.4.4 of [7].
[3] The potential energy curves and transition dipole moment functions were obtained via personal communication from the authors of [11]

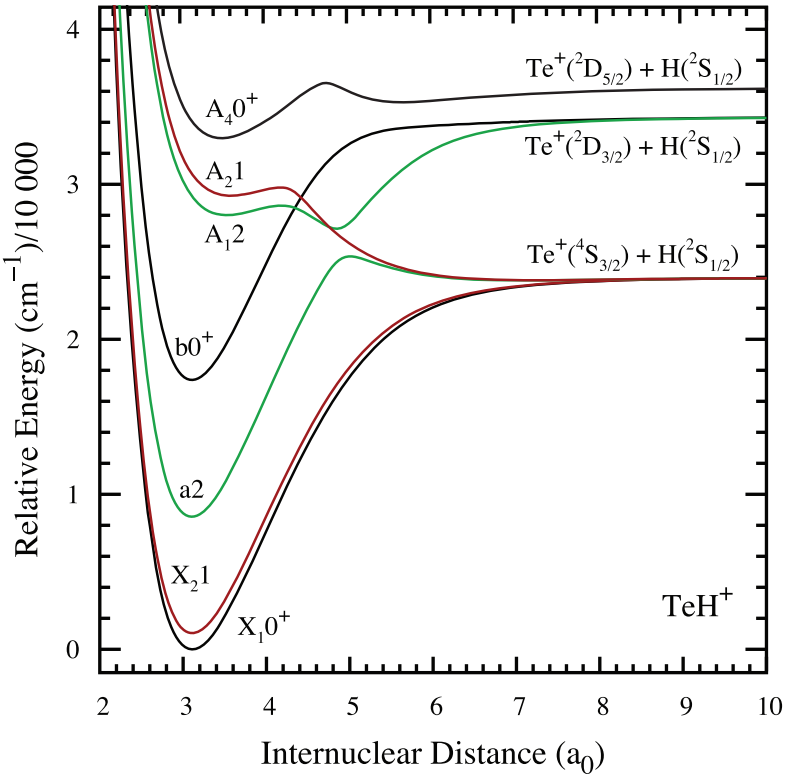

Figure 5.4. Potential energy curves for the lowest lying states of TeH^+, adapted from [11].

5.2. Sensitivity to μ

A fractional change in μ is assumed to be proportional to a fractional change in frequency ν via [36]:

$$\frac{\Delta\nu}{\nu} = K_\mu \frac{\Delta\mu}{\mu} \tag{5.1}$$

where $\nu = E_e - E_g$, the transition energy between the ground and excited states, and K_μ is the sensitivity coefficient derived to be:

$$K_\mu = \frac{\mu}{\nu}\left(\frac{dE_e}{d\mu} - \frac{dE_g}{d\mu}\right) \tag{5.2}$$

where the quantities $dE_e/d\mu$ and $dE_g/d\mu$ describe how the excited and ground states of the transition of interest change with μ. Their difference is called the absolute sensitivity ($K_\mu\nu$). Plugging Eq. 5.2 into Eq. 5.1, the equation can be rearranged into:

$$\Delta\mu = \Delta\nu \left(\frac{dE_e}{d\mu} - \frac{dE_g}{d\mu} \right)^{-1} \tag{5.3}$$

Eq. 5.3 suggests that the smallest limit on a change in μ can be achieved by finding a system with a large absolute sensitivity, where a high precision (small $\Delta\nu$) can be achieved. A convenient way to determine the absolute sensitivity is to fit the rovibrational energy levels to a Dunham expansion:[1]

$$E(v, J) = \sum_{k,l} Y_{k,l}(v + \frac{1}{2})^k [J(J+1) - \Omega^2]^l \tag{5.4}$$

where $Y_{k,l}$ refers to different rotational and vibrational constants of the molecule, v is the vibrational number, J is the total angular momentum number minus nuclear spin and Ω is the projection of the total angular momentum onto the internuclear axis. $E(v, J)$ changes with μ via [36]:

$$\frac{dE(v, J)}{d\mu} = \sum_{k,l} \frac{dY_{k,l}}{d\mu}(v + \frac{1}{2})^k [J(J+1) - \Omega]^l \tag{5.5}$$

and

$$\frac{dY_{k,l}}{d\mu} \approx \frac{-Y_{k,l}}{\mu} \left(l + \frac{k}{2} \right) \tag{5.6}$$

For most molecules, the vibrational energy spacings are much larger than the rotational energy spacing ($Y_{k,0} >> Y_{0,l}$), implying that vibrational transitions will have the largest

[1] See Section 2.9 of [7].

absolute sensitivity. In addition, the anharmonicity of the potential allows transitions between many vibrational states, leading to larger absolute sensitivities.[1] However, rotational transitions obey strict selection rules due to parity, preventing large absolute sensitivities.[2] Solving for the absolute sensitivity of the transition ν with only the first two vibrational constants $\omega_e/\omega_e x_e$ ($Y_{1,0}/Y_{2,0}$) yields:

$$K_\mu \nu = \frac{1}{2}(v_g - v_e)[\omega_e - 2(1 + v_g + v_e)\omega_e x_e] \tag{5.7}$$

where v_g and v_e are the ground and excited state vibrational numbers, respectively. Eq. 5.7 suggests that the largest absolute sensitivity can be achieved driving vibrational transitions in molecules with deep, harmonic potential wells, i.e. large $|(v_g - v_e)\omega_e|$ and small $\omega_e x_e$. Given a set of vibrational constants for a potential well and assuming the ground vibrational level $v_g = 0$, the optimal excited state v_e can be found by maximizing Eq. 5.7. The largest absolute sensitivity often occurs with $E(v_e)$ being approximately three quarters of the well depth [132]. For the ground $X_1 0^+$ state of TeH^+ the vibrational constants are 2146.6 and 37.70 for ω_e and $\omega_e x_e$, respectively. Using Eq. 5.7, the optimal transition is the $v = 0 \rightarrow v = 14$ transition, having an absolute sensitivity of $\sim$7100 cm^{-1}.

5.3. Statistics

Minimizing $\Delta\nu$ in Eq. 5.3 also leads to a tighter constraint on $\Delta\mu$. To maintain generality, we describe averaging many measurements of a single molecule with near-100% detection efficiency. Such reliable state detection exists in the form of electron

[1] Vibrational overtones are orders of magnitude weaker in line strength than transitions between adjacent vibrational states.

[2] Certain rotational transitions can however have very long lifetimes, compensating for their low absolute sensitvities.

shelving [133], implemented in techniques such as quantum logic spectroscopy [100]. A similar protocol is detailed in Chapter 4. For this analysis we choose to focus on Ramsey interferometry due to its success in atomic clock experiments reaching fractional precisions at one part in 10^{18} [134, 135].

In the quantum projection noise limit, the root-mean-square frequency uncertainty as a function of measurement time T is derived to be [136, 137]:

$$\delta f_{rms}(T) = \frac{1}{2T_R \pi C}\sqrt{\frac{T_c}{2T}} \tag{5.8}$$

where T_R is the Ramsey time, T_c is the cycle time, T is the total measurement time and C is the visibility. The longer the Ramsey time, the more population exits the excited state via spontaneous emission, leading to a lower visibility. The optimal Ramsey time resides close to the lifetime of the transition (Γ^{-1}), corresponding to $C \approx 0.6$.[1] This expression assumes the measurement is performed on resonance, which can be achieved via phase modulation of the probe laser [138]. Note that each cycle time consists of two measurements, one on each side of the Ramsey fringe. In the limit of zero experimental dead time ($T_c = 2T_R = 2/\Gamma$), $\Delta\nu$ becomes proportional to $\sqrt{\Gamma}$. Examination of Eq. 5.8 reveals that we want an excited vibrational with a long lifetime (large T_R) and a molecule that we can re-prepare in the initial state as fast as possible (small T_c). The vibrational lifetimes in the $X_1 0^+$ of TeH^+ were calculated using LEVEL 16, using the potential energy curve and permanent dipole moment from [11].

[1] $C \approx 1 - e^{-1}$

5.4. Figure of Merit

The conclusions of Sections 5.2 and 5.3 are unfortunately not compatible. Eq. 5.7 yields larger absolute sensitivities for higher energy vibrationally excited states, which tend to have shorter lifetimes and require more time to re-prepare the system into the ground state, contradicting Eq. 5.8. Plugging Eq. 5.8 into Eq. 5.3 with ($T_R = 1/\Gamma$), a figure of merit can be established with the leftover relevant parameters [139]:

$$\mathrm{FOM}_k = \frac{K_\mu \nu}{\Gamma^k} \tag{5.9}$$

where $k = 1/2$ in the limit of zero experimental dead time ($T_c = 2T_R$), and $k = 1$ in the limit of long experimental dead time ($T_c >> T_R$). Combining the vibrational lifetime data acquired using LEVEL 16 with the absolute sensitivity calculation for each level, we plot in Fig. 5.5 the figure of merit for each vibrationally excited state normalized to the first vibrational excited state in regimes of short and long cycle times. Note that while both regimes are displayed on the same plot, one cannot compare the values on the vertical axis to each other between the two regimes. Examining Fig. 5.5 reveals that the choice of excited state is more critical in the linewidth-limited experiment, starting with a steep slope that eventually plateaus. It also shows that the optimal compromise between excited state lifetime and absolute sensitivity is v = 8, which has a lifetime of 40 ms and the $v = 0 \rightarrow v = 8$ transition has an absolute sensitivity of $\sim$5900 cm^{-1}.

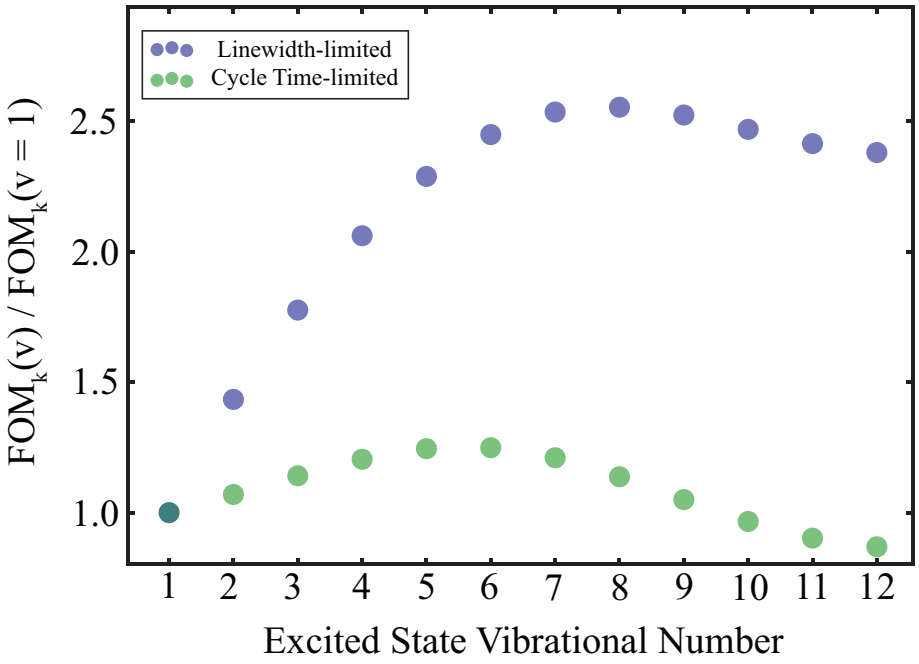

Figure 5.5. Figure of merit as a function of vibrationally excited state for cycle time-limited (k = 1) and linewidth-limited (k = 1/2) experiments, normalized to $v = 1$.

5.5. Systematics

Eq. 5.8 indicates that we can reach an arbitrary precision if we average long enough (large T). However, at some point $\Delta\nu$ will be limited by systematic frequency shifts.[1] Our ground and excited states will be sensitive to external fields, and unstable external fields will translate to uncertainty in $\Delta\nu$. Specifically, we are concerned about differential frequency shifts, which occur when the ground and excited states have different susceptibilities. The previous sections have narrowed our analysis down to the two vibrational states of interest: $v = 0$ and $v = 8$. Analysis of the differential shifts arising from different

[1] A constant systematic frequency offset would cancel out in a μ-variation measurement, although drifting systematics would not.

interactions will further narrow down the choice of specific rotational and hyperfine states to use within each vibrational manifold.

5.5.1. Basis Set

The general procedure for calculating systematic shifts is to construct an effective Hamiltonian with the appropriate interaction terms, and diagonalize the Hamiltonian to obtain the energy shifts at different external field strengths. To reliably estimate the energy shifts, we must choose a basis set that will accurately describe the system. As described in Section 5.1, the strong spin-orbit coupling interaction suggests that Hund's case (c) will be the most reliable angular momentum coupling scheme, where $\boldsymbol{L}$ and $\boldsymbol{S}$ first couple to form $\boldsymbol{J_a}$. The rotational angular momentum $\boldsymbol{R}$ and $\boldsymbol{J_a}$ couple to form $\boldsymbol{J}$. The good quantum numbers are J and its projection onto the internuclear axis Ω. J_a would usually not be a good quantum number due to spherical symmetry being broken by the internuclear axis.[1] However, here we also assume the pure precession approximation, where one approximates the molecular orbitals as atomic orbitals with well defined atomic quantum numbers, quantized along the internuclear axis.[2] Under this approximation, L and S, and therefore J_a are assumed to be good quantum numbers. This approximation works especially well for hydrides with large nuclei such as TeH^+ because the hydrogen 1s orbital does little to perturb the large and highly localized atomic orbitals on the other atom (Section 5.5 of [126]).

Using knowledge of the atomic configurations at the dissociation limits from Section 5.1, we can determine J_a for our states of interest. For the ground state at the

[1]The projection of $\boldsymbol{J_a}$ onto the internuclear axis is Ω, which is however a good quantum number.
[2]See Section 7.8.3 of [7].

dissociation limit, Te^+ and H are in the ^4S and ^2S configurations, respectively. Both atoms approach each other with no orbital angular momentum, so L = 0 for the ground states of TeH^+. Te^+ in its ground state has 3 unpaired electrons, one of which will be paired with the H electron, yielding S = 1 for TeH^+. Therefore $J_a = 1$ and its two possible projections onto the internuclear axis are $\Omega = 0$ and $\Omega = 1$: the $X_1 0^+$ and $X_2 1$ states.

For simplicity we consider the ^{130}Te isotope due to its lack of nuclear spin. Hydrogen has a nuclear spin of 1/2, and we must decide how this spin will couple in our system. Two sub-cases of Hund's case (c) arise known as Hund's case (c_α) and (c_β), which correspond to the nuclear spin $\boldsymbol{I_H}$ either coupling to $\boldsymbol{J_a}$ or $\boldsymbol{J}$. In TeH^+ the Hund's case (c_β) scheme is more appropriate due to the large rotational energy common to hydrides. $\boldsymbol{J_a}$, which is quantized along the internuclear axis, is averaged out due to the fast rotation of the internuclear axis, preventing $\boldsymbol{I_H}$ from coupling to $\boldsymbol{J_a}$ [140]. Quantitatively, the rotational energy is much larger than the coupling energy of $\boldsymbol{I_H} \cdot \boldsymbol{J_a}$. Our basis is then $|J_a, \Omega; \Omega, J, I_H, F, M_F\rangle$.

We also require that our eigenstates have proper symmetry, and the Hund's case (c) basis states are not eigenfunctions of the space-fixed inversion operator[1] We therefore introduce the parity quantum number ϵ, which can take values of 1 or -1. The correct parity states are then:

$$|J_a, \Omega; \Omega, J, I_H, F, M_F, \epsilon = 1\rangle = |J_a, \Omega; \Omega, J, I_H, F, M_F\rangle + (-1)^P |J_a, \Omega; \Omega, J, I_H, F, M_F\rangle$$

$$|J_a, \Omega; \Omega, J, I_H, F, M_F, \epsilon = -1\rangle = |J_a, \Omega; \Omega, J, I_H, F, M_F\rangle - (-1)^P |J_a, \Omega; \Omega, J, I_H, F, M_F\rangle \tag{5.10}$$

[1] $E^*|\Omega\rangle = |-\Omega\rangle \neq \pm|\Omega\rangle$.

where $P = J + s$, and s is even or odd depending on whether the parity of the electronic state is + or -.[1] $s = 0$ for the ground states of TeH^+.

5.5.2. Physical Picture

In the Hund's case (c) basis set, $\boldsymbol{J_a}$ and the rotational angular momentum $\boldsymbol{R}$ couple to form $\boldsymbol{J}$. The rotational Hamiltonian [142]:

$$\begin{aligned} \mathcal{H}_{\text{rot}} &= B(R)(\boldsymbol{J} - \boldsymbol{J_a})^2 \\ &= B(R)(\boldsymbol{J}^2 + \boldsymbol{J_a}^2 - 2\boldsymbol{J} \cdot \boldsymbol{J_a}), \end{aligned} \tag{5.11}$$

results in a $\boldsymbol{J} \cdot \boldsymbol{J_a}$ perturbation, which will mix states of different Ω.[2] Although the full effective Hamiltonian and its matrix elements for calculating this coupling are presented in Appendix C, we can use perturbation theory to show how the $\boldsymbol{J \cdot J_a}$ (rotational-electronic) interaction alters our eigenstates. In the absence of any inter-electronic coupling, the $X_2 1$ state is doubly-degenerate with the eigenstates given by Eq. 5.10. Assuming $X_2 1$ is dominantly perturbed by the $X_1 0^+$ state, the rotational-electronic interaction will couple one of the eigenstates with the rotational state in $X_1 0^+$ with the same J and parity. The energy splitting is given by:

$$\Delta T_{ef} = qJ(J+1), \tag{5.12}$$

where the Ω-doubling interaction strength q can be approximated as [143]:

$$q = \frac{2B^2 \langle X_2 1 | J_a^+ | X_1 0^+ \rangle}{\Delta E} \tag{5.13}$$

[1] See Table III of [141].
[2] For more information, see Section 10.7 (b) of [7].

where ΔE is the spin-orbit splitting, B is the rotational constant in $X_2 1$ and:

$$\langle X_2 1 | J_a^+ | X_1 0^+ \rangle = J_a (J_a + 1)^{0.5}. \tag{5.14}$$

If we assume that ΔT_{ef} is the second order energy correction to the rotational-electronic interaction, we can derive the first order correction to the wavefunction for $J_a = 1$:

$$\Psi^{(1)} = \frac{[2\sqrt{2}J(J+1)]^{1/2} B}{\Delta E} \tag{5.15}$$

Using $B = 6.23$ cm^{-1} and $\Delta E = 1049$ cm^{-1}, Eq. 5.15 suggests that the first rotationally excited state of $|\mathrm{X}_1 0^+, v = 0\rangle$ will be:

$$\Psi = |\mathrm{X}_1 0^+, v = 0, J = 1\rangle + 0.014 |\mathrm{X}_2 1, v = 0, J = 1, \epsilon = -1\rangle \tag{5.16}$$

Although the mixing is only on the order of a percent, this will lead to dramatic consequences, explained in Section 5.5.3.3.

5.5.3. Magnetic fields

5.5.3.1. Electronic. The strongest Zeeman interaction is attributed to a magnetic field interacting with nonzero spin and orbital magnetic moments:

$$\mathcal{H}_{Z_{el}} = -\mu_B T^1(\boldsymbol{B}) \cdot [g_s T^1(\boldsymbol{S}) + g_l T^1(\boldsymbol{L})] \tag{5.17}$$

where μ_B is a Bohr magneton (1.4 MHz/G) and g_s and g_l are the electron spin and orbital g factors having values of 2.0023 and 1, respectively. Even with impressive magnetic field control (1 μG), this corresponds to approximately a 1 Hz first order Zeeman shift, which

leads to a large fractional precision even for a large spectroscopy transition at 1 PHz ($\Delta\nu/\nu = 1 \times 10^{-15}$). Large first order Zeeman shifts have been handled either by driving forbidden "clock" transitions with zero first order Zeeman shift ($M_J = 0 \rightarrow M_J = 0$) [144], or by averaging over Zeeman states with opposite Zeeman shifts ($+M_J \rightarrow +M_J$ averaged with $-M_J \rightarrow -M_J$) [145]. Neither of these techniques however protect against second order Zeeman shifts, which arise from mixing with nearby Zeeman states from different manifolds.

One could almost entirely avoid such large Zeeman shifts by choosing electronic states with no spin or orbital angular momentum: $^1\Sigma$ and $\Omega = 0$ states, for example. Although even these states will partially mix with other electronic states having nonzero $\boldsymbol{S}$ or $\boldsymbol{L}$, which can still lead to relatively large Zeeman shifts.

5.5.3.2. Nuclear. The next strongest Zeeman interactions will arise from nuclear contributions:

$$\mathcal{H}_{\mathrm{Z}_{nuc}} = -T^1(\boldsymbol{B}) \cdot [g_N \mu_N T^1(\boldsymbol{I}) + g_r \mu_B T^1(\boldsymbol{N})] \tag{5.18}$$

where g_N is the nuclear g-factor, μ_N is the nuclear magneton and g_r is the rotational g-factor. The nuclear magneton is scaled by the proton-to-electron mass ratio, and therefore leads to the nuclear spin interaction being three orders of magnitude weaker than that of the electron. The rotational magnetic moment arises from the rotating nuclei creating a magnetic moment. The rotational g-factors also lead to an approximately three order of magnitude reduction in interaction strength. An extensive review of the rotational magnetic moment can be found in [146], and a general summary of similarly small Zeeman interactions can be found in Section 7.6 of [7].

Following our example in the previous section, the first order nuclear interactions can still limit precisions to approximately ($\Delta\nu/\nu = 1 \times 10^{-18}$). Previously mentioned averaging techniques however, can suppress the first order shift, leaving only the second order nuclear Zeeman shifts, which are effectively negligible.

5.5.3.3. Zeeman Shifts in TeH^+. Using the physical intuition presented in Section 5.5.2, we can estimate the most important contributors to the Zeeman shifts. If a percent of the $X_2 1$ state is mixed in with the $X_1 0^+$ state by the rotational-electronic interaction, it is clear that the electron spin Zeeman interaction will be the strongest interaction, because the electron spin Zeeman interaction is three orders of magnitude larger than the nuclear spin Zeeman interactions in the $X_1 0^+$ state. Similarly, the quadratic shifts will also be affected by the rotational-electronic interaction. The dominant quadratic Zeeman shifts arise from mixing with nearby hyperfine states, therefore the hyperfine splitting is critical to the determination of quadratic Zeeman shifts. Within the $X_1 0^+$ state, the proton nuclear spin-rotation interaction will lead to a small hyperfine splitting on the order of 10 kHz.[1] This would normally lead to a very large quadratic Zeeman shift; however, the contribution of the $X_2 1$ state suggests that the proton sees approximately a percent of an electron spin, leading to a larger hyperfine splitting via the $\boldsymbol{I} \cdot \boldsymbol{S}$ interaction.

5.5.4. Electric Fields

Molecules will respond to external electric fields via the Stark interaction:[2]

$$\mathcal{H}_{\mathrm{E}} = -T^1(\boldsymbol{\mu_e}) \cdot T^1(\boldsymbol{E}), \tag{5.19}$$

[1] See Appendix C

[2] This Stark shift derivation follows [147].

which can be expanded in terms of the laboratory-fixed components of the electric field:[1]

$$\mathcal{H}_{\mathrm{E}} = -\sum_{p}(-1)^{p}T^{1}_{-p}(\boldsymbol{\mu_e})T^{1}_{p}(\boldsymbol{E}). \tag{5.20}$$

where p sums over the electric field polarizations:

$$\begin{aligned} T^{1}_{0}(\boldsymbol{E}) &= E_z \\ T^{1}_{\pm 1}(\boldsymbol{E}) &= \mp\frac{1}{\sqrt{2}}(E_x \pm iE_y). \end{aligned} \tag{5.21}$$

The electric field has the form:

$$E_p = \frac{E(\boldsymbol{r})}{2}\left(e^{i\omega_e t} + e^{-i\omega_e t}\right) = E(\boldsymbol{r})cos(\omega_e t). \tag{5.22}$$

The corresponding Stark shift for single polarization p will be:

$$\Delta E = -\frac{1}{2}\alpha_{i,-p}(\omega_e)\langle\varepsilon_p^2\rangle \tag{5.23}$$

where $\langle\varepsilon_p^2\rangle$ is the time-averaged root-mean-square electric field amplitude,[2] and $\alpha_{i,-p}$ is the polarizability of an $|i\rangle$ state for p-polarized radiation with frequency ω_e:

$$\alpha_{i,-p}(\omega_e) = \sum_{f}\frac{|\langle i|T^{1}_{-p}(\boldsymbol{\mu_e})|f\rangle|^2}{\hbar}\left(\frac{2\omega_{if}}{\omega_{if}^2 - \omega_e^2}\right), \tag{5.24}$$

where $|f\rangle$ is coupling to $|i\rangle$ and ω_{if} is the energy difference between $|f\rangle$ and $|i\rangle$. We expand our dipole moment matrix element $\langle i|T^{1}_{-p}(\boldsymbol{\mu_e})|f\rangle$ in our Hund's case (c_β) basis

[1] Eq. 5.112 of [7] was used to expand the spherical scalar product.
[2] $E = \sqrt{2}\varepsilon$.

($|i\rangle = |\Omega, v, J, I_H, F, M_F, \epsilon\rangle$) and rotate into the body-fixed frame:

$$\begin{aligned}
\langle i|T^1_{-p}(\boldsymbol{\mu_e})|f\rangle &= \langle \Omega, v, J, I_H, F, M_F, \epsilon|T^1_{-p}(\boldsymbol{\mu_e})|\Omega', v', J', I_H, F', M'_F, \epsilon'\rangle \\
&= \sum_q \langle \Omega, v, J, I_H, F, M_F, \epsilon|\mathscr{D}^{(1)}_{-pq}(\omega)^* T^1_q(\boldsymbol{\mu_e})|\Omega', v', J', I_H, F', M'_F, \epsilon'\rangle \\
&= \sum_q (-1)^{F-M_F} \begin{pmatrix} F & 1 & F' \\ -M_F & -p & M'_F \end{pmatrix} (-1)^{F'+J+1+I_H} \\
&\times \{(2F'+1)(2F+1)\}^{1/2} \begin{Bmatrix} J' & F' & I_H \\ F & J & 1 \end{Bmatrix} (-1)^{J-\Omega} \\
&\times \begin{pmatrix} J & 1 & J' \\ -\Omega & q & \Omega' \end{pmatrix} \{(2J'+1)(2J+1)\}^{1/2} \sqrt{C^{HW}} \langle \eta, v|T^1_q(\boldsymbol{\mu_e})|\eta', v'\rangle,
\end{aligned} \tag{5.25}$$

where $\langle \Omega, v|T^1_q(\boldsymbol{\mu_e})|\Omega', v'\rangle$ is the vibronic body-fixed dipole moment in the q direction, and $C^{HW} = (1 + \delta_{\Omega 0} + \delta_{\Omega' 0} - 2\delta_{\Omega 0}\delta_{\Omega' 0})$ is the Hannson/Watsen factor that accounts for transitions between parity states [128]. Note that the second Wigner 3j symbol in Eq. 5.25 will ensure that only one component of q will be nonzero: $q = \Omega - \Omega'$. We therefore remove the sum over q and refer to the only surviving component of $T^1_q(\boldsymbol{\mu_e})$ as $\boldsymbol{\mu_e}$. We can therefore rewrite Eq. 5.24 in our basis:

$$\begin{aligned}
\alpha_{i,-p}(\omega_e) &= \frac{1}{\hbar} \sum_{\epsilon'} \sum_{\Omega'} \sum_{v'} \sum_{J'} \sum_{F'} (2J+1)(2J'+1)(2F+1)(2F'+1) \\
&\times \begin{pmatrix} F & 1 & F' \\ -M_F & -p & M_F + p \end{pmatrix}^2 \begin{Bmatrix} J' & F' & I_H \\ F & J & 1 \end{Bmatrix}^2 \begin{pmatrix} J & 1 & J' \\ -\Omega & \Omega - \Omega' & \Omega' \end{pmatrix}^2 \\
&\times C^{HW} |\langle \Omega, v|\boldsymbol{\mu_e}|\Omega', v'\rangle|^2 \left(\frac{2\omega_{if}}{\omega_{if}^2 - \omega_e^2} \right),
\end{aligned} \tag{5.26}$$

where we have removed the sum over M_F' by recognizing that the first Wigner 3j symbol can only be nonzero if $M_F' = M_F + p$. To obtain $\langle \Omega, v|\boldsymbol{\mu_e}|\Omega', v'\rangle$ we input the potential energy surfaces for Ω and Ω', as well as the electric dipole moment function between them into LEVEL 16, which computes the integral.

While Eq. 5.26 gives the full polarizability for a given state $|i\rangle$, it is often more useful to break up the total polarizability into its constituent scalar and tensor components such that the Stark shift:

$$\Delta E = -\frac{1}{2}[\alpha_F^s(\omega_e)T^0(\boldsymbol{\varepsilon}^2) + \alpha_F^T(\omega_e)T^2(\boldsymbol{\varepsilon}^2)], \tag{5.27}$$

Eq. 5.27 has the advantage of splitting up the direction-independent and dependent terms, where the direction-dependent tensor Stark shift goes to zero for the case of unpolarized radiation or averaging over transitions to all M_F' states. In the atomic literature [148, 149], Eq. 5.27 is written as:

$$\Delta E = -\frac{1}{2}\varepsilon^2 \left[\alpha_F^s(\omega_e) + \alpha_F^T(\omega_e)\frac{3M_F^2 - F(F+1)}{F(2F-1)}\right]. \tag{5.28}$$

which is valid when the electric field is assumed to be uniform along the Z direction. Eq. 5.28 defines $\alpha_F^T(\omega_e)$ such that:

$$\Delta E = -\frac{1}{2}\varepsilon^2 \left[\alpha_F^s(\omega_e) + \alpha_F^T(\omega_e)\right] \tag{5.29}$$

for stretched states.[1]

[1]One can see that the numerator $[3M_F^2 - F(F+1)]$ goes to zero when summing over $M_F = -F$ to F.

The extra degrees of freedom for a generic molecule prohibit the polarizability from being written in a form as simple and convenient as Eq. 5.28. However, for the special case of a molecule in a $^1\Sigma$ (or $\Omega = 0$) state and a linearly polarized electric field,[1] the polarizability actually can be written in a simple form [150, 151]:

$$\Delta E = -\frac{1}{2}\varepsilon^2 \left[\alpha^s(\omega_e) + \alpha^T(\omega_e)\frac{3M_J^2 - J(J+1)}{(2J-1)(2J+3)}\right], \tag{5.30}$$

when making appropriate approximations.[2] Knowing that $\alpha^T(\omega_e)$ goes to zero when summing over Zeeman states, we can actually derive an expression for $\alpha^s(\omega_e)$ starting from the full polarizability (Eq. 5.26).

For the case of unpolarized radiation, we can take advantage of the following sum rule to derive the scalar polarizability:

$$\sum_p \begin{pmatrix} F & 1 & F' \\ -M_F & -p & M_F + p, \end{pmatrix}^2 = \frac{1}{2F+1}. \tag{5.31}$$

Summing Eq. 5.26 over the laboratory-fixed polarization p and using Eq. 5.31 removes the dependence on p. We can also remove the dependence on the hyperfine structure by making use of some symmetry properties and sum rules for Wigner 6j symbols:

$$\begin{Bmatrix} J' & F' & I_H \\ F & J & 1 \end{Bmatrix} = \begin{Bmatrix} I_H & J' & F' \\ 1 & F & J \end{Bmatrix} \tag{5.32}$$

[1] Hyperfine structure is ignored here.

[2] Although Eq. 5.30 was derived for the electronic polarizability, It can be shown that the coefficient in the second term of Eq. 5.30 appears when calculating both the rotational and vibrational polarizabilities as well.

and

$$\sum_{F'}(2F'+1)\begin{Bmatrix} I_H & J' & F' \\ 1 & F & J \end{Bmatrix}\begin{Bmatrix} I_H & J' & F' \\ 1 & F & J \end{Bmatrix} = \frac{1}{2J+1}. \tag{5.33}$$

The scalar polarizability then becomes:

$$\begin{aligned}\alpha_i(\omega_e) = \frac{1}{\hbar}\sum_{\epsilon'}\sum_{\Omega'}\sum_{v'}\sum_{J'}(2J'+1)\begin{pmatrix} J & 1 & J' \\ -\Omega & \Omega-\Omega' & \Omega' \end{pmatrix}^2 \\ \times C^{HW}|\langle\Omega, v|\boldsymbol{\mu_e}|\Omega', v'\rangle|^2\left(\frac{2\omega_{if}}{\omega_{if}^2-\omega_e^2}\right).\end{aligned} \tag{5.34}$$

Note that we have effectively treated the different Zeeman and hyperfine states as degenerate when making use of the sum rules (Eq. 5.31 and Eq. 5.33), which is justified because their interaction strengths are many orders of magnitude smaller than the rotational splitting.

To obtain more physical insight about the Stark interaction in TeH^+, we split up Eq. 5.34 into its different degrees of freedom:

$$\alpha_r^s(\omega_e) = \frac{1}{\hbar}\sum_{J'}(2J'+1)\begin{pmatrix} J & 1 & J' \\ 0 & 0 & 0 \end{pmatrix}^2 |\langle \mathrm{X}_1 0^+, v|\boldsymbol{\mu_e}|\mathrm{X}_1 0^+, v\rangle|^2\left(\frac{2\omega_{if}}{\omega_{if}^2-\omega_e^2}\right), \tag{5.35}$$

$$\alpha_v^s(\omega_e) = \frac{1}{\hbar}\sum_{v'\neq v}\sum_{J'}(2J'+1)\begin{pmatrix} J & 1 & J' \\ 0 & 0 & 0 \end{pmatrix}^2 |\langle \mathrm{X}_1 0^+, v|\boldsymbol{\mu_e}|\mathrm{X}_1 0^+, v'\rangle|^2\left(\frac{2\omega_{if}}{\omega_{if}^2-\omega_e^2}\right), \tag{5.36}$$

$$\alpha_{SO}^s(\omega_e) = \frac{2}{\hbar}\sum_{v'}\sum_{J'}(2J'+1)\begin{pmatrix} J & 1 & J' \\ 0 & -1 & 1 \end{pmatrix}^2 |\langle \mathrm{X}_1 0^+, v|\boldsymbol{\mu_e}|\mathrm{X}_2 1, v'\rangle|^2\left(\frac{2\omega_{if}}{\omega_{if}^2-\omega_e^2}\right), \tag{5.37}$$

and

$$\alpha_e^s(\omega_e) = \frac{2}{\hbar}\sum_{v'}\sum_{J'}(2J'+1)\begin{pmatrix} J & 1 & J' \\ 0 & -1 & 1 \end{pmatrix}^2 |\langle \mathrm{X}_1 0^+, v|\boldsymbol{\mu_e}|\mathrm{A}_2 1, v'\rangle|^2 \left(\frac{2\omega_{if}}{\omega_{if}^2 - \omega_e^2}\right), \quad (5.38)$$

where α_r^s and α_v^s are the ground state rotational and vibrational contributions; α_{SO}^s is the nearby spin-orbit state contribution, and α_e^s is the electronic contribution, which we attribute to the $A_2 1$ state because it has the largest electronic dipole moment from $X_1 0^+$ [11]. We use LEVEL 16 to compute the dipole moments and energy splittings ω_{if} between each ro-vibrational state.

Note that the $A_2 1$ state has only 1 bound state with small Franck-Condon overlap. However, our spectroscopy states in $X_1 0^+$ will interact with the continuum states of $A_2 1$ as well, therefore Eq. 5.38 is actually a poor approximation. We instead invoke the Franck-Condon principle and assume that an electronic transition happens instantaneously relative to the nuclear motion, where the probability of a transition is given by the probability of the nuclear wavefunction at a given internuclear distance. The polarizability is then calculated via:

$$\alpha_e^s(\omega_e) = \frac{2}{\hbar}\int |\Psi^v_{\mathrm{X}_1 0^+}(R)|^2 \boldsymbol{\mu_e}(R)^2 \left(\frac{2V(R)}{V(R)^2 - \omega_e^2}\right) dR, \quad (5.39)$$

where R is the internuclear distance, $\Psi^v_{\mathrm{X}_1 0^+}(R)$ is the ground state wavefunction, $\boldsymbol{\mu_e}(R)$ is the dipole moment between $X_1 0^+$ and $A_2 1$, and $V(R)$ is the energy difference E($A_2 1$(R)) - E($|X_1 0^+, v\rangle$).

	$\alpha^X(\omega=0)$ (a.u.)				$\alpha^X(\omega=0)$ (a.u.)			
	α_S^r	α_S^v	α_S^{so}	α_S^e	α_T^r	α_T^v	α_T^{so}	α_T^e
$\|0,0\rangle$	1500	0.02	0.04	1	0	0	0	0
$\|0,1\rangle^*$	0.08	0.02	0.04	1	1100	-0.04	0.02	0.6
$\|0,2\rangle$	0.2	0.02	0.04	1	400	-0.04	0.02	0.6
$\|8,2\rangle^*$	0.3	-0.03	0.03	0.6	600	-0.09	0.01	0.3

Table 5.1. Contributions to DC polarizabilities for selected $X_1 0^+$ J-states $|v,J\rangle$. The proposed spectroscopy transition is marked*.

Having an expression for the scalar polarizability for each degree of freedom, we can use it to calculate $\alpha^T(\omega_e)$ for each degree of freedom using Eq. 5.30.[1] In Table 5.1 we tabulate the scalar polarizabilities and tensor polarizabilities for a few potential spectroscopy states for each degree of freedom at a DC field, $\omega_e = 0$. We chose to calculate polarizabilities for the two vibrational states ($v = 0$ and $v = 8$) that provide a transition with the highest absolute sensitivity to μ.

Table 5.1 paints a complex picture, showing that a compromise must be made when choosing spectroscopy states. As expected, the scalar rotational polarizability is the dominant contributor for J = 0 states, because the rotational degree of freedom provides the closest states of opposite parity. When not in J $\neq$ 0, the interaction of J with J + 1 and J - 1 cancel each other out.[2] This however comes at a penalty because the rotational tensor stark shift is very large for J > 0 states. Also, J > 1/2 states will have a nonzero quadrupole shift. Fortunately, both the tensor Stark shift and the quadrupole shift can be nulled by averaging over transitions between all Zeeman states or by measuring the transition with three different magnetic field directions [152]. We therefore would want to use the $|v=0, J=1\rangle$ and $|v=8, J=2\rangle$ states for spectroscopy.

[1] ΔE was calculated by diagonalizing the Hamiltonian at an arbitrary electric field, and $\alpha^s(\omega_e)$ was subtracted to obtain $\alpha^T(\omega_e)$

[2] This is cancellation is slightly spoiled by centrifugal distortion.

	Δ^X_{300} (mHz)			
	$\Delta^{\mathrm{r}}_{300}$	$\Delta^{\mathrm{v}}_{300}$	$\Delta^{\mathrm{SO}}_{300}$	$\Delta^{\mathrm{e}}_{300}$
$\|0,0\rangle$	12	-0.2	-0.4	-10
$\|0,1\rangle^*$	11	-0.2	-0.2	-10
$\|0,2\rangle$	11	-0.2	-0.2	-10
$\|8,2\rangle^*$	11	0.4	-0.1	-6

Table 5.2. Contributions to 300 K BBR shifts for selected $X_1 0^+$ J-states $|v, J\rangle$. The proposed spectroscopy transition is marked*.

5.5.4.1. Blackbody Radiation. To calculate the shift associated with blackbody radiation, we need to calculate each contribution from every other state to which our spectroscopy states can couple. The dipole moments for each of these transitions can be calculated as shown in Eq. 5.25. At 300 K, blackbody radiation consists of a distribution of radiation, which must be integrated over for each coupling state. We do this integration numerically following the procedure in [153].[1] The corresponding shifts and the contributions from each molecular degree of freedom are presented in Table 5.2. Assuming a 5 K temperature stability at 300 K, the fractional precision on our spectroscopy transition would be below 1×10^{-18}.

5.5.4.2. Probe Laser Light Shift. The saturation intensity I_{sat} of the spectroscopy transition is proportional to $\Gamma^2_{\mathrm{tot}}/d^2$, where Γ_{tot} is the total relaxation rate of the upper state, and d is the transition moment of the transition [154, 155]. We consider the TeH^+ $|X_1 0^+, v = 0\rangle \rightarrow |X_1 0^+, v = 8\rangle$ transition. The upper state $|v = 8\rangle$ has $\Gamma_8 = 25\ \mathrm{s}^{-1}$, whereas the spectroscopy channel has $\Gamma_{08} = 2.4 \times 10^{-4}\ \mathrm{s}^{-1}$. Despite the coupling to other decay channels, I_{sat} is only 1.5 $\mu\mathrm{W/mm}^2$. At this drive intensity, the differential light shift from coupling to the $A_2 1$ manifold is 0.5 mHz, and the light shift from the remaining electronic states is much smaller.

[1]For the $A_2 1$ state we calculate the shift at each R, performing a double integral.

5.5.4.3. Quadrupole Shift. Most molecules will have a quadrupole moment due to the arrangement of nuclear and electronic charges, which can interact with the electric field gradients in the environment. The interaction Hamiltonian will be the same as Eq. 4.15. Matrix elements can be evaluated in a similar manner as in Section 4.5.4, as shown in [156]. Note that in an ion trap, there is a natural field gradient stemming from the endcaps of the trap itself. The potential of a linear Paul trap is [116]:

$$V(x,y,z) = U_{rf} + \frac{U_{dc}\kappa}{z_0^2}(2z^2 - x^2 - y^2) \tag{5.40}$$

where U_{rf} is the RF component, U_{dc} is the voltage applied to the end caps, z_0 is the half-distance between the end caps and κ is a geometrical factor. The factor $U_{dc}\kappa/z_0^2$ is the field gradient and can be expressed in convenient units: V/mm^2. The field gradient in Eq. 5.40 is expressed in Cartesian coordinates and is directly proportional to the spherical tensor that can be used for evaluating matrix elements:

$$T_0^2(\boldsymbol{\nabla E}) = \frac{1}{\sqrt{6}}(2z^2 - x^2 - y^2). \tag{5.41}$$

One can determine the value of the quadrupole moment by varying the end cap voltage and measuring the shift as demonstrated in [157].

For TeH^+ The quadrupole moment functions were obtained by personal communication with the authors of [11]. Integrating over the internuclear distance R the quadrupole moment functions $Q_{ZZ}(R)$, $Q_{XX}(R)$ and $Q_{YY}(R)$ for $v = 0$ in $X_1 0^+$ yield 1.10, -0.552 and -0.552 ea_0^2, respectively. For $v = 8$ the corresponding values are: 2.24, -1.12 and -1.12 ea_0^2.

Because the quadrupole interaction is a rank-2 interaction, any state with less than unity total angular momentum will have a quadrupole shift of zero. Hyperfine structure then allows the unique scenario of driving a dipole allowed, quadrupole shift-free transition: $|J, F = 1/2\rangle \rightarrow |J \pm 1, F = 1/2\rangle$.

5.5.5. Doppler Shifts

The thermal motion of the molecule can cause Doppler shifts that will increase $\Delta\nu$. First order Doppler shifts can be eliminated by driving carrier transitions on the molecular ion trapped in the Lamb-Dicke regime [158]. However, second order Doppler shifts due to relativistic time dilation cannot be avoided. The fractional shift is given by [159]:

$$\frac{\Delta\nu_{\mathrm{D2}}}{\nu} = -\frac{E_K}{mc^2} \tag{5.42}$$

where $\Delta\nu_{\mathrm{D2}}$ is the second order Doppler shift, E_K is the kinetic energy, c is the speed of light and m is the mass of the molecular ion. The lowest kinetic energy achievable will depend on the mass and cooling characteristics of the co-trapped atomic ion used to cool the molecule. Instead, Eq. 5.42 tells us that heavier molecular ions have a fundamental advantage. For heavy ions such as TeH^+, second order Doppler shifts can be reduced to the 10^{-20} level [160].

One interesting feature for TeH^+ and similar molecules, is the negative static differential polarizability when driving between $|v = 0, J = 0\rangle$ and $|v = 8, J = 1\rangle$, which arises because only J = 0 has a large static polarizability due to nearby rotational states, and the rotational contribution is the largest. In this scenario one can tune the RF frequency of the ion trap such that the second order Doppler shift cancels out the Stark shift. Plugging

in our differential polarizability ($\sim$ 700 a.u.) into Eq. 15 of [161] yields an RF frequency of approximately 2 MHz. This frequency is too small for a quantum logic spectroscopy experiment; however, the fast optical state preparation methods available to TeH^+ and the short excited state lifetime of $b0^+$ could make TeH^+ suitable for the production of multi-ion clocks [162], using fluorescence detection.

5.6. Projected Uncertainties in TeH^+

While the previous sections provided a semi-quantitative picture of the expected Zeeman and Stark shifts, the actual shifts are determined by diagonalizing the effective Hamiltonian (Appendix C), which fully includes hyperfine structure. Section 5.5.4 argued that the $|v = 0, J = 1\rangle$ and $|v = 8, J = 2\rangle$ states would be best for single molecule spectroscopy, due to their inherently small scalar polarizabilities. The remaining choice of hyperfine states makes the most impact on the Zeeman shifts. The $|v = 0, J = 1, F = 1/2\rangle$ and $|v = 0, J = 2, F = 3/2\rangle$ states have quadratic Zeeman shifts in the same direction, as do the $|v = 0, J = 1, F = 3/2\rangle$ and $|v = 0, J = 2, F = 5/2\rangle$ states. The former set of states has fewer Zeeman states to average over, making it the more convenient spectroscopy channel. The projected uncertainties for the $|v = 0, J = 1, F = 1/2\rangle \rightarrow |v = 0, J = 2, F = 3/2\rangle$ transition are presented in Table 5.3.

The differential Stark shifts were calculated for the spectroscopy channel via diagonlization using a 100 V/m electric field uncertainty, and the scalar and tensor Stark shifts are split via Eq. 5.30. Although smaller electric field uncertainties have been achieved for single ions [163, 160], we use 100 V/m as a conservative estimate. The projected

Effect	$\sigma/f \times 10^{18}$
BBR Stark	0.9
DC Stark, Scalar	0.09
DC Stark, Tensor	$\ll 1$
Light shift	< 1
Quadrupole	< 1
Quadratic Zeeman	0.6
Statistics (at 1 day)	10

Table 5.3. Projected uncertainty for spectroscopy on TeH^+ $|v = 0, J = 1, F = 1/2\rangle \rightarrow |v = 8, J = 2, F = 3/2\rangle$.

uncertainties for the tensor Stark and quadrupole shifts stem from an anticipated ability to average over Zeeman states to effectively null these shifts.

By diagonalizing at several magnetic bias fields from 0 to 2 μT, we fit the data to obtain 1^{st} and 2^{nd} order Zeeman coefficients for our spectroscopy states. We calculate ground and excited state g-factors of 0.07 and 0.05. The differential quadratic Zeeman coefficient is 40000 Hz/mT^2. Assuming a bias field of 100 nT, a field large enough to resolve all relevant Zeeman states involved, and a conservative field uncertainty of 10 nT [164], we predict a fractional quadratic Zeeman shift uncertainty of 0.6×10^{-18}. The linear shift can be nulled with an uncertainty below 1×10^{-19} after measuring opposite pairs of m_F states [32]. The differential quadratic Zeeman shift is comparable to that of atomic clocks [33], and can be made even smaller by using the ^{125}Te isotope, because the nuclear spin of the ^{125}Te will lead to an even larger hyperfine splitting.

5.7. Comparison With Other Molecules

Based on the results of the previous sections, an ideal molecule will have a deep, harmonic potential well, with long vibrational excited state lifetimes that can be quickly re-prepared in the ground state. To address systematics, the molecule's ground state

would also ideally have no electron spin or nuclear spin, and the molecule would have no electric dipole moment and be heavy. It is clear from these criteria that it is very unlikely for one molecule to possess all these attributes at once, and each molecular candidate should be carefully considered against all of these criteria. TeH^+ represents a fair compromise between many of these criteria. As a result, a single molecule experiment with TeH^+ is capable of surpassing the tightest constraints on μ-variation using current technology.

5.7.1. Vibrational Lifetimes

Consider a scenario where all technical challenges can be addressed, such as achieving perfect external field control and instant re-preparation into the initial state. In this case only the bond well depth and the excited state lifetime are critical parameters. Most diatomics with covalent bonds will have well depths of a few eV. As a result, all such molecules will have vibrational overtone transitions with absolute sensitivities to μ within a factor of a few. The longest vibrational state lifetimes occur in homonuclear molecules, which have no permanent dipole moment.[1] For these reasons homonuclear molecular ions have been proposed for sensitive μ-variation measurements [165, 139].

In such a scenario polar molecules such as TeH^+ are at a disadvantage. Although the lifetime can be improved by a factor of two by switching to TeD^+. The lifetime can be calculated by transforming the TeH^+ electric dipole moment function if the function was orginally computed in the center-of-mass frame [166]. The potential energy surface

[1]Even homonuclear molecules might have finite vibrational lifetimes due to magnetic dipole allowed transitions, quadrupole transitions or coupling to other electronic states.

for TeH^+ and TeD^+ will be the same, and the TeD^+ vibrational energy spacings can be computed using LEVEL with the TeH^+ potential energy surface.

5.7.2. State Repreparation

In a realistic experiment, superb environmental isolation can be achieved for a single ion in a linear Paul trap. However, the trade-off for great control over systematics is a penalty in accumulation of statistics, due to there being only one ion measured per experimental cycle. If we reexamine Eq. 5.8 in a linewidth-limited scenario ($T_c = 2T_R$), a single ion is surprisingly competitive. For example, given a typical spectroscopy transition in the optical domain ($\nu = 600$ THz) and a typical vibrational state lifetime (T_R) of 100 ms, the fractional precision can reach a fractional precision of approximately 5×10^{-18} with one day of integration time.

Linewidth-limited experiments are common for atomic systems; however, preparing a molecule back into a specific quantum state is significantly more challenging due to its massive internal phase space volume stemming from the rotational and vibrational degrees of freedom. Many rotational or even vibrational states can be populated at room temperature. Therefore it is in our best interest to choose a molecule that has the smallest phase space volume as possible, i.e. molecules with large vibrational and rotational constants, and no degeneracies due to electronic and nuclear spin. For example, buffer gas cooling has been demonstrated to reliably cool to 7.5 K within a few seconds the magnesium hydride ion (MgH^+), which has a ground state rotational constant of 6.4 cm^{-1} [167]. At this temperature the J = 0 state reaches a state population of approximately 0.5. However, if this temperature was achieved with O_2^+, which has a rotational constant of

1.7 cm^{-1}, the maximum state population achievable[1] would only be 0.08 in J = 7, which would accumulate statistics almost 40 times slower than MgH^+. In this regard, the large rotational and vibrational constants of TeH^+ are beneficial.

Other techniques exist to reach even colder temperatures. For example, selective photoionization of neutral molecules directly into the molecular ion's ground state has been achieved [168]. Implementation of this technique requires a method to replace the molecular ion with a new one in the correct state, for which some promising demonstrations exist [169]. Another approach is to pump the molecular ion back into the initial state using lasers. One version of this approach is to use a co-trapped atomic ion as the dissipative element, although its speed is limited to the coupling strength of the molecular ion and the co-trapped atomic ion. Using a frequency comb, this technique can be extended to any molecule [170, 106].

5.7.3. Fast Optical State Preparation

An even faster approach involves using a broad-linewidth electronic transition to optically pump the molecule, in exact analogy to optical pumping in atomic systems. This technique is practically impossible in most molecules because of the numerous off-diagonal decay channels that will lead to population diffusion. However, molecules having small vibrational branching ratios can significantly reduce the number of required lasers [41, 42]. A pulse-shaped broadband laser can even replace many lasers, allowing for the implementation of rotational cooling on the order of 10 μs [117, 72]. Scenarios leading to highly

[1]Assuming a Boltzmann distribution

diagonal Franck-Condon factors are detailed in [171] and have also been predicted to occur in other heavy species such as lanthanides [172].

As seen in Section 5.1, TeH^+ has extremely small vibrational branching ratios and reasonably short electronic state liftimes. One drawback is that TeH^+ has an additional electronic state to optically pump. Although we would ultimately want to perform spectroscopy in the ground $X_1 0^+$ state, the $b0^+ \rightarrow X_2 1$ transition's lifetime is approximately 20 times shorter than that of $b0^+ \rightarrow X_1 0^+$. Any cooling scheme will then require coupling between all three of these levels, which is an added complication. There is also a non-negligible magnetic dipole moment between these states, allowing transitions between states of like parity. For example, this gives the $X_2 1$ state a lifetime of 460 ms.[1] AlH^+ in contrast has only two electronic states to consider for its cooling scheme and a 20-fold shorter upper electronic state lifetime. A manuscript providing detailed analysis of potential cooling schemes, statistics and μ-variation performance for TeH^+ is currently in preparation [173].

5.7.4. Miscellaneous Properties

TeH^+ also has properties that make it experimentally convenient. The isotope of interest, $I = 0$ ^{130}Te, has a 34% natural abundance. Odd isotopes are also abundant and can lead to level structure with first-order Zeeman insensitive clock transitions and smaller quadratic Zeeman shifts due to larger hyperfine splittings. The low melting point of Te allows a bright and stable beam of TeH using a Smalley-type source using molten tellurium [88, 75], from which TeH^+ can be produced by resonance enhanced multi-photon ionization. Also,

[1] Magnetic dipole moments were obtained via personal communication from the authors of [11].

neither ^{130}Te nor H possesses a nuclear quadrupole moment, leading to a more accurate determination of molecular constants. $^{130}TeH^+$ is also a relatively heavy ion, which in addition to reducing second order Doppler shifts (Section 5.5.5), the mass of $^{130}TeH^+$ is fairly close to that of Ba^+, making Ba^+ an ideal candidate for sympathetic cooling and quantum logic state readout [104].

References

[1] H. J. Metcalf and P. van der Straten, *Laser Cooling and Trapping*, Graduate Texts in Contemporary Physics (Springer New York, 1999).

[2] C. F. Roos, Ph.D. thesis, University of Innsbruck at Innsbruck, Austria (2000).

[3] S. Webster, Ph.D. thesis, University of Oxford at Oxford, United Kingdom (2005).

[4] H. Pauly, *Atom, Molecule, and Cluster Beams I: Basic Theory, Production and Detection of Thermal Energy Beams*, Atom, Molecule, and Cluster Beams (Springer, 2000).

[5] U. Even, EPJ Techniques and Instrumentation **2**, 17 (2015).

[6] G. Herzberg and J. W. T. Spinks, *Molecular Spectra and Molecular Structure: Diatomic molecules*, Prentice-Hall physics series; U. Condon, ed (Van Nostrand, 1950).

[7] J. Brown and A. Carrington, *Rotational Spectroscopy of Diatomic Molecules* (Cambridge University Press, 2003).

[8] S. Truppe, Ph.D. thesis, Imperial College London at London, England (2014).

[9] W. Christen, K. Rademann, and U. Even, J. Chem. Phys. **125**, 174307 (2006).

[10] C. M. Seck, M. G. Kokish, M. R. Dietrich, and B. C. Odom, Phys. Rev. A **93**, 053415 (2016).

[11] L. Gonçalves dos Santos, A. G. S. de Oliveira-Filho, and F. R. Ornellas, J. Chem. Phys. **142**, 024316 (2015).

[12] C.-Y. Lien, Ph.D. thesis, Northwestern University at Evanston, IL, United States (2014).

[13] M. Dine and A. Kusenko, Rev. Mod. Phys. **76**, 1 (2003).

[14] L. Abbott, Sci. Am. **258**, 106 (1988).

[15] B. P. Schmidt, Rev. Mod. Phys. **84**, 1151 (2012).

[16] D. Clowe, M. Bradač, A. H. Gonzalez, M. Markevitch, S. W. Randall, C. Jones, and D. Zaritsky, Astrophys. J. **648**, L109 (2006).

[17] J.-P. Uzan, Living Rev. Relativ. **14**, 2 (2011).

[18] J. Rich, Am. J. Phys. **71**, 1043 (2003).

[19] T. Nilsson, On time-variation of the fundamental constants (2003).

[20] J.-P. Uzan, Rev. Mod. Phys. **75**, 403 (2003).

[21] P. A. M. Dirac, P. R. Soc. A **338**, 439 (1974).

[22] S. Dodelson, M. Kaplinghat, and E. Stewart, Phys. Rev. Lett. **85**, 5276 (2000).

[23] N. Arkani-Hamed, L. J. Hall, C. Kolda, and H. Murayama, Phys. Rev. Lett. **85**, 4434 (2000).

[24] A. Derevianko and M. Pospelov, Nat. Phys. **10**, 933 (2014).

[25] Y. V. Stadnik and V. V. Flambaum, Phys. Rev. Lett. **115**, 201301 (2015).

[26] W. J. Marciano, Physical Review Letters **52**, 489 (1984).

[27] S. G. Karshenboim, Can. J. Phys. **83**, 767 (2005).

[28] S. A. Levshakov, F. Combes, F. Boone, I. I. Agafonova, D. Reimers, and M. G. Kozlov, Astron. Astrophys. **540**, L9 (2012).

[29] A. Songaila and L. L. Cowie, Astrophys. J. **793**, 103 (2014).

[30] J. K. Webb, J. A. King, M. T. Murphy, V. V. Flambaum, R. F. Carswell, and M. B. Bainbridge, Phys. Rev. Lett. **107**, 191101 (2011).

[31] C. J. A. P. Martins, Rep. Prog. Phys. **80**, 126902 (2017).

[32] T. Nicholson, S. Campbell, R. Hutson, G. Marti, B. Bloom, R. McNally, W. Zhang, M. Barrett, M. Safronova, G. Strouse, et al., Nat. Commun. **6**, 6896 (2015).

[33] A. D. Ludlow, M. M. Boyd, J. Ye, E. Peik, and P. O. Schmidt, Rev. Mod. Phys. **87**, 637 (2015).

[34] T. Rosenband, D. B. Hume, P. O. Schmidt, C. W. Chou, A. Brusch, L. Lorini, W. H. Oskay, R. E. Drullinger, T. M. Fortier, J. E. Stalnaker, et al., Science **319**, 1808 (2008).

[35] R. M. Godun, P. B. R. Nisbet-Jones, J. M. Jones, S. A. King, L. A. M. Johnson, H. S. Margolis, K. Szymaniec, S. N. Lea, K. Bongs, and P. Gill, Phys. Rev. Lett. **113**, 210801 (2014).

[36] P. Jansen, H. L. Bethlem, and W. Ubachs, J. Chem. Phys. **140**, 010901 (2014).

[37] V. V. Flambaum and A. F. Tedesco, Phys. Rev. C **73**, 055501 (2006).

[38] V. V. Flambaum, D. B. Leinweber, A. W. Thomas, and R. D. Young, Phys. Rev. D **69**, 115006 (2004).

[39] N. Huntemann, B. Lipphardt, C. Tamm, V. Gerginov, S. Weyers, and E. Peik, Phys. Rev. Lett. **113**, 210802 (2014).

[40] J. Bagdonaite, M. Daprà, P. Jansen, H. L. Bethlem, W. Ubachs, S. Muller, C. Henkel, and K. M. Menten, Phys. Rev. Lett. **111**, 231101 (2013).

[41] E. S. Shuman, J. F. Barry, and D. DeMille, Nature **467**, 820 (2010).

[42] J. H. V. Nguyen, C. R. Viteri, E. G. Hohenstein, C. D. Sherrill, K. R. Brown, and B. Odom, New J. Phys. **13**, 063023 (2011).

[43] A. Shelkovnikov, R. J. Butcher, C. Chardonnet, and A. Amy-Klein, Phys. Rev. Lett. **100**, 150801 (2008).

[44] P. Blythe, B. Roth, U. Fröhlich, H. Wenz, and S. Schiller, Phys. Rev. Lett. **95**, 183002 (2005).

[45] S. Willitsch, M. T. Bell, A. D. Gingell, and T. P. Softley, Phys. Chem. Chem. Phys. **10**, 7200 (2008).

[46] A. Ostendorf, C. B. Zhang, M. A. Wilson, D. Offenberg, B. Roth, and S. Schiller, Phys. Rev. Lett. **97**, 243005 (2006).

[47] B. Roth, A. Ostendorf, H. Wenz, and S. Schiller, J. Phys. B - At. Mol. Opt. **38**, 3673 (2005).

[48] D. Offenberg, C. B. Zhang, C. Wellers, B. Roth, and S. Schiller, Phys. Rev. A **78**, 061401 (2008).

[49] R. Rugango, J. E. Goeders, T. H. Dixon, J. M. Gray, N. B. Khanyile, G. Shu, R. J. Clark, and K. R. Brown, New J. Phys. **17**, 035009 (2015).

[50] Y. Wan, F. Gebert, F. Wolf, and P. O. Schmidt, Phys. Rev. A **91**, 043425 (2015).

[51] F. Wolf, Y. Wan, J. C. Heip, F. Gebert, C. Shi, and P. O. Schmidt, Nature **530**, 457 (2016).

[52] C.-w. Chou, C. Kurz, D. B. Hume, P. N. Plessow, D. R. Leibrandt, and D. Leibfried, Nature **545**, 203 (2017).

[53] C. Seck, Ph.D. thesis, Northwestern University at Evanston, IL, United States (2016).

[54] Y.-W. Lin, Ph.D. thesis, Northwestern University at Evanston, IL, United States (2016).

[55] V. Rajagopal, Ph.D. thesis, Northwestern University at Evanston, IL (2014).

[56] M. G. Kokish, V. Rajagopal, J. P. Marler, and B. C. Odom, Rev. Sci. Instrum. **85**, 086111 (2014).

[57] W. G. Rellergert, S. T. Sullivan, S. Kotochigova, A. Petrov, K. Chen, S. J. Schowalter, and E. R. Hudson, Phys. Rev. Lett. **107**, 243201 (2011).

[58] H. Loh, K. C. Cossel, M. C. Grau, K.-K. Ni, E. R. Meyer, J. L. Bohn, J. Ye, and E. A. Cornell, Science **342**, 1220 (2013).

[59] M. V. DePalatis and M. S. Chapman, Phys. Rev. A **88**, 023403 (2013).

[60] B. Roth, D. Offenberg, C. Zhang, and S. Schiller, Phys. Rev. A **78**, 042709 (2008).

[61] Y.-P. Chang, K. Długołęcki, J. Küpper, D. Rösch, D. Wild, and S. Willitsch, Science **342**, 98 (2013).

[62] K. Mølhave and M. Drewsen, Phys. Rev. A **62**, 011401 (2000).

[63] J. Deckers and J. B. Fenn, Rev. Sci. Instrum. **34**, 96 (1963).

[64] B. A. Collings and M. A. Romaschin, J. Am. Soc. Mass. Spectr. **20**, 1714 (2009).

[65] M. Drewsen, C. Brodersen, L. Hornekær, J. S. Hangst, and J. P. Schifffer, Phys. Rev. Lett. **81**, 2878 (1998).

[66] A. Steele, L. Churchill, P. Griffin, and M. Chapman, Phys. Rev. A **75**, 053404 (2007).

[67] V. Rajagopal, J. P. Marler, M. G. Kokish, and B. C. Odom, Eur. J. Mass Spectrom. **22**, 1 (2016).

[68] F. Brandi and F. Giammanco, Opt. Express **19**, 347 (2011).

[69] J. M. Guevremont, S. Sheldon, and F. Zaera, Rev. Sci. Instrum. **71**, 3869 (2000).

[70] H. Pauly, *Atom, Molecule, and Cluster Beams II: Cluster Beams, Fast and Slow Beams, Accessory Equipment and Applications*, vol. 2 (Springer, 2000).

[71] J. B. Cross, Rev. Sci. Instrum. **53**, 38 (1982).

[72] C.-Y. Lien, C. M. Seck, Y.-W. Lin, J. H. Nguyen, D. A. Tabor, and B. C. Odom, Nat. Commun. **5**, 4783 (2014).

[73] C. M. Seck, E. G. Hohenstein, C.-Y. Lien, P. R. Stollenwerk, and B. C. Odom, J. Mol. Spectrosc. **300**, 108 (2014).

[74] Y. F. Zhu, R. Shehadeh, and E. R. Grant, J. Chem. Phys. **97**, 883 (1992).

[75] M. G. Kokish, M. R. Dietrich, and B. C. Odom, J. Phys. B - At. Mol. Opt. **49**, 035301 (2016).

[76] A. André, D. DeMille, J. M. Doyle, M. D. Lukin, S. E. Maxwell, P. Rabl, R. J. Schoelkopf, and P. Zoller, Nat. Phys. **2**, 636 (2006).

[77] S. Schiller and V. Korobov, Phys. Rev. A **71**, 032505 (2005).

[78] D. DeMille, S. B. Cahn, D. Murphree, D. A. Rahmlow, and M. G. Kozlov, Phys. Rev. Lett. **100**, 023003 (2008).

[79] A. Leanhardt, J. Bohn, H. Loh, P. Maletinsky, E. Meyer, L. Sinclair, R. Stutz, and E. Cornell, J. Mol. Spectrosc. **270**, 1 (2011).

[80] P. F. Staanum, K. Højbjerre, P. S. Skyt, A. K. Hansen, and M. Drewsen, Nat. Phys. **6**, 271 (2010).

[81] B. Roth, J. C. J. Koelemeij, H. Daerr, and S. Schiller, Phys. Rev. A **74**, 040501 (2006).

[82] K.-K. Ni, H. Loh, M. Grau, K. C. Cossel, J. Ye, and E. A. Cornell, J. of Mol. Spectrosc. **300**, 12 (2014).

[83] J. E. Goeders, C. R. Clark, G. Vittorini, K. Wright, C. R. Viteri, and K. R. Brown, J. Phys. Chem. A **117**, 9725 (2013).

[84] G. Meng, Master's thesis, National University of Singapore (2013).

[85] K. Chen, S. J. Schowalter, S. Kotochigova, A. Petrov, W. G. Rellergert, S. T. Sullivan, and E. R. Hudson, Phys. Rev. A **83**, 030501 (2011).

[86] M. A. Duncan, Rev. Sci. Instrum. **83**, 041101 (2012).

[87] M. F. Jarrold, J. E. Bower, and J. S. Kraus, J. Chem. Phys. **86**, 3876 (1987).

[88] C. M. Neal, G. A. Breaux, B. Cao, A. K. Starace, and M. F. Jarrold, Rev. Sci. Instrum. **78**, 075108 (2007).

[89] J. O'Hanlon, *A User's Guide to Vacuum Technology* (John Wiley & Sons, 2003).

[90] G. V. Chertihin and L. Andrews, J. Phys. Chem. **97**, 10295 (1993).

[91] Y. Zhang and M. Stuke, Chem. Phys. Lett. **149**, 310 (1988).

[92] M. Ebben, G. Meijer, and J. ter Meulen, Appl. Phys. B - Lasers O. **50**, 35 (1990).

[93] K. Luria, W. Christen, and U. Even, J. Phys. Chem. A **115**, 7362 (2011).

[94] S. A. Mitchell and P. A. Hackett, J. Chem. Phys. **79**, 4815 (1983).

[95] S. K. Tokunaga, J. O. Stack, J. J. Hudson, B. E. Sauer, E. A. Hinds, and M. R. Tarbutt, J. Chem. Phys. **126**, 124314 (2007).

[96] M. R. Tarbutt, J. J. Hudson, B. E. Sauer, E. A. Hinds, V. A. Ryzhov, V. L. Ryabov, and V. F. Ezhov, J. Phys. B - At. Mol. Opt. **35**, 5013 (2002).

[97] A. B. Bullock and P. R. Bolton, J. Appl. Phys. **85**, 460 (1999).

[98] M. Di Rosa, Eur. Phys. J. D **31**, 395 (2004).

[99] J. M. O. Matos, P. Malmqvist, and B. O. Roos, J. Chem. Phys. **86**, 5032 (1987).

[100] P. O. Schmidt, T. Rosenband, C. Langer, W. M. Itano, J. C. Bergquist, and D. J. Wineland, Science **309**, 749 (2005).

[101] I. Labazan, N. Krstulović, and S. Milošević, Chem. Phys. Lett. **428**, 13 (2006).

[102] S. D. Beattie and G. S. McGrady, Int. J. Hydrogen Energ. **34**, 9151 (2009).

[103] M. Guggemos, D. Heinrich, O. A. Herrera-Sancho, R. Blatt, and C. F. Roos, New J. Phys. **17**, 103001 (2015).

[104] J. B. Wübbena, S. Amairi, O. Mandel, and P. O. Schmidt, Phys. Rev. A **85**, 043412 (2012).

[105] T. Hasegawa, Phys. Rev. A **83**, 053407 (2011).

[106] S. Ding and D. N. Matsukevich, New J. Phys. **14**, 023028 (2012).

[107] D. Wineland, C. Monroe, W. Itano, D. Leibfried, B. King, and D. Meekhof, J. Res. Nat. Bur. Stand. **103**, 259 (1998).

[108] I. V. Inlek, C. Crocker, M. Lichtman, K. Sosnova, and C. Monroe, Phys. Rev. Lett. **118**, 250502 (2017).

[109] U. G. Poschinger, G. Huber, F. Ziesel, M. Deiß, M. Hettrich, S. A. Schulz, K. Singer, G. Poulsen, M. Drewsen, R. J. Hendricks, et al., J. Phys. B - At. Mol. Opt. **42**, 154013 (2009).

[110] C. R. Clark, J. E. Goeders, Y. K. Dodia, C. R. Viteri, and K. R. Brown, Phys. Rev. A **81**, 043428 (2010).

[111] Y.-W. Lin, S. Williams, and B. C. Odom, Phys. Rev. A **87**, 011402 (2013).

[112] X. Chen, Y.-W. Lin, and B. C. Odom, New J. Phys. **17**, 043037 (2015).

[113] Y. Wan, F. Gebert, J. B. Wübbena, N. Scharnhorst, S. Amairi, I. D. Leroux, B. Hemmerling, N. Lörch, K. Hammerer, and P. O. Schmidt, Nat. Commun. **5** (2014).

[114] Y. Wan, Ph.D. thesis, Gottfried Wilhelm Leibniz Universitt Hannover at Hannover, Germany (2014).

[115] C. Hempel, Ph.D. thesis, University of Innsbruck at Innsbruck, Austria (2014).

[116] C. B. Zhang, D. Offenberg, B. Roth, M. A. Wilson, and S. Schiller, Phys. Rev. A **76**, 012719 (2007).

[117] C.-Y. Lien, S. R. Williams, and B. Odom, Phys. Chem. Chem. Phys. **13**, 18825 (2011).

[118] V. V. Flambaum, Phys. Rev. A **73**, 034101 (2006).

[119] W. Holst, Nature **132**, 1003 (1933).

[120] R. S. Mulliken, Rev. Mod. Phys. **4**, 1 (1932).

[121] M. A Morrison and G. A Parker, Aust. J. Phys. **40**, 465 (1987).

[122] M. Goto and S. Saito, Astrophys. J. **452** (1995).

[123] W. Szajna and M. Zachwieja, J. Mol. Spectrosc. **269**, 56 (2011).

[124] L. B. Knight, S. T. Cobranchi, B. W. Gregory, and E. Earl, J. Chem. Phys. **86**, 3143 (1987).

[125] C. H. Townes and A. L. Schawlow, *Microwave Spectroscopy*, Dover books on physics (Dover Publications, 2013).

[126] H. Lefebvre-Brion and R. W. Field, *The Spectra and Dynamics of Diatomic Molecules* (Elsevier Academic Press, 2004).

[127] J. T. Hougen, Tech. Rep., National Bureau of Standards, Gaithersburg, MD (1970).

[128] A. Hansson and J. K. Watson, J. Mol. Spectrosc. **233**, 169 (2005).

[129] M. G. Kokish, P. R. Stollenwerk, M. Kajita, and B. C. Odom (2017), arxiv:1710.08589.

[130] P. F. Bernath, *Spectra of Atoms and Molecules* (Oxford University Press, 2005).

[131] R. J. Le Roy, J. Quant. Spectrosc. Ra. **186**, 167 (2017).

[132] D. DeMille, S. Sainis, J. Sage, T. Bergeman, S. Kotochigova, and E. Tiesinga, Phys. Rev. Lett. **100**, 043202 (2008).

[133] W. Nagourney, J. Sandberg, and H. Dehmelt, Phys. Rev. Lett. **56**, 2797 (1986).

[134] N. Hinkley, J. A. Sherman, N. B. Phillips, M. Schioppo, N. D. Lemke, K. Beloy, M. Pizzocaro, C. W. Oates, and A. D. Ludlow, Science **341**, 1215 (2013).

[135] N. Huntemann, C. Sanner, B. Lipphardt, C. Tamm, and E. Peik, Phys. Rev. Lett. **116**, 063001 (2016).

[136] E. Riis and A. G. Sinclair, J. Phys. B - At. Mol. Opt. **37**, 4719 (2004).

[137] L. Hollberg, C. W. Oates, E. Anne Curtis, E. N. Ivanov, S. A. Diddams, T. Udem, H. G. Robinson, J. C. Bergquist, R. J. Rafac, W. M. Itano, et al., IEEE J. Quantum Elect. **37**, 1502 (2001).

[138] V. Letchumanan, P. Gill, E. Riis, and A. G. Sinclair, Phys. Rev. A **70**, 33419 (2004).

[139] D. Hanneke, R. A. Carollo, and D. A. Lane, Phys. Rev. A **94**, 050101 (2016).

[140] T. Takekoshi, C. Strauss, F. Lang, J. H. Denschlag, M. Lysebo, and L. Veseth, Phys. Rev. A **83**, 062504 (2011).

[141] J. Xie and R. N. Zare, J. Chem. Phys. **93**, 3033 (1990).

[142] L. Veseth, J. Phys. B - At. Mol. Opt. **6**, 1473 (1973).

[143] G. Bujin and C. Linton, J. Mol. Spectrosc. **147**, 120 (1991).

[144] T. Rosenband, P. Schmidt, D. Hume, W. Itano, T. Fortier, J. Stalnaker, K. Kim, S. Diddams, J. Koelemeij, J. Bergquist, et al., Phys. Rev. Lett. **98**, 220801 (2007).

[145] M. Takamoto, F.-L. Hong, R. Higashi, Y. Fujii, M. Imae, and H. Katori, J. Phys. Soc. Jpn. **75**, 104302 (2006).

[146] J. F. Ogilvie, J. Oddershede, and S. P. A. Sauer, in *Advances in Chemical Physics: Volume 111* (2007), pp. 475–536.

[147] M. Lysebo and L. Veseth, Phys. Rev. A **83**, 033407 (2011).

[148] J. R. P. Angel and P. G. H. Sandars, P. R. Soc. A **305**, 125 (1968).

[149] A. Khadjavi, A. Lurio, and W. Happer, Physical Review **167**, 128 (1968).

[150] M. Brieger, Chem. Phys. **89**, 275 (1984).

[151] K. D. Bonin and V. V. Kresin, *Electric-dipole Polarizabilities of Atoms, Molecules, and Clusters* (World Scientific, 1997).

[152] P. Dubé, A. A. Madej, J. E. Bernard, L. Marmet, J.-S. Boulanger, and S. Cundy, Phys. Rev. Lett. **95**, 033001 (2005).

[153] J. W. Farley and W. H. Wing, Phys. Rev. A **23**, 2397 (1981).

[154] T. Zelevinsky, S. Kotochigova, and J. Ye, Phys. Rev. Lett. **100**, 043201 (2008).

[155] R. Krems, B. Friedrich, and W. C. Stwalley, *Cold Molecules: Theory, Experiment, Applications* (CRC Press, 2009).

[156] M. Germann and S. Willitsch, Mol. Phys. **114**, 769 (2016).

[157] G. P. Barwood, H. S. Margolis, G. Huang, P. Gill, and H. A. Klein, Phys. Rev. Lett. **93**, 133001 (2004).

[158] A. A. Madej and J. E. Bernard, in *Frequency Measurement and Control* (Springer Berlin Heidelberg, Berlin, Heidelberg, 2001), pp. 153–195.

[159] D. J. Berkeland, J. D. Miller, J. C. Bergquist, W. M. Itano, and D. J. Wineland, J. Appl. Phys. **83**, 5025 (1998).

[160] J. Keller, T. Burgermeister, D. Kalincev, J. Kiethe, and T. E. Mehlstäubler, J. Phys. Conf. Ser. **723**, 2 (2015).

[161] P. Dubé, A. A. Madej, Z. Zhou, and J. E. Bernard, Phys. Rev. A **87**, 023806 (2013).

[162] K. Arnold, E. Hajiyev, E. Paez, C. H. Lee, M. D. Barrett, and J. Bollinger, Phys. Rev. A **92**, 032108 (2015).

[163] S. Charles Doret, J. M. Amini, K. Wright, C. Volin, T. Killian, A. Ozakin, D. Denison, H. Hayden, C.-S. Pai, R. E. Slusher, et al., New J. Phys. **14**, 073012 (2012).

[164] A. A. Madej, P. Dubé, Z. Zhou, J. E. Bernard, and M. Gertsvolf, Phys. Rev. Lett. **109**, 203002 (2012).

[165] M. Kajita, G. Gopakumar, M. Abe, M. Hada, and M. Keller, Phys. Rev. A **89**, 032509 (2014).

[166] B. Folomeg, P. Rosmus, and H.-J. Werner, Chem. Phys. Lett. **136**, 562 (1987).

[167] A. K. Hansen, O. O. Versolato, Ł. Kłosowski, S. B. Kristensen, A. Gingell, M. Schwarz, A. Windberger, J. Ullrich, J. R. C. López-Urrutia, and M. Drewsen, Nature **508**, 76 (2014).

[168] X. Tong, A. H. Winney, and S. Willitsch, Phys. Rev. Lett. **105**, 143001 (2010).

[169] S. Kahra, G. Leschhorn, M. Kowalewski, A. Schiffrin, E. Bothschafter, W. Fuß, R. de Vivie-Riedle, R. Ernstorfer, F. Krausz, R. Kienberger, et al., Nat. Phys. **8**, 238 (2012).

[170] D. Leibfried, New J. Phys. **14**, 023029 (2012).

[171] T. A. Isaev, S. Hoekstra, and R. Berger, Phys. Rev. A **82**, 052521 (2010).

[172] A. Dunning, A. Petrov, S. J. Schowalter, P. Puri, S. Kotochigova, and E. R. Hudson, J. Chem. Phys. **143**, 124309 (2015).

[173] P. R. Stollenwerk, M. G. Kokish, A. G. S. de Oliveira-Filho, F. R. Ornellas, and B. C. Odom, in press (2018).

[174] G. Morigi and H. Walther, Eur. Phys. J. D **13**, 261 (2001).

[175] S. Ding, Ph.D. thesis, National University of Singapore at Singapore (2015).

[176] R. A. Frosch and H. M. Foley, Physical Review **88**, 1337 (1952).

[177] T. Okabayashi, E. Y. Okabayashi, M. Tanimoto, T. Furuya, and S. Saito, Chem. Phys. Lett. **422**, 58 (2006).

[178] F. Tezcan, T. D. Varberg, F. Stroh, and K. M. Evenson, J. Mol. Spectrosc. **185**, 290 (1997).

[179] H. Fujiwara, K. Kobayashi, H. Ozeki, S. Saito, and A. Ismail Jaman, J. Chem. Soc. Faraday T. **93**, 1045 (1997).

[180] S. H. Ashworth and J. M. Brown, J. Chem. Soc. Faraday T. **86**, 1995 (1990).

[181] J. M. Brown, R. F. Curl, and K. M. Evenson, J. Chem. Phys. **81**, 2884 (1984).

[182] V. Stackmann, K. Lipus, and W. Urban, Mol. Phys. **80**, 635 (1993).

APPENDIX A

AlH Source Construction

A.1. Miscellaneous Construction Information

For additional information about the reducing flange holding the glass nozzle, see [74] and the associated machine drawing (Fig. A.2). The skimmer is mounted to a stainless steel adapter plate (Fig. A.4), which is mounted to a reducing flange (Fig. A.3) using vented screws.

The glass nozzle is relatively simple to make. The tube can be cut to the appropriate length starting from a long tube. The hole exiting to the oven was drilled using a diamond-tipped Dremel bit, which are inexpensive to purchase. A Dremel was used because a high 10000 RPM drill speed is recommended for drilling glass. To control heat the drilling was done submerged in water. Additional grooves around the tube's opening to the boron-nitride oven were drilled using a sphere-tipped bit, in order to achieve a better seal between the tube and the oven. A conical tip was used to drill the nozzle opening.

As mentioned in the main text, although the boron-nitride oven is held fixed by the tungsten wire wrapped around it attached to the feedthroughs, we provide a more secure fixture using a metal clamp. The clamp is made from an Amphenol RF 31-759, BNC grounding lug with the tips clipped to the correct length. The full assembly is pictured in Fig. A.1. The seal between the boron nitride oven and the opening of the glass tube

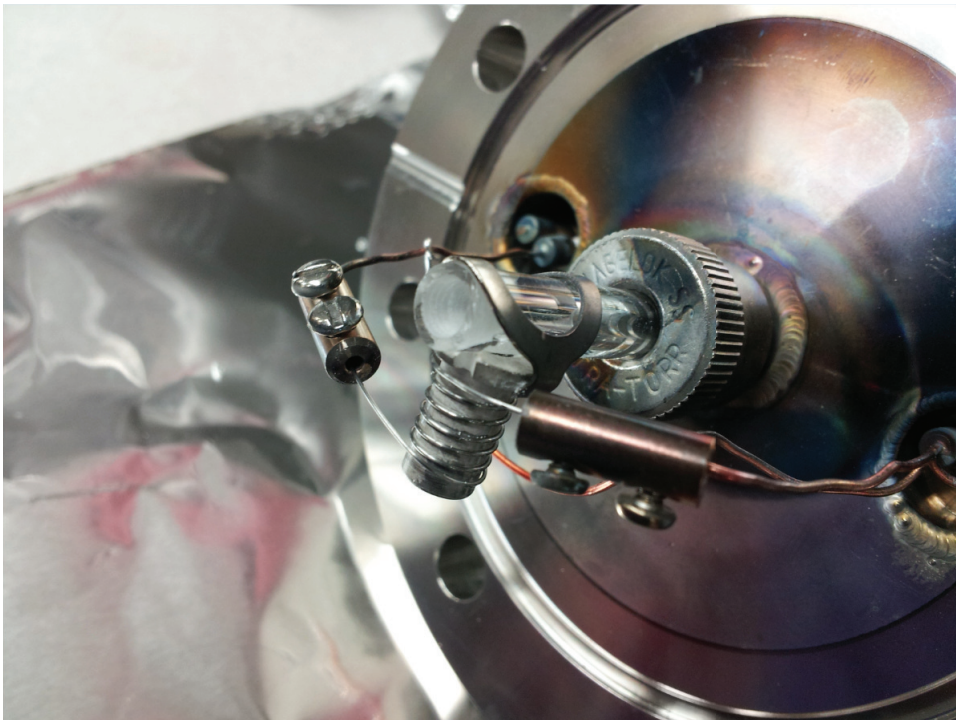

Figure A.1. Assembled source.

can be made better by filing some of the oven away to match the shape of the opening in the glass tube. The boron-nitride material is soft.

A.2. Machine Drawings

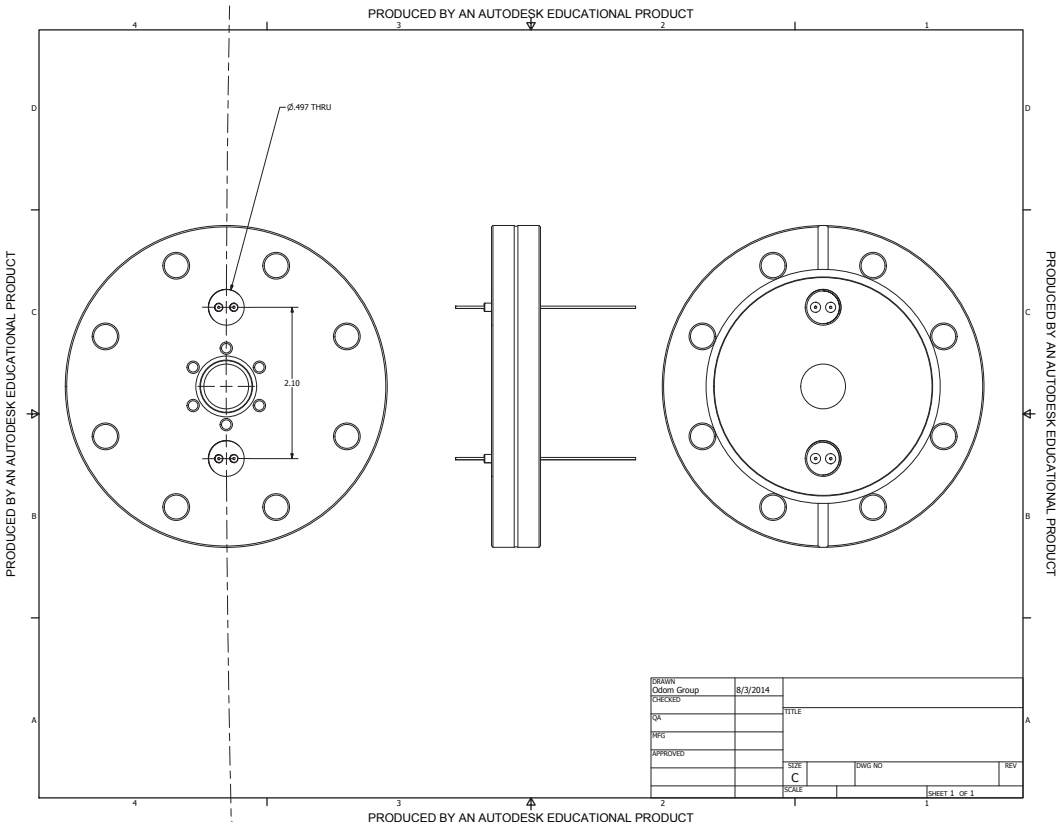

Figure A.2. 4.5" to 1.33" ConFlat reducing flange with four feedthroughs welded in place. Glass tube holder not shown.

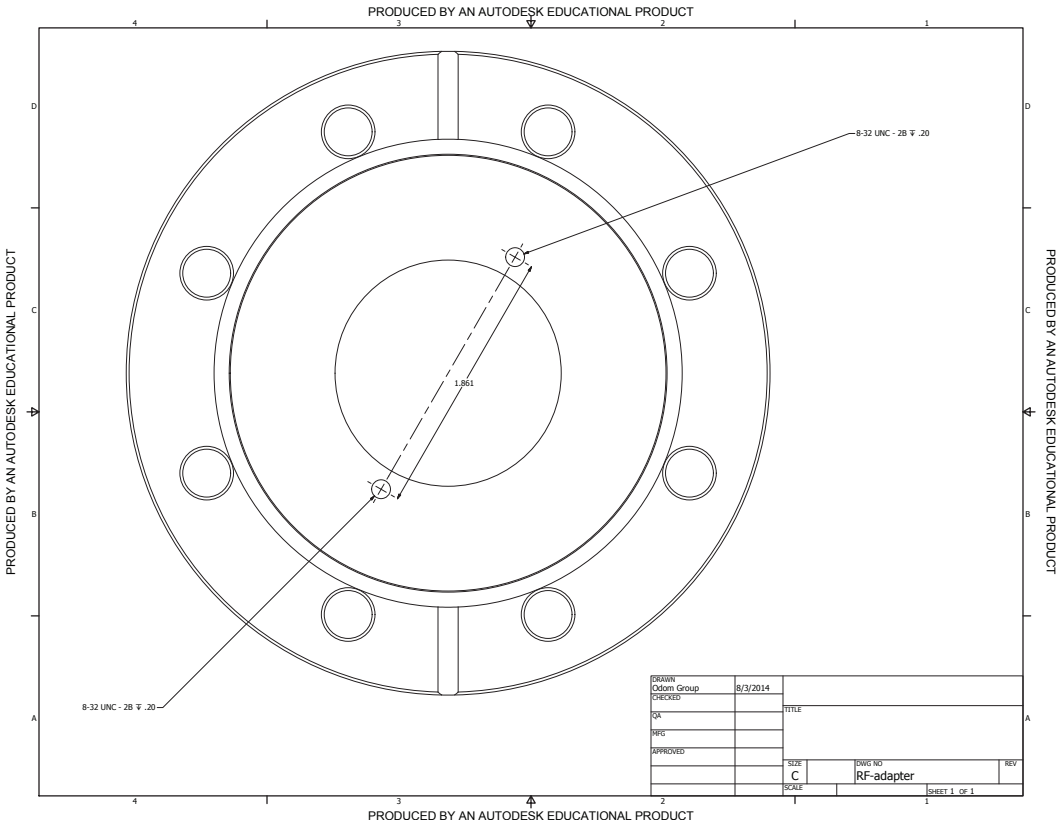

Figure A.3. 4.5” to 2.75” ConFlat reducing flange that holds the adapter plate for the skimmer.

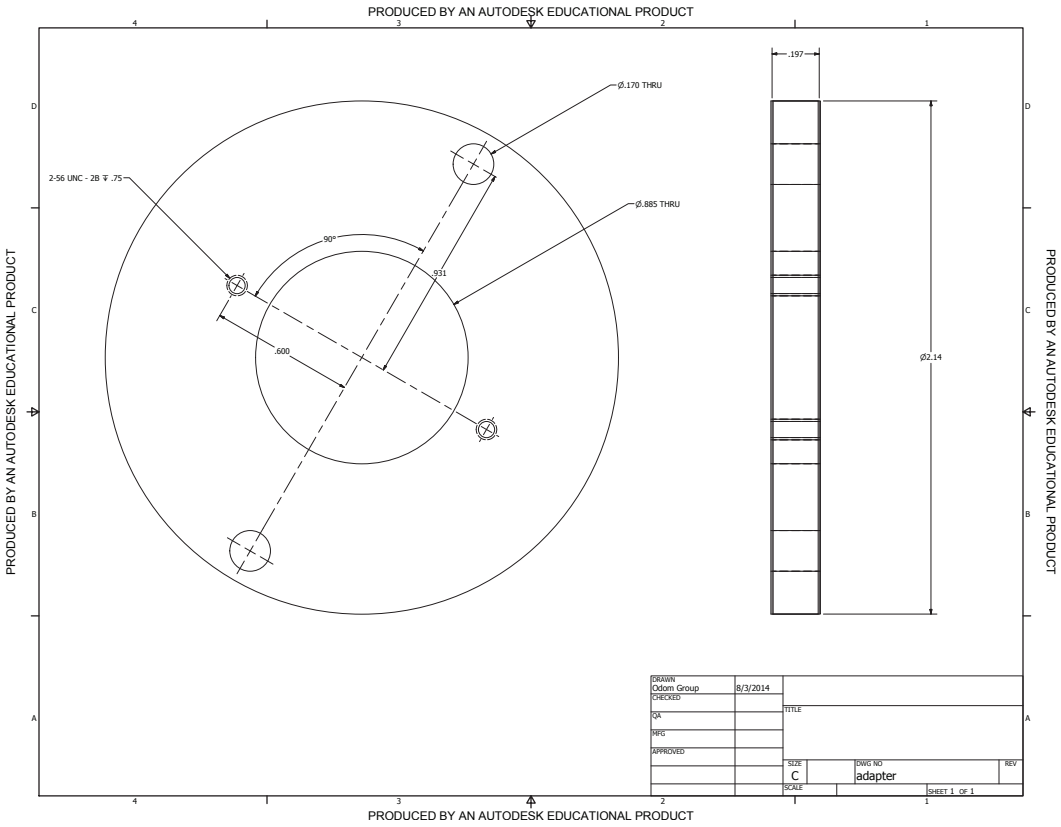

Figure A.4. Skimmer adapter plate.

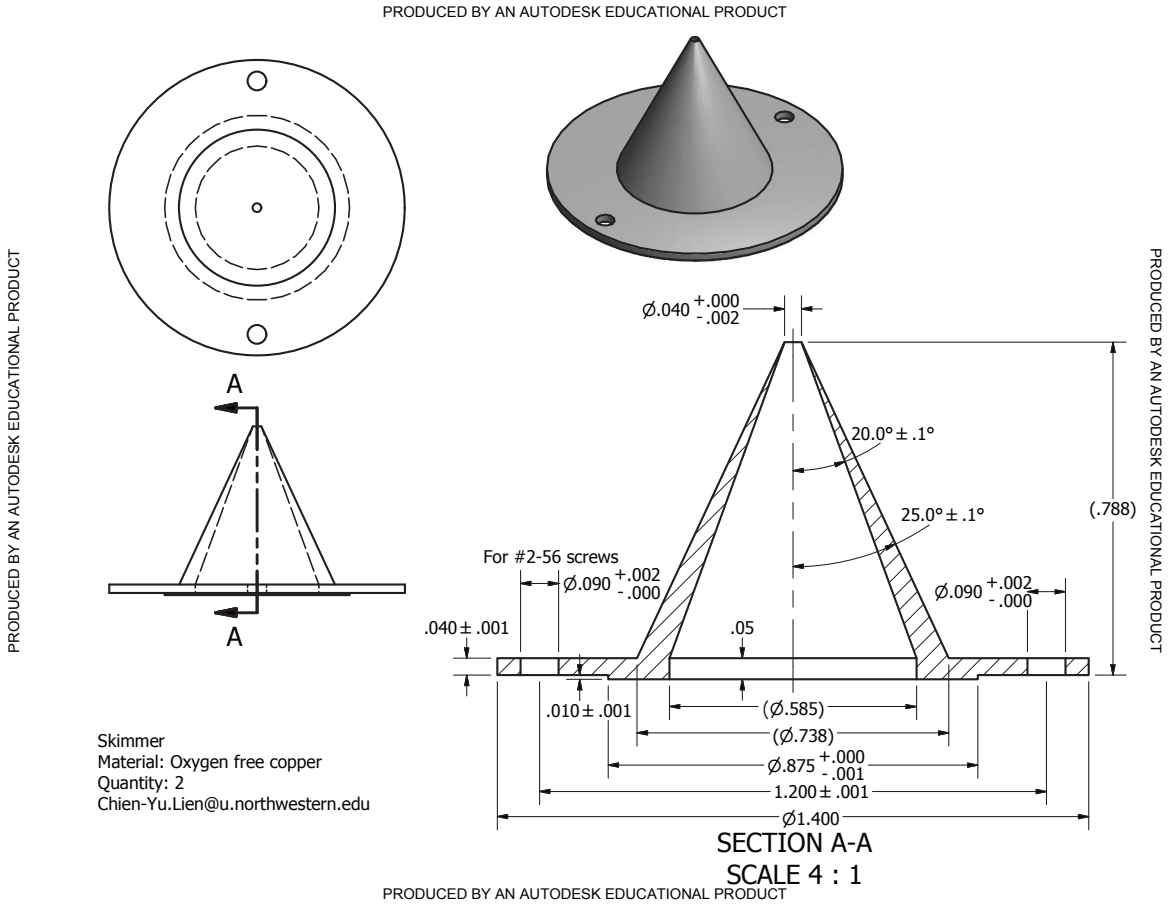

Figure A.5. Skimmer, the same as was used in [12].

APPENDIX B

Derivation of Effective Lamb-Dicke Parameters in a Two-Ion Crystal

B.1. Introduction

Although we can calculate the Lamb-Dicke parameters for each ion in the trap, we can only measure the normal modes of motion. We therefore need a framework for understanding how momentum imparted on one ion transfers its energy to the normal modes of the crystal. There are several derivations for finding the normal modes in the context of two trapped ions: [174], [104], [105], [114], [175]. Here I will re-derive the dynamics for this problem and comment on how the different published sources relate to this derivation.

B.2. Two Trapped Ions in the Normal Mode Basis

The potential energy for this system in the Z direction can be written as [105]:

$$V = \frac{1}{2}m_1\Omega_1^2 z_1^2 + \frac{1}{2}m_2\Omega_2^2 z_2^2 + \frac{e^2}{4\pi\epsilon_0(z_2 - z_1)} \tag{B.1}$$

where m_1 is the laser-cooled ion mass, m_2 is the spectroscopy ion, Ω_1 and Ω_2 are the corresponding secular frequencies for each individual ion, and z_1 and z_2 are the positions of the laser-cooled and spectroscopy ion along the z axis. Since the secular frequency Ω inversely depends on the square root of the mass, the potential energy for both ions is

actually the same, assuming they have the same charge.[1] Equation B.1 can be re-written as:

$$V = \frac{1}{2}u_0 z_1^2 + \frac{1}{2}u_0 z_2^2 + \frac{e^2}{4\pi\epsilon_0(z_2 - z_1)} \tag{B.2}$$

where u_0 is in units of kg/s^2. The kinetic energy can be written as:

$$T = \frac{1}{2}m_1 \dot{z_1}^2 + \frac{1}{2}m_2 \dot{z_2}^2 \tag{B.3}$$

At low kinetic energies, the ions will crystallize around their equilibrium positions, which can be found by solving $\delta V/\delta z_1 = 0$ and $\delta V/\delta z_2 = 0$ for z_1 and z_2. The equilibrium positions relative to the origin are:

$$Z_0 = \pm \left(\frac{e^2}{16\pi\epsilon_0 u_0} \right)^{\frac{1}{3}} \tag{B.4}$$

Because the ions mostly oscillate around their equilibrium positions, we can switch to displacement (from equilibrium) coordinates. For convenience, the coordinates are also mass-weighted.

$$q_1 = \sqrt{m_1}(z_1 - Z_0) \tag{B.5}$$

$$q_2 = \sqrt{m_2}(z_2 + Z_0) \tag{B.6}$$

The potential can be Taylor expanded about the equilibrium positions and truncated to second order:

$$V \approx V_0 + \sum_i \frac{\delta V}{\delta q_i} q_i + \frac{1}{2}\sum_{i,j} \frac{\delta^2 V}{\delta q_i \delta q_j} q_i q_j \tag{B.7}$$

[1]Here both ions are singly charged.

where i is 1 or 2. V_0 does not affect the equations of motion and $\delta V/\delta q_i = 0$ at the equilibrium positions. Substituting Equations B.4, B.5, and B.6 into B.7 yields V in displacement coordinates:[1]

$$V = u_0 \left(\frac{q_1}{\sqrt{m_1}} - \frac{q_2}{\sqrt{m_2}} \right)^2 \tag{B.8}$$

The Lagrangian, $\mathcal{L}$ = T - V, is then:

$$\mathcal{L} = \frac{1}{2}\dot{q_1}^2 + \frac{1}{2}\dot{q_2}^2 - u_0 \left(\frac{q_1}{\sqrt{m_1}} - \frac{q_2}{\sqrt{m_2}} \right)^2 \tag{B.9}$$

Using the Lagrangian, we arrive at two equations of motion using:

$$\frac{d}{dt}\left(\frac{\delta \mathcal{L}}{\delta \dot{q}_i}\right) - \frac{\delta \mathcal{L}}{\delta q_i} = 0 \qquad\qquad i = 1, 2 \tag{B.10}$$

Substituting Equation B.9 into Equation B.10 yields:

$$\ddot{q_1} + \frac{2q_1 u_0}{m_1} - \frac{q_2 u_0}{\sqrt{m_1 m_2}} = 0 \tag{B.11}$$

$$\ddot{q_2} - \frac{q_1 u_0}{\sqrt{m_1 m_2}} + \frac{2q_2 u_0}{m_2} = 0 \tag{B.12}$$

To solve the equations of motion, we insert the trial solutions:

$$q_1 = Ae^{i\omega t} \tag{B.13}$$

$$q_2 = Be^{i\omega t} \tag{B.14}$$

where A and B are the normal mode amplitudes and ω is the normal mode frequency. Substituting Equations B.13 and B.14 into Equations B.11 and B.12 yields a system of

[1]The second order term was evaluated at $q_1 = q_2 = 0$.

equations, written in matrix notation:

$$\begin{pmatrix} \frac{2u_0}{m_1} & -\frac{u_0}{\sqrt{m_1 m_2}} \\ -\frac{u_0}{\sqrt{m_1 m_2}} & \frac{2u_0}{m_2} \end{pmatrix} \begin{pmatrix} A \\ B \end{pmatrix} = \omega^2 \begin{pmatrix} A \\ B \end{pmatrix} \tag{B.15}$$

Here the 2x2 matrix in Equation B.15 turns out to be the Hessian of V evaluated at the equilibrium positions, i.e.:

$$V_H = \left. \begin{pmatrix} \frac{\delta^2 V}{\delta q_1^2} & \frac{\delta^2 V}{\delta q_1 \delta q_2} \\ \frac{\delta^2 V}{\delta q_2 \delta q_1} & \frac{\delta^2 V}{\delta q_2^2} \end{pmatrix} \right|_{\substack{q_1 = 0 \\ q_2 = 0}} \tag{B.16}$$

which is the second order term of Equation B.7. i.e. finding the normal modes for the two ion system simply reduces to finding the eigenvalues of the Hessian of V in mass-weighted displacement coordinates, where the normal modes are the square root of the eigenvalues. The eigenvalues and eigenvectors for each normal mode, labeled + and −, are:

$$\omega_\pm^2 = \frac{u_0}{m_1}\left(1 + \frac{1}{\mu} \pm \sqrt{1 - \frac{1}{\mu} + \frac{1}{\mu^2}}\right), \tag{B.17}$$

$$A_\pm = \left(\frac{1}{1 + \left(1 - \frac{1}{\mu} \mp \sqrt{1 - \frac{1}{\mu} + \frac{1}{\mu^2}}\right)^2 \mu}\right)^{1/2}, \tag{B.18}$$

$$B_\pm = \left(1 - \frac{1}{\mu} \mp \sqrt{1 - \frac{1}{\mu} + \frac{1}{\mu^2}}\right)\sqrt{\mu} A_\pm, \tag{B.19}$$

where $\mu = m_2/m_1$.[1] Equations B.17, B.18 and B.19 can be substituted into Equations B.13 and B.14. In general, Equations B.13 and B.14 will satisfy B.15 when multiplied

[1]The mass ratio μ here should not be confused with the proton-to-electron mass ratio m_p/m_e.

by an arbitrary constant, yielding:

$$q_1 = q_+ A_+ e^{i\omega_+ t} \tag{B.20}$$

$$q_2 = q_+ B_+ e^{i\omega_+ t} \tag{B.21}$$

$$q_1 = q_- A_- e^{i\omega_- t} \tag{B.22}$$

$$q_2 = q_- B_- e^{i\omega_- t} \tag{B.23}$$

Note that an even more general solution will involve an additional term for the $-\omega$ frequency, which can be associated with its own arbitrary constant. For example:

$$q_1 = q_+^+ A_+ e^{i\omega_+ t} + q_+^- A_+ e^{-i\omega_+ t} \tag{B.24}$$

However, here we choose to ignore the $-\omega$ terms, as they will not affect the physical conclusions derived from these solutions. Adding Equation B.20 to B.22 and Equation B.21 to B.23 and rearranging, we arrive at:

$$q_1 = \frac{1}{2}\left(q_+ A_+ e^{i\omega_+ t} + q_- A_- e^{i\omega_- t}\right) \tag{B.25}$$

$$q_2 = \frac{1}{2}\left(q_+ B_+ e^{i\omega_+ t} + q_- B_- e^{i\omega_- t}\right) \tag{B.26}$$

By using the orthogonality condition, $A_+ A_- + B_+ B_- = 0$ and recognizing that $B_+ = A_-$ and $B_- = -A_+$, one can reproduce equations 10 and 11 in [104]. Note that Equations 9 in [174], are the eigenvectors of Equation B.16, but transformed out of the mass-weighted

basis, i.e.

$$\sqrt{m_1}\begin{pmatrix} \frac{1}{\sqrt{m_1}} & 0 \\ 0 & \frac{1}{\sqrt{m_2}} \end{pmatrix}\begin{bmatrix} N_+\left(\frac{1-\mu-\sqrt{1-\frac{1}{\mu}+\frac{1}{\mu^2}}}{\sqrt{\mu}}\right) & N_-\left(\frac{1-\mu+\sqrt{1-\frac{1}{\mu}+\frac{1}{\mu^2}}}{\sqrt{\mu}}\right) \\ N_+ & N_- \end{bmatrix} \tag{B.27}$$

where $N_\pm$ are the normalization factors as described in [174]. Note that the eigenvectors (Equations 9 in [174]) are named $q_\pm$, which are analogous to $(A_\pm, B_\pm)$ in this text. These should not to be confused with $q_\pm$ in this text, which are the normal mode amplitudes, analogous to z_o and z_i in [174].

B.3. Physical Interpretation

In the case of equal masses, $\mu = 1$, the eigenvectors reduce to:

$$\begin{pmatrix} A_\pm \\ B_\pm \end{pmatrix} = \frac{1}{\sqrt{2}}\begin{pmatrix} 1 \\ \mp 1 \end{pmatrix} \tag{B.28}$$

where we can conclude that the + mode corresponds to the out-of-phase mode, since the displacements for each ion have opposite signs, whereas the − mode is the in-phase mode, due to the displacements having the same signs. Similarly, the − eigenvalue is lower in energy than the + eigenvalue.

We can more extract physical insight by plotting the eigenvectors, Equations B.18 and B.19, as a function of mass ratio, Figure B.1. Both A_- and B_+ asymptote to 0 for large mass ratios, while A_+ and B_- asymptote to 1. We can use this to predict the effect on ion displacement using Equations B.25 and B.26. For the heavier ion, at large mass ratios, both normal mode components asymptote to zero due to the $1/\sqrt{\mu}$ factor. This means that the heavier ion's displacement eventually reduces to zero. The lighter ion,

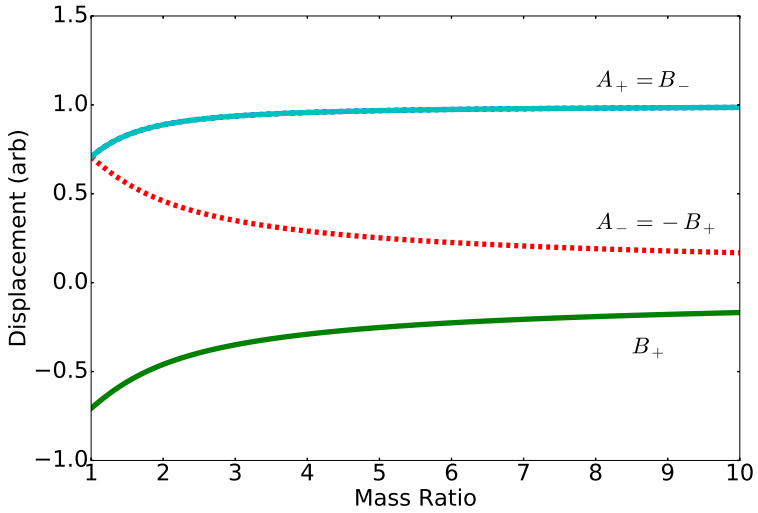

Figure B.1. Eigenvectors from Equations B.18 and B.19. Both A_- and B_+ asymptote to 0 for large mass ratios.

however, only has the out-of-phase component left over at large mass ratios, meaning the light ion continues to oscillate as if there was no coupling from the heavier ion. These conclusions are the same as those described in the second paragraph of section 2.1 in [174].

Using the same analysis for intermediate mass ratios, we can conclude that the heavier ion contributes more to the in-phase mode, while the lighter ion contributes more to the out-of-phase mode. This will be important when analyzing how energy added to one ion adds energy to each normal mode, such as in photon recoil spectroscopy.

B.4. Lamb-Dicke Parameters

In the normal mode picture, our Hamiltonian becomes a set of two independent harmonic oscillators:

$$H = \frac{p_+^2}{2} + \frac{p_-^2}{2} + \frac{1}{2}\Omega_+^2 q_+^2 + \frac{1}{2}\Omega_-^2 q_-^2 \tag{B.29}$$

To quantize the system, we define for each mode a set of creation/annihilation operators:

$$a_{\pm} = \sqrt{\frac{\Omega_{\pm}}{2\hbar}} \left(\hat{q}_{\pm} + \frac{i}{\Omega_{\pm}} \hat{p}_{\pm} \right) \tag{B.30}$$

$$a_{\pm}^{\dagger} = \sqrt{\frac{\Omega_{\pm}}{2\hbar}} \left(\hat{q}_{\pm} - \frac{i}{\Omega_{\pm}} \hat{p}_{\pm} \right) \tag{B.31}$$

The quantized normal mode coordinate is then:

$$\hat{q}_{\pm} = \sqrt{\frac{\hbar}{2\Omega_{\pm}}} (a_{\pm}^{\dagger} + a_{\pm}) \tag{B.32}$$

The eigenvectors provide a transformation between the mass-weighted displacement coordinates and the normal mode coordinates, i.e.

$$\begin{pmatrix} q_1 \\ q_2 \end{pmatrix} = \beta \begin{pmatrix} q_+ \\ q_- \end{pmatrix} \tag{B.33}$$

where β is defined as:

$$\beta = \begin{pmatrix} A_+ & A_- \\ B_+ & B_- \end{pmatrix} \tag{B.34}$$

To transform into displacement coordinates, we can apply the matrix:

$$T^{-1} = \begin{pmatrix} \frac{1}{\sqrt{m_1}} & 0 \\ 0 & \frac{1}{\sqrt{\mu m_1}} \end{pmatrix} \tag{B.35}$$

to the left side of Equation B.33. Substituting in Equation B.32 yields the each ion in displacement coordinates:

$$q_1' = \left(A_+\sqrt{\frac{\hbar}{2\Omega_+ m_1}}\right)(a_+^\dagger + a_+) + \left(A_-\sqrt{\frac{\hbar}{2\Omega_- m_1}}\right)(a_-^\dagger + a_-) \tag{B.36}$$

$$q_2' = \left(B_+\sqrt{\frac{\hbar}{2\Omega_+ \mu m_1}}\right)(a_+^\dagger + a_+) + \left(B_-\sqrt{\frac{\hbar}{2\Omega_- \mu m_1}}\right)(a_-^\dagger + a_-) \tag{B.37}$$

Following Section 2.3 in [174], applying a radiative "kick" on one ion leads to a motional excitation in each normal mode governed by the effective Lamb-Dicke parameters, i.e. the coeffients in Equations B.36 and B.37 multiplied by the projection of the radiation's wavevector onto the normal mode axis: k_z.

To transform into mass-weighted displacement coordinates, we invoke $q_{1,2} = \beta q_{+,-}$ and apply the inverse of β to both sides. Note: the determinant of β is 1.

$$\beta^{-1} = \begin{pmatrix} B_- & -A_- \\ -B_+ & A_+ \end{pmatrix} = \beta^T = \begin{pmatrix} A_+ & B_+ \\ A_- & B_- \end{pmatrix} \tag{B.38}$$

Following Yong Wan's derivation in [114], we can use this transformation to determine how a force on one ion transfers energy into the normal modes. Equation B.10 can be modified to now include a force on one ion:

$$\frac{d}{dt}\left(\frac{\delta\mathcal{L}}{\delta\dot{q}_i}\right) - \frac{\delta\mathcal{L}}{\delta q_i} = F_i \qquad\qquad i = 1, 2 \tag{B.39}$$

or in vector notation:

$$\ddot{\mathbf{q}}_{\mathbf{1,2}} + V_H \mathbf{q}_{\mathbf{1,2}} = \mathbf{F}_{\mathbf{1,2}} \tag{B.40}$$

yielding:

$$\ddot{\mathbf{q}}_{+,-} + V_H \mathbf{q}_{+,-} = \beta^T \mathbf{F_{1,2}} \tag{B.41}$$

therefore, the components of β^T determine the energy transfer from one ion into each of the respective normal modes.

For reference, we also provide the relations between the normal mode coordinates and the original coordinate system:

$$q_+ = A_+\sqrt{m_1}(z_1 + Z_0) + B_+\sqrt{\mu m_1}(z_2 - Z_0) \tag{B.42}$$

$$q_- = A_-\sqrt{m_1}(z_1 + Z_0) + B_-\sqrt{\mu m_1}(z_2 - Z_0) \tag{B.43}$$

$$z_1 = \frac{1}{\sqrt{m_1}}(B_- q_+ - B_+ q_-) - Z_0) \tag{B.44}$$

$$z_2 = \frac{1}{\sqrt{\mu m_1}}(-A_- q_+ + A_+ q_-) + Z_0) \tag{B.45}$$

APPENDIX C

Matrix Elements for Hund's Case (c_β): TeH^+

$$\mathcal{H} = \mathcal{H}_{\rm rot} + \mathcal{H}_{\rm nsr} + \mathcal{H}_{\rm HFS} + \mathcal{H}_{Z_I} + \mathcal{H}_{Z_{\rm rot}} + \mathcal{H}_{Z_{\rm S}} + \mathcal{H}_E + \mathcal{H}_Q \tag{C.1}$$

where $\mathcal{H}_{\rm rot}$ is the rotational kinetic energy and

$$\mathcal{H}_{\rm nsr} = -c_I T^1(\boldsymbol{J}) \cdot T^1(\boldsymbol{I}), \tag{C.2}$$

$$\mathcal{H}_{\rm HFS} = bT^1(\boldsymbol{S}) \cdot T^1(\boldsymbol{I}) + cT^1_{q=0}(\boldsymbol{S}) \cdot T^1_{q=0}(\boldsymbol{I}), \tag{C.3}$$

$$\mathcal{H}_{Z_I} = -g_I \mu_N T^1_0(\boldsymbol{B}) \cdot T^1_0(\boldsymbol{I}), \tag{C.4}$$

$$\mathcal{H}_{Z_{\rm rot}} = -g_J \mu_B T^1_0(\boldsymbol{B}) \cdot T^1_0(\boldsymbol{J}), \tag{C.5}$$

$$\mathcal{H}_{Z_{\rm S}} = g_s \mu_B T^1_0(\boldsymbol{B}) \cdot T^1_0(\boldsymbol{S}), \tag{C.6}$$

$$\mathcal{H}_E = -T^1_0(\boldsymbol{\mu_e}) \cdot T^1_0(\boldsymbol{E}), \tag{C.7}$$

$$\mathcal{H}_Q = -T_0^2(\boldsymbol{\nabla E}) \cdot T_0^2(\boldsymbol{Q}). \tag{C.8}$$

Note that all fields are assumed to be along the $p = 0$ direction. The constants c_I, g_I, g_J, g_s and μ_e are the nuclear spin-rotation coupling constant, proton g factor, rotational g factor, electron spin g factor and ground state electric dipole moment, respectively. The constants b and c are the Frosch and Foley parameters [176], which are related to Fermi Contact and dipolar interaction constants: b_F and t_0 via:

$$b = b_F - \frac{c}{3} \tag{C.9}$$

and

$$t_0 = \frac{c}{3}. \tag{C.10}$$

The matrix elements are presented below. For convenience, the diagonal and off-diagonal components of the rotational Hamiltonian, $\mathcal{H}_{\rm rot}^D$ and $\mathcal{H}_{\rm rot}^{OD}$, are separated, where $\mathcal{H}_{\rm rot} = \mathcal{H}_{\rm rot}^D + \mathcal{H}_{\rm rot}^{OD}$.

$$\langle v, J_a; \Omega, J|\mathcal{H}_{\rm rot}^D|v, J_a; \Omega, J\rangle = B_v \left[J(J+1) + J_a(J_a+1) - 2\Omega^2\right] \tag{C.11}$$

$$\langle v, J_a; \Omega, J|\mathcal{H}_{\rm rot}^{OD}|v, J_a; \Omega', J\rangle = -2B_v \sum_{q=\pm 1} (-1)^{J_a-\Omega} \begin{pmatrix} J_a & 1 & J_a \\ -\Omega & q & \Omega' \end{pmatrix} (-1)^{J-\Omega} \begin{pmatrix} J & 1 & J \\ -\Omega & q & \Omega' \end{pmatrix} \times \left[J_a(J_a+1)(2J_a+1)J(J+1)(2J+1)\right]^{1/2} \tag{C.12}$$

$$
\begin{aligned}
&\langle v,J_a;\Omega,J,I,F|\mathcal{H}_{\rm HFS}|v,J_a;\Omega',J',I,F'\rangle \\
&= x(-1)^{J'+F+I}\begin{Bmatrix} I & J' & F \\ J & I & 1 \end{Bmatrix}[I(I+1)(2I+1)]^{1/2}(-1)^{J-\Omega}\begin{pmatrix} J & 1 & J' \\ -\Omega & q & \Omega' \end{pmatrix} \\
&\quad\times(-1)^{J_a-\Omega}\begin{pmatrix} J_a & 1 & J_a \\ -\Omega & q & \Omega' \end{pmatrix}(-1)^{J_a+L+S+1}\begin{Bmatrix} J_a & S & L \\ S & J_a & 1 \end{Bmatrix} \\
&\quad\times[(2J_a'+1)(2J_a+1)S(S+1)(2S+1)]^{1/2}
\end{aligned}
\tag{C.13}
$$

where $x = b, c$.

$$
\begin{aligned}
&\langle v,\,\Omega,J,I,F|\mathcal{H}_{\rm nsr}|v,\Omega,J,I,F\rangle \\
&\quad= c_I(-1)^{J+F+I}\begin{Bmatrix} I & J & F \\ J & I & 1 \end{Bmatrix}[J(J+1)(2J+1)I(I+1)(2I+1)]^{1/2}
\end{aligned}
\tag{C.14}
$$

$$
\begin{aligned}
&\langle v,\,\Omega,J,I,F,M_F|\mathcal{H}_{Z_{\rm rot}}|v,\Omega,J,I,F',M_F\rangle \\
&= -\,g_J\mu_B B_z(-1)^{F-M_F}\begin{pmatrix} F & 1 & F' \\ -M_F & 0 & M_F \end{pmatrix}(-1)^{F'+J+1+I}[(2F'+1)(2F+1)]^{1/2} \\
&\quad\times\begin{Bmatrix} J & F' & I \\ F & J & 1 \end{Bmatrix}[J(J+1)(2J+1)]^{1/2}
\end{aligned}
\tag{C.15}
$$

$$
\begin{aligned}
&\langle v,\, \Omega, J, I, F, M_F|\mathcal{H}_{Z_I}|v, \Omega, J, I, F', M_F\rangle \\
&\quad = -\, g_I \mu_N B_z (-1)^{F-M_F} \begin{pmatrix} F & 1 & F' \\ -M_F & 0 & M_F \end{pmatrix} (-1)^{F+J+1+I} [(2F'+1)(2F+1)]^{1/2} \\
&\qquad \times \begin{Bmatrix} F & I & J \\ I & F' & 1 \end{Bmatrix} [I(I+1)(2I+1)]^{1/2}
\end{aligned}
\tag{C.16}
$$

$$
\begin{aligned}
&\langle v, J_a; \Omega, J, I, F, M_F|\mathcal{H}_{Z_S}|v, J_a; \Omega', J', I, F', M_F\rangle \\
&= g_s \mu_B B_z (-1)^{F-M_F+F'+2J+I+1-\Omega} \begin{pmatrix} F & 1 & F' \\ -M_F & 0 & M_F \end{pmatrix} \begin{pmatrix} J & 1 & J' \\ -\Omega & q & \Omega' \end{pmatrix} [(2F'+1)(2F+1)]^{1/2} \\
&\quad \times [(2J'+1)(2J+1)]^{1/2} \begin{Bmatrix} J & F & I \\ F' & J' & 1 \end{Bmatrix} (-1)^{J_a-\Omega} \begin{pmatrix} J_a & 1 & J_a \\ -\Omega & q & \Omega' \end{pmatrix} (-1)^{J_a+L+S+1} \\
&\quad \times \begin{Bmatrix} J_a & S & L \\ S & J_a & 1 \end{Bmatrix} [(2J_a'+1)(2J_a+1)S(S+1)(2S+1)]^{1/2}
\end{aligned}
\tag{C.17}
$$

where $q = \Omega - \Omega'$.

The parity eigenstate in $X_2 1$ coupling to the negative parity $|v = 0, J_a = 0; \Omega = 0, J = 1\rangle$ state will be:

$$|v=8, J_a=1; J=1, -\rangle = \frac{1}{\sqrt{2}}(|v=0, J_a=1; \Omega=1, J=1\rangle - |v=0, J_a=1; \Omega=-1, J=1\rangle) \tag{C.18}$$

$$\begin{aligned}
&\langle v,\, \Omega, J, I, F, M_F|\mathcal{H}_E|v, \Omega', J', I, F', M_F\rangle \\
&= -\mu_e E_Z (-1)^{F-M_F} \begin{pmatrix} F & 1 & F' \\ -M_F & 0 & M_F \end{pmatrix} (-1)^{F+J+1+I}[(2F'+1)(2F+1)]^{1/2} \\
&\quad \times \begin{Bmatrix} J' & F' & I \\ F & J & 1 \end{Bmatrix} (-1)^{J-\Omega} \begin{pmatrix} J & 1 & J' \\ -\Omega & q & \Omega' \end{pmatrix} [(2J'+1)(2J+1)]^{1/2}
\end{aligned} \tag{C.19}$$

where μ_e is the transition dipole moment between $|\Omega\rangle$ and $|\Omega'\rangle$.

$$\begin{aligned}
&\langle v,\, \Omega, J, I, F, M_F|\mathcal{H}_Q|v, \Omega, J', I, F', M_F\rangle \\
&= T_0^2(\boldsymbol{\nabla E})(-1)^{F-M_F} \begin{pmatrix} F & 2 & F' \\ -M_F & 0 & M_F \end{pmatrix} (-1)^{F'+J+2+I}[(2F'+1)(2F+1)]^{1/2} \\
&\quad \times \begin{Bmatrix} J & F & I \\ F' & J' & 2 \end{Bmatrix} (-1)^{J-\Omega} \begin{pmatrix} J & 2 & J' \\ -\Omega & 0 & \Omega \end{pmatrix} [(2J'+1)(2J+1)]^{1/2} \\
&\quad \times \langle v, \Omega|T_0^2(\boldsymbol{Q})|v, \Omega\rangle
\end{aligned} \tag{C.20}$$

C.1. Constants

Without experimental data for TeH^+, we are forced to estimate some of the interaction constants (Table C.1). In the case of hydrides, c_I can be somewhat reliably predicted for

Table C.1. Constants used in matrix element calculations.

Constant	Value
c_I	$\sim$ 10 kHz
b	-50 MHz
c	10 MHz
g_I	5.58
g_J	-0.001
g_s	2
μ_N	7.62×10^{-4} MHz/G
μ_B	1.40×10^{-4} MHz/G

the heavy atom's nuclear spin-rotation interaction (Eq. 8-41 in [125] or [177]); however, the proton nuclear spin-rotation interaction is both difficult to observe and difficult to predict. We instead estimate the value based on measurements made for molecules possessing a heavy atom both one row below and above tellurium in the periodic table. For ZnH, $c_I(H)$ was measured to be 60 kHz [178], and for AuH it was not observed within the experimental uncertainty of 30 kHz [177]. A measurement with similar uncertainty was made for AsH, where the value of $c_I(H)$ was determined to be smaller than the uncertainty as well [179]. Although the uncertainty is large on our estimate, its effect on the hyperfine splitting is small compared to the other hyperfine parameters. The hyperfine constants b and c were estimated from the AsH molecule [179], which has very similar electronic structure to TeH^+, with As one row above Te in the periodic table. Using arguments that the Fermi Contact parameter b_F scales linearly with bond length [180] and that the dipolar constant c scales as the inverse cube of the bond length [181], b and c for TeH^+ were determined from the AsH values of -53 MHz and 13 MHz, respectively. The ratio of ground state bond lengths from TeH^+ to AsH is 1.07. The rotational g-factor g_J was estimated from a measurement of SbH [182], which has both a very similar reduced mass

and electronic structure to that of TeH^+. Its small value indicates that the rotational Zeeman interaction will be the smallest Zeeman interaction.

APPENDIX D

Machine Drawings

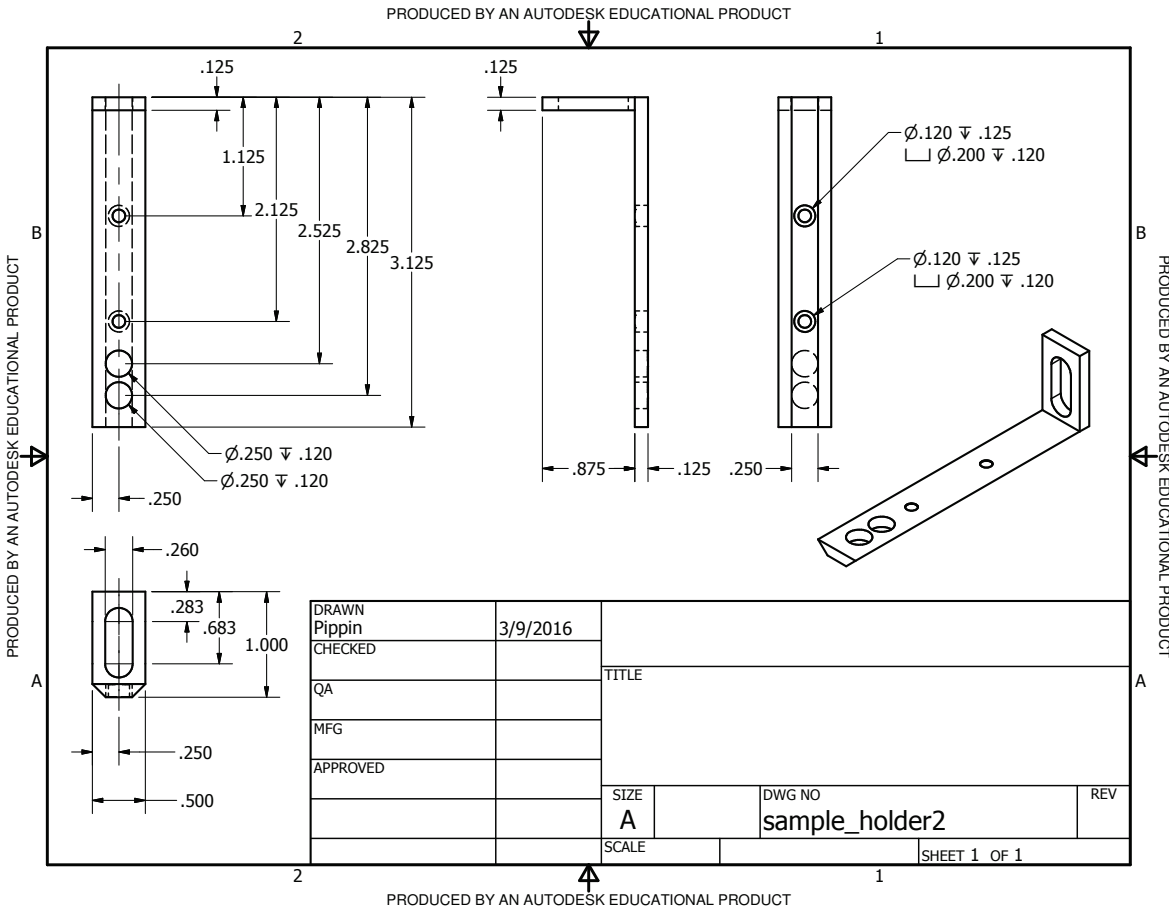

Figure D.1. Ante Chamber Sample Holder.

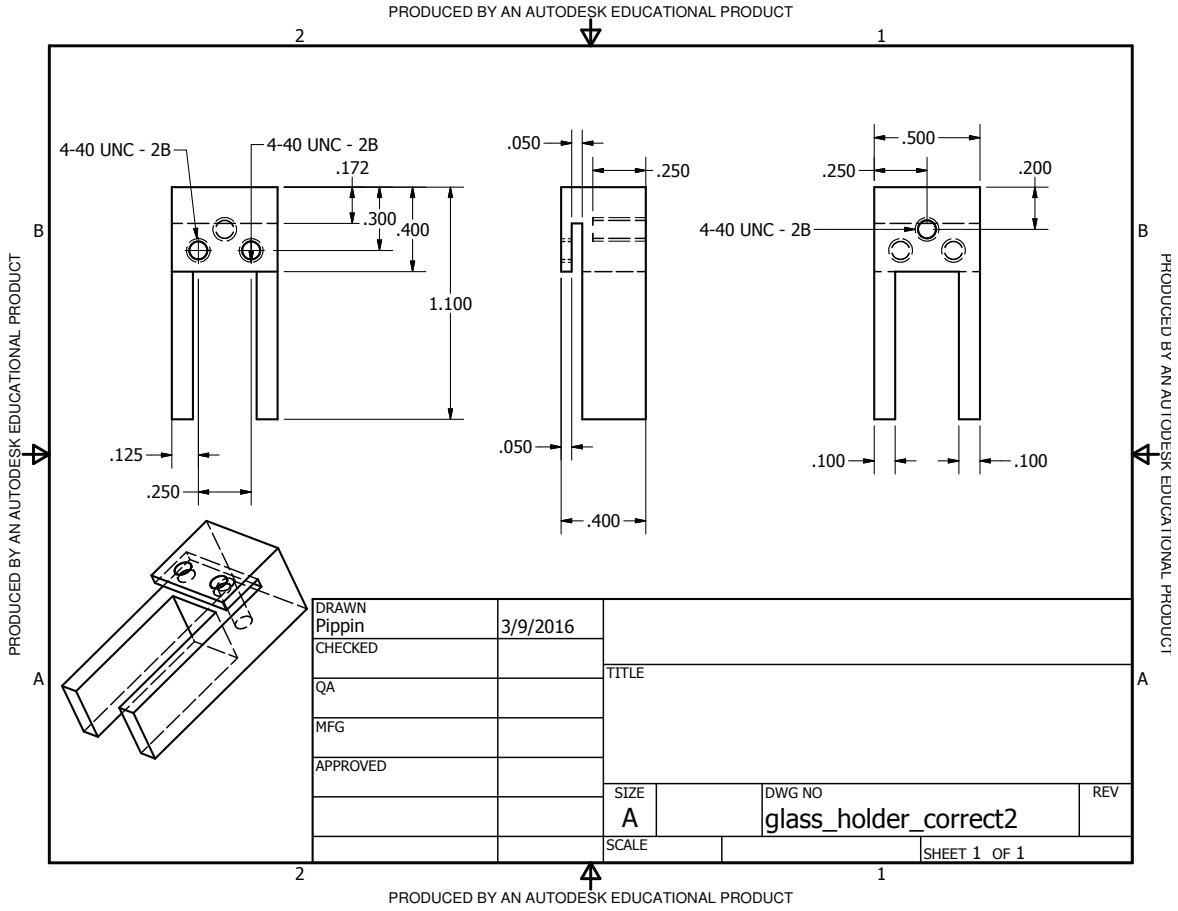

Figure D.2. Ante Chamber Sample Holder Shield Attachment.